Delft University of Technology

Design strategies for large range flexure mechanisms

Rommers, J.

DOI
10.4233/uuid:4eaf8bdb-53e2-49e5-9730-2550945b267f

Publication date
2022

Document Version
Final published version

Citation (APA)
Rommers, J. (2022). *Design strategies for large range flexure mechanisms*. [Dissertation (TU Delft), Delft University of Technology]. https://doi.org/10.4233/uuid:4eaf8bdb-53e2-49e5-9730-2550945b267f

Important note
To cite this publication, please use the final published version (if applicable).
Please check the document version above.

Copyright
Other than for strictly personal use, it is not permitted to download, forward or distribute the text or part of it, without the consent of the author(s) and/or copyright holder(s), unless the work is under an open content license such as Creative Commons.

Takedown policy
Please contact us and provide details if you believe this document breaches copyrights.
We will remove access to the work immediately and investigate your claim.

This work is downloaded from Delft University of Technology.
For technical reasons the number of authors shown on this cover page is limited to a maximum of 10.

DESIGN STRATEGIES FOR LARGE RANGE FLEXURE MECHANISMS

DESIGN STRATEGIES FOR LARGE RANGE FLEXURE MECHANISMS

Dissertation

For the purpose of obtaining the degree of doctor
at Delft University of Technology,
by the authority of the Rector Magnificus Prof. dr. ir. T. H. J. J. van der Hagen,
chair of the Board for Doctorates,
to be defended publicly on Monday 20 June 2022 at 12:30 o'clock

by

Jelle ROMMERS

Master of Science in Mechanical Engineering,
Delft University of Technology, The Netherlands,
born in Rijswijk, The Netherlands.

This dissertation has been approved by the

promotor: Prof. dr. ir. J.L. Herder
copromotor: Dr. ir. V. van der Wijk

Composition of the doctoral committee:

Rector Magnificus,	chairperson
Prof. dr. ir. J.L. Herder,	Delft University of Technology
Dr. ir. V. van der Wijk,	Delft University of Technology
Independent members:	
Prof. dr. ir. A. van Keulen,	Delft University of Technology
Prof. dr. A.A. Zadpoor,	Delft University of Technology
Prof. Dr. -Ing. habil. L. Zentner,	Technische Universität Ilmenau, Germany
Prof. dr. ir. J. P. M. B. Vermeulen,	Eindhoven University of Technology
Other member:	
Prof. dr. ir. D.M. Brouwer,	University of Twente

This work is part of the research program ‘Möbius’ with project number 14665, which is (partly) financed by the Netherlands Organization for Scientific Research (NWO).

Keywords: Precision Engineering, Flexure Mechanisms, Compliant Mechanisms

Printed by: Gildeprint

Front & Back: Close-up of the spherical joint from chapter 6.

Copyright © 2022 by J. Rommers

ISBN 978-94-6384-353-9

An electronic version of this dissertation is available at
http://repository.tudelft.nl/.

Voor Evelien

CONTENTS

Summary xi

Samenvatting xiii

Preface xvii

1 Introduction 1
- 1.1 Flexure mechanisms 2
- 1.2 Potential for improvement 2
- 1.3 Objective 3
- 1.4 Outline 4
- References 4

2 The STAGE method for simultaneous design of the stress and geometry of flexure mechanisms 7
- 2.1 Introduction 8
- 2.2 The STAGE method 9
    - 2.2.1 Step 1: Design the functional geometry 9
    - 2.2.2 Step 2: Design the internal stresses. 9
    - 2.2.3 Step 3: Calculate the stress-free fabrication geometry 14
    - 2.2.4 Step 4: Assemble the fabricated part 15
    - 2.2.5 Discussion on the STAGE method 16
- 2.3 Application example: CFP with reduced peak stress. 16
- 2.4 Application example: folded leaf spring with reduced peak stress 18
    - 2.4.1 The folded leaf spring 18
    - 2.4.2 Redesign with the STAGE method and a parameter sweep 19
    - 2.4.3 Optimal redesigned FLS 19
    - 2.4.4 Experimental validation of the peak stress reduction. 20
    - 2.4.5 Experimental validation of the functional geometry 22
- 2.5 Discussion 23
- 2.6 Conclusions. 24
- References 25

3 Reducing actuation force and peak stress of a flexure-based linear guide using the STAGE method 27
- 3.1 Introduction 28
- 3.2 Static balancing of the linear guide design using the STAGE method 28
    - 3.2.1 The folded leaf spring linear guide design 28
    - 3.2.2 Redesigning procedure 30
    - 3.2.3 Resulting redesigns 32

3.3 Experimental validation. 33
    3.3.1 Test of the actuation force reduction 33
    3.3.2 Test of the geometry after assembly 34
3.4 Discussion 34
3.5 Conclusion 36
3.6 Acknowledgment 37
References 37

4 Design of a Folded Leaf Spring with high support stiffness at large displacements using the Inverse Finite Element Method 41
4.1 Introduction 42
4.2 Method 42
    4.2.1 Support stiffness reduction of a blade flexure in the actuated state. . 42
    4.2.2 The Inverse Finite Element Method 43
    4.2.3 The folded leaf spring 44
    4.2.4 Redesign of the folded leaf spring using the IFE method 46
    4.2.5 Design and validation of the combination element 46
4.3 Results and Discussion 47
4.4 Conclusion 49
4.5 Acknowledgment 49
References 49

5 A flexure-based linear guide with torsion reinforcement structures 53
5.1 Introduction 54
5.2 Linear guide designs 55
    5.2.1 The 6 Folded Leaf Spring (6FLS) linear guide. 55
    5.2.2 The Torsion Reinforced Folded Leaf Spring (TR-FLS) 57
    5.2.3 The 2-TR-FLS linear guide 58
    5.2.4 3-TR-FLS linear guide 58
5.3 Optimization and comparison 59
    5.3.1 Performance metric 59
    5.3.2 Optimization variables and constraints 59
    5.3.3 Optimization algorithm 61
    5.3.4 Optimization results 62
5.4 Experimental validation. 63
    5.4.1 Prototype 63
    5.4.2 Measurement setup 64
    5.4.3 Experimental results 67
5.5 Discussion 68
5.6 Conclusion 70
References 70

6 A new type of spherical flexure joint based on tetrahedron elements 73
6.1 Introduction 74
6.2 Designs of the two new spherical flexure joints and their planar derivatives 75
6.3 The tetrahedron and prism elements in detail 79
    6.3.1 Equivalent representations of the tetrahedron and prism elements . 79

6.3.2 Degrees of freedom of the tetrahedron and prism elements 80
6.3.3 Equivalent stiffness of the wire flexure 81
6.3.4 Constraint stiffness terms of the prism element 82
6.3.5 Constraint stiffness terms of the tetrahedron element 84
6.3.6 Comparison of the equations to finite-element simulations 87
6.4 Discussion 90
6.5 Conclusion 91
6.6 Acknowledgment 92
References 92

7 Discussion **95**
7.1 Discussion on part 1 (chapters 2-4) 96
7.2 Discussion on part 2 (chapters 5 and 6) 97
References 97

8 Conclusion **99**
8.1 Conclusions of part 1 (chapters 2-4). 100
8.2 Conclusions of part 2 (chapters 5 and 6) 100
8.3 General conclusions 101

Acknowledgements **103**

A Inverse FEM example **105**

Curriculum Vitæ **109**

List of Publications **111**

SUMMARY

The moving parts in a mechanical device often rely on rolling or sliding contacts such as in ball bearings to gain motion. These suffice in many applications, but the friction inherent to their working principle limits their motion repeatability and thereby their precision. Flexure mechanisms are a popular alternative in the field of precision engineering because they gain motion by elastic deformation of slender segments such as thin spring steel plates, resulting in a highly repeatable motion due to the absence of friction and play. Furthermore, they are lubricant-free and do not generate particles, which makes them suitable for applications in space, astronomy, the semiconductor industry, and healthcare.

A drawback of flexure mechanisms is their limited range of motion compared to their build volume, which results in voluminous designs and which limits their application field. Their range is limited by material stress but also because at large displacements the stiffness in their support directions decreases significantly, and their actuation effort increases at large deflections, resulting in high energy consumption and heat generation. Increasing the motion range would highly benefit the field of precision engineering and could also lead to innovations in healthcare or space.

The motivation for this thesis is the observation that the vast majority of flexure mechanisms consist of initially straight and stress-free flexures. Recent developments in fabrication methods such as the additive manufacturing of steel are providing the possibility to create more complex shapes, which could improve the range of motion of flexure mechanisms.

The objective of this thesis is to provide design strategies to increase the motion range of flexure mechanisms. The thesis consists of two parts, of which the first (chapters 2-4) focuses on a new method to design stressed and curved flexures. The second part (chapters 5 and 6) further develops a recent strategy to increase the range of motion using torsion reinforcement structures.

In the first part of this thesis the stress and geometry (STAGE) method is proposed, which can be used to design the stress and geometry of flexure mechanisms simultaneously for a specified state. This allows designers to control at which point in the displacement range the flexures are curved and stressed, which in turn enables the design of initially curved and stressed flexures. The main contribution of the method is that it explicitly distinguishes between the functional geometry and the fabrication geometry, which are commonly regarded as equal. The method is valid for large displacements without simplifying the mechanics, by using the relatively unknown inverse finite-element method. The STAGE method gives insight in the achievable stress fields by providing a graphical approach. It shows that the stress field of a flexure mechanism can be designed independently from its geometry and vice versa if it is statically determinate, if bending stresses dominate, and if it consists of slender flexures with constant cross sections. If this is not the case, a parameter sweep can be used as demonstrated in chapter 3.

The potential of the STAGE method is demonstrated by creating initial stress fields in commonly used flexure mechanisms with the goal of reducing peak stress or actuation force at large displacements. In the well-known crossed-flexure pivot design, a peak stress reduction of 23% is achieved. The actuation force of a folded leaf spring linear guide mechanism is decreased by 96%, at the cost of an increase of 45% in peak stress. A different initial stress field in the latter mechanism results in a simultaneous reduction of actuation force (35%) and peak stress (28%), which is a surprising result because commonly a trade-off has to be made between these two properties. After assembly, the redesigns attain the functional geometry, which was originally intended by the designer. This means that existing flexure mechanisms could be replaced by their redesigned versions without changes in their geometry and without changing their attachment points in the machine.

Experiments validate the theoretically predicted peak stress and actuation force reduction. Additional experiments showed that the functional geometry is well attained after assembly, with geometric deviations in the order of half the thickness of the flexures. The flexures were fabricated using wire-electrical discharge machining, which is a proven fabrication method in industry.

Chapter 4 shows that curved flexures can be used to create a folded leaf spring with a high support stiffness at large displacements, and that, theoretically, a combination of different elements can be used to create a high support stiffness in the whole motion range. It is likely that the same approach will benefit other flexure designs.

In the second part of this thesis, the recent ‘torsion reinforcement’ strategy is further developed and generalized. In chapter 5, torsion reinforcement structures are added to a folded leaf spring, which increases its constraints from one to three. This enables the design of a linear guide with only two flexure elements instead of the five (or six) folded leaf springs as in pre-existing designs. Both the pre-existing and the new design are optimized on support stiffness and then compared. The support stiffness of the new design is twice as high as the pre-existing design, while occupying a 33% smaller and -perhaps more importantly- a less obstructive build volume. The models used to assess the support stiffness were validated by experiments.

In chapter 6, a generalization of the blade flexure with a single torsion reinforcement structure is presented in the form of a tetrahedron-shaped element. Using this element, two new spherical joint designs are conceived. These joints allow a large motion range without intermediate bodies, which is new with respect to the state of the art. Analytic equations are presented for the support stiffness of the element in its undeflected state, and compared to finite-element simulations.

SAMENVATTING

De bewegende onderdelen in een mechanisch apparaat werken meestal op basis van rollende of glijdende contacten, zoals in kogellagers. Deze voldoen in veel gevallen maar de herhalingsnauwkeurigheid (precisie) die ermee behaald kan worden is beperkt door de wrijving die onvermijdelijk ontstaat tussen de contactvlakken. Als alternatief worden in de precisietechniek elastische mechanismen gebruikt. Deze werken op basis van elastische vervorming, bijvoorbeeld door dunne platen van verenstaal (bladveren) die buigen om zo een beweging toe te laten. Door de afwezigheid van contactvlakken is er geen wrijving of speling, wat resulteert in een zeer hoge herhalingsnauwkeurigheid. Bovendien zijn er geen smeermiddelen nodig en worden er geen deeltjes gegenereerd, hetgeen ze erg geschikt maakt voor toepassingen in de ruimte, astronomie, de halfgeleiderindustrie en de gezondheidszorg.

Een nadeel van elastische mechanismen is hun beperkte bewegingsbereik. Dit resulteert in grote benodigde bouwvolumes, wat het toepassingsgebied beperkt. Het bereik wordt beperkt door materiaalspanningen, maar ook omdat bij grote verplaatsingen de stijfheid in de ondersteunende richtingen aanzienlijk afneemt, en omdat de benodigde actuatiekracht toeneemt, wat resulteert in een hoog energieverbruik en warmteontwikkeling. Het vergroten van het bewegingsbereik zou de precisietechniek ten goede komen en zou ook kunnen leiden tot innovaties in de zorg of de ruimtevaart.

De motivatie voor dit proefschrift is de observatie dat de overgrote meerderheid van elastische mechanismen uit dezelfde, aanvankelijk rechte en spanningsvrije bladveren bestaat. Recente ontwikkelingen in fabricagemethoden, zoals de additieve fabricage van staal, bieden de mogelijkheid om complexere vormen te creëren, wat het bewegingsbereik van elastische mechanismen zou kunnen verbeteren.

Het doel van dit proefschrift is om ontwerpstrategieën te presenteren waarmee het bewegingsbereik van elastische mechanismen vergroot kan worden. Het proefschrift bestaat uit twee delen, waarvan het eerste (hoofdstukken 2-4) zich richt op een nieuwe methode om initieel gespannen en gebogen bladveren te ontwerpen. In het tweede deel (hoofdstukken 5 en 6) wordt een recente strategie verder ontwikkeld die gebaseerd is op het verstijven van de torsierichting van bladveren, waardoor het bewegingsbereik ook vergroot kan worden.

In het eerste deel van dit proefschrift wordt de ’Stress and Geometry’ (STAGE) methode gepresenteerd die bedoeld is om de spanning en geometrie van elastische mechanismen gelijktijdig te ontwerpen, in een bepaalde stand van het mechanisme. Hierdoor kunnen ontwerpers bepalen in welke stand van het mechanisme de bladveren gebogen en gespannen zijn, wat het op zijn beurt mogelijk maakt om aanvankelijk gebogen en gespannen bladveren te ontwerpen. De belangrijkste bijdrage van de methode is dat deze expliciet onderscheid maakt tussen de functionele geometrie en de fabricagegeometrie, die over het algemeen als gelijk worden aangenomen. De methode is bruikbaar voor grote verplaatsingen zonder de mechanica te vereenvoudigen, doordat gebruik gemaakt wordt van de relatief onbekende inverse eindige-elementenmethode. De STAGE-methode geeft inzicht in welke spanningsvelden haalbaar zijn, door middel van een grafische benadering. De methode laat zien dat het spanningsveld van een elastisch mechanisme onafhankelijk van zijn functionele geometrie kan worden ontworpen en vice versa onder de voorwaarden dat het mechanisme statisch bepaald is, buigspanningen domineren en het bestaat uit slanke elementen met constante doorsneden. Als dit niet het geval is, kan een *parameter sweep* worden gebruikt zoals aangetoond in hoofdstuk 3.

Het potentieel van de STAGE-methode wordt aangetoond door initiële spanningsvelden te creëren in bekende elastische mechanismen met als doel de piekspanning of actuatiekracht bij grote verplaatsingen te verminderen. In het bekende kruisveerscharnier wordt een piekspanningsreductie van 23% bereikt. De actuatiekracht van een rechtgeleidingsmechanisme met gevouwen bladveren wordt verminderd met 96%, ten koste van een toename van 45% in piekspanning. Een ander initieel spanningsveld in hetzelfde mechanisme resulteert in een gelijktijdige vermindering van de actuatiekracht (35%) en piekspanning (28%), wat een verrassend resultaat is omdat er gewoonlijk een afweging moet worden gemaakt tussen deze twee eigenschappen. Na montage van de herontworpen mechanismen nemen zij de functionele geometrie aan die oorspronkelijk was ontworpen. Dit betekent dat bestaande elastische mechanismen kunnen worden vervangen door hun herontworpen versies zonder veranderingen in hun geometrie en zonder hun bevestigingspunten in de machine te veranderen.

De theoretisch voorspelde piekspanning en reductie van de actuatiekracht zijn beide gevalideerd met experimenten. Aanvullende experimenten toonden aan dat de functionele geometrie goed wordt bereikt na montage: de geometrische afwijkingen zijn in de orde van de helft van de dikte van de bladveren. De bladveren zijn vervaardigd door middel van draadvonken, wat een beproefde fabricagemethode is in de industrie.

Hoofdstuk 4 laat zien dat initiële krommingen kunnen worden gebruikt om een gevouwen bladveer te creëren met een hoge ondersteuningsstijfheid bij grote verplaatsingen, en dat theoretisch een combinatie van verschillende elementen kan worden gebruikt om een hoge ondersteuningsstijfheid in het gehele bewegingsbereik te creëren. Het is waarschijnlijk dat dezelfde aanpak andere ontwerpen van elastische elementen ten goede zal komen.

In het tweede deel van dit proefschrift wordt de recente strategie die gebruik maakt van torsieverstijvingen verder ontwikkeld en veralgemeniseerd. In hoofdstuk 5 worden torsieverstijvingsstructuren toegevoegd aan een gevouwen bladveer, waardoor deze niet één maar drie vrijheidsgraden onderdrukt. Dit maakt het mogelijk om een rechtgeleiding te ontwerpen met slechts twee elementen in plaats van de vijf (of zes) gevouwen bladveren zoals in reeds bestaande ontwerpen. Zowel het reeds bestaande als het nieuwe ontwerp worden in het hoofdstuk geoptimaliseerd op ondersteuningsstijfheid en vervolgens vergeleken. De ondersteuningsstijfheid van het nieuwe ontwerp is twee keer zo hoog als het reeds bestaande ontwerp, terwijl het 33% kleiner en - misschien nog belangrijker - een minder hinderlijk bouwvolume inneemt. De modellen die zijn gebruikt om de ondersteuningsstijfheid te beoordelen, worden door experimenten gevalideerd.

In hoofdstuk 6 wordt een veralgemenisering van de bladveer met een enkele torsieverstijvingsstructuur gepresenteerd in de vorm van een tetraëdervormig element. Er worden twee elastische sferische gewrichten (vergelijkbaar met kogelgewrichten) gepresenteerd die opgebouwd zijn uit dit element. Deze gewrichten hebben een groot bewegingsbereik zonder gebruik te maken van grote tussenlichamen, wat nieuw is ten opzichte van de huidige literatuur. In het hoofdstuk worden analytische vergelijkingen gepresenteerd die de ondersteuningsstijfheid van het element in zijn ongebogen stand uitdrukken. De vergelijkingen zijn gevalideerd met behulp van eindige-elementensimulaties.

PREFACE

This thesis is about a fascinating type of structures which seem to have a will of their own. Unlike regular structures, they allow some very specific motions and stubbornly resist anything else. They become even more magical when the displacements they allow are large, and this is exactly what this thesis is about.

Although my main motivation for this work was fascination, another important motivation was that these magical structures are actually called *flexure mechanisms* and are used in all kind of applications, as described in the Introduction. It was not difficult to keep these applications in mind and still do quite fundamental research, by focusing on linear and rotary motions and keeping material stresses within the limits of currently available materials. After all, many machines and devices require linear guides and rotation hinges.

The thesis is structured in the form of peer-reviewed articles, instead of a monograph. Each article contains its own specific Introduction, Discussion and Conclusion, and additionally, shorter and more general versions of these sections are provided to put the complete work into perspective.

Jelle Rommers
The Hague, May 2022

1

INTRODUCTION

This chapter introduces the objective and motivation for this thesis from the perspective of precision engineering. Flexure mechanisms are popular elements in the precision industry because they do not suffer from friction or play, but are limited to small range of motion applications. This thesis aims to provide design strategies to increase this range and consists of two parts. The first part focuses on a design method which helps to design initially curved and stressed flexures which help to decrease peak stresses, decrease actuation force, and increases support stiffness, all at large displacements. The second part further develops and generalizes a recent strategy to increase the range of motion using torsion reinforcement structures.

1.1. FLEXURE MECHANISMS

Whether the goal is to transform energy, force or motion [1, 2], mechanical devices need moving parts to do their work. These parts commonly rely on rolling or sliding contacts such as ball bearings to gain motion. If high precision is required, these do not suffice: even a perfect cylinder on a perfectly flat surface will experience micro-slip because it is compressed when loaded [3], resulting in poor motion repeatability. Active bearing principles such as magnetic levitation provide high precision by avoiding contact, but cannot be used in many applications due to their energy consumption and heat build-up.

A unique solution is provided by flexure mechanisms, which combine a passive nature and high precision by using elastic deformation to gain motion. Figure 1.1a shows a flexure mechanism consisting of steel bodies connected by thin strips known as blade flexures or leaf springs, which bend to allow motion of the end effector in the x- and y directions. Movements in the other, undesired directions have a stiffness which is orders of magnitude higher. Elastic deformation is highly repeatable because it is free from friction and play. Also, lubricants are not needed and no particles are generated, which makes flexure mechanisms highly suitable for vacuum environments and medical applications.

A drawback of flexure mechanisms is their limited range of motion, which is typically in the order of magnitude of the thickness of their flexures. In current designs there is a trade-off between motion range and other desired properties such as small build volume, low peak stresses, low stiffness in the motion direction, high stiffness in the supporting directions and high load bearing capacity. Improving the motion range of flexure mechanisms would highly benefit the precision industry (think of lithography systems) by increasing their application area, and perhaps even replacing active systems. It could also lead to innovations in healthcare, for example in bending-based orthoses which could be worn underneath clothing [4], contamination-free surgical tools [5], or additively manufactured tools for minimally-invasive surgery [6].

After a long period of research on flexure mechanisms with articles dating back ninety years [7], only recently a significant improvement has been made on the range of motion problem. The new flexure hinge designs from [8] and [9] have a total range of 40° and 80°, respectively, without the common dramatic decrease in support stiffness. This is a major improvement compared to state-of-the-art designs which rarely reach 10° [8, 10]. The strategy in the new designs is to increase the support stiffness of a blade flexure at large deflections by adding triangular 'torsion reinforcement structures' which will be explained in chapter 5.

1.2. POTENTIAL FOR IMPROVEMENT

In addition to the torsion reinforcement strategy, two other potential ways to improve the range of motion of flexure mechanisms are identified, forming the basis for this thesis.

Firstly, it is observed that the vast majority of flexure mechanisms consists of flat blade flexures (leaf springs) or straight slender rods known as wire flexures. This holds for planar mechanisms such as the example in Fig. 1.1a, but also for spatial mechanisms:

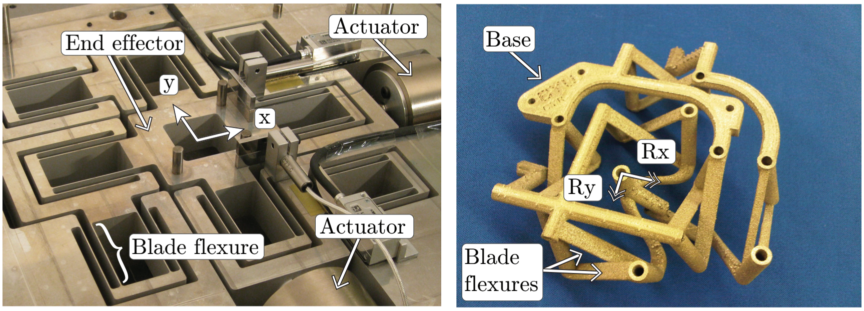

(a) (b)

Figure 1.1: (a) Flexure-based xy-stage fabricated by conventional wire-electrical discharge machining [11, 12]; (b) Flexure-based tip-tilt mechanism fabricated by additive manufacturing [13], showing the same blade flexure designs despite the improved design freedom.

Figure 1.1b shows a tip-tilt flexure mechanism design, fabricated by additive manufacturing of a titanium alloy. Although it is a complex spatial design, its flat blade flexures do not differ from the blade flexures in the more conventional planar design in Fig. 1.1a, fabricated by conventional wire electrical discharge machining. Flat blade flexures become curved during motion of the mechanism, which dramatically reduces their support stiffness and thereby limits their motion range [8]. The recent developments in additive manufacturing of steel make it possible to create more complex geometries, but this design freedom is not used to its full potential.

A second observation is that flexures are generally designed as stress-free in the initial position of the mechanism. Current design methods for flexure mechanisms consider stress as a secondary, limiting factor. This is remarkable because stresses are known as a useful design parameter in other areas of engineering, for example to reduce the stresses in concrete by using preloaded rods or to reduce the load cycle amplitude of stresses by preloading bolts such as in combustion engine heads. Stress is one of the major factors limiting the range of motion of flexure mechanisms, causing fatigue failure and increased actuation effort.

1.3. OBJECTIVE

The objective of this thesis is to provide design strategies to increase the motion range of flexure mechanisms. This objective is subdivided into two subgoals.

The first subgoal is to develop a design method which helps to exploit the potential of initially stressed and curved flexures. The method should enable designers to use curvature and stress as design variables, instead of side-effects that only occur once the mechanism is moving. Pre-stress in other areas of engineering is mainly used in the axial direction of rods and bolts, and usually for small displacements where geometry changes can be neglected. In this thesis this will be generalized to include bending stresses and large displacements.

The second subgoal is to generalize the recent ‘torsion reinforcement’ strategy. The torsion reinforcement structures have until now only been applied to single, flat blade flexures. This thesis will exploit applications to spatial flexures with large range of motion.

1.4. OUTLINE

The thesis consists of two parts, of which the first (chapters 2-4) focuses on a new design method which helps to exploit the potential of stressed and curved flexures. The second part (chapters 5 and 6) builds on the recently developed torsion reinforcement strategy from [8] and [9].

The first part starts with chapter 2 in which the design method is introduced, called the stress and geometry (STAGE) method. As a first application, it is used to reduce peak stresses at large displacements. In chapter 3, the STAGE method is used to reduce the actuation force of a linear guide flexure mechanism for large displacements. Chapter 4 shows how initially curved flexures can be used to create a high support stiffness at large displacements.

The second part of this thesis starts with chapter 5 in which the pre-existing torsion reinforcement strategy is used to create a linear guide with a large range of motion and high support stiffness. In chapter 6, a generalized version of the torsion reinforcement structures is presented and used to create two new spherical flexure joint designs with a large range of motion.

Chapter 7 provides a discussion on the results of this thesis and chapter 8 summarizes its contributions.

REFERENCES

[1] A. G. Erdman and G. N. Sandor, *Mechanism design analysis and synthesis (Vol. 1)* (Prentice-Hall, Inc., 1997).

[2] J. Shigley and J. Uicker, *Theory of Machines and Mechanisms 2nd Ed.* (McGraw Hill, 1994).

[3] H. Soemers, *Design Principles for precision mechanisms* (T-Pointprint, 2011).

[4] J. Ring and C. Kim, *A passive brace to improve activities of daily living utilizing compliant parallel mechanisms,* in *International Design Engineering Technical Conferences and Computers and Information in Engineering Conference*, Vol. 50152 (American Society of Mechanical Engineers, 2016) p. V05AT07A015.

[5] A. Lamers, J. A. G. Sánchez, and J. L. Herder, *Design of a statically balanced fully compliant grasper,* Mechanism and machine theory **92**, 230 (2015).

[6] S. Kota, K.-J. Lu, Z. Kreiner, B. Trease, J. Arenas, and J. Geiger, *Design and application of compliant mechanisms for surgical tools,* (2005).

[7] F. S. Eastman, *Flexure pivots to replace knife edges and ball bearings* (Univ. Wash Engng Exp. Sta. Bull. No. 86., 1935).

[8] D. Wiersma, S. Boer, R. Aarts, and D. Brouwer, *Design and performance optimization of large stroke spatial flexures,* Journal of Computational and Nonlinear Dynamics **9** (2014), 10.1115/1.4025669.

[9] M. Naves, D. Brouwer, and R. Aarts, *Building block-based spatial topology synthesis method for large-stroke flexure hinges,* Journal of Mechanisms and Robotics **9** (2017), 10.1115/1.4036223.

[10] S. Henein, P. Spanoudakis, S. Droz, L. I. Myklebust, and E. Onillon, *Flexure pivot for aerospace mechanisms,* in *10th European Space Mechanisms and Tribology Symposium, San Sebastian, Spain* (Citeseer, 2003) pp. 285–288.

[11] S. Awtar, *Analysis and synthesis of planer kinematic xy mechanisms,* Cambridge MA, Massachusetts Institute of Technology (2004).

[12] *Precision systems design laboratory (psdl),* `https://psdl.engin.umich.edu/nanopositioning.php`, accessed: March 2021.

[13] E. Merriam, J. Jones, S. Magleby, and L. Howell, *Monolithic 2 dof fully compliant space pointing mechanism,* Mechanical Sciences **4**, 381 (2013).

2

THE STAGE METHOD FOR SIMULTANEOUS DESIGN OF THE STRESS AND GEOMETRY OF FLEXURE MECHANISMS

Current design methods for flexure (or compliant) mechanisms regard stress as a secondary, limiting factor. This is remarkable because stress is also known as a useful design parameter. In this paper we propose the Stress And Geometry (STAGE) method, to design the geometry of a flexure mechanism together with a desired stress field. From this design, the stress-free to-be-fabricated geometry is computed using the inverse finite-element method. To demonstrate the potential of the method, the geometry of the well-known crossed-flexure pivot is taken as example. We first show how this mechanism can be redesigned for the same functional geometry with various internal stresses. This results for a specific choice of stress field in a design of a crossed-flexure pivot with 23% lower peak stresses during motion as compared to the known designs, for a ±45 degrees rotation. We then present a second example, of a Folded Leaf Spring (FLS). With a parameter sweep the optimal stress field is calculated, showing a peak stress reduction of 28% during motion. This result was validated with an experiment, showing a normalized mean absolute error of 5.5% between experiment and theory. With a second experiment it was verified that the functional geometry of the FLS with internal stresses was equal to the one without internal stresses, with geometric deviations smaller than half the thickness of the flexures.

This chapter is to be submitted to Precision Engineering

2.1. INTRODUCTION

Flexure mechanisms use elastic deformation of slender segments to achieve motion, which results in a highly repeatable behavior due to the absence of friction and backlash. The design of these mechanisms is not trivial and multiple design methods exist, either based on degrees-of-freedom and constraints [1–3], rigid-body representations [4], the combination of simple building blocks to form more complex mechanisms [5–7] or structural optimization techniques [8].

The mentioned design methods focus mainly on the geometry of the mechanism and regard stress as a resulting, limiting factor. This is remarkable since stress is also known as a useful design parameter. Examples in engineering are the reduction of tensile forces in concrete by preloaded rods, avoidance of buckling by preloading bicycle spokes [9], and the preloading of bolts to mitigate their load cycle amplitude. Specific examples in the flexure mechanisms field are the introduction of clamping forces and elimination of backlash by a preloaded member [10], the introduction of multi-stable states using snap-through elements [11, 12], and the reduction of stiffness using preloaded elements with negative stiffness [13, 14].

A general method to design stresses in flexure mechanisms is not available, but various strategies to manipulate stresses for a specific geometric design are known. These strategies mainly aim to avoid stress concentrations. A first strategy is to opt for distributed instead of lumped compliance by using blade or wire flexures instead of notch hinges [8]. The stresses can be further smoothened by gradually increasing the thickness of the flexures at regions with stress concentrations [15, 16], although this generally results in higher stresses in other regions due to the increased stiffness. Another strategy is to connect multiple flexures in series to reduce the required stroke of each element [17]. Although these strategies are effective, a major disadvantage they have is that the functional geometry originally intended by the designer is changed, leading to significantly sub-optimal designs.

In this paper we propose the Stress And Geometry (STAGE) method, to design the stresses and geometry of flexure mechanisms simultaneously. The functional geometry of the mechanism is designed together with a desired stress field, from which the stress-free, to-be-fabricated geometry is computed using the inverse finite-element method.

In section 2.2, the STAGE method is presented and explained in detail, by applying it to the well-known crossed-flexure pivot (CFP) as an example. In section 2.3 we demonstrate the potential of the method for designing a CFP with reduced peak stresses for large rotations, resulting in a new stress-free fabrication geometry. In section 2.4, we present a second application example to reduce peak stresses, this time using a parameter sweep to find the most optimal stress field for a folded leaf spring. Two experimental tests have been conducted to validate the outcomes. In section 2.5 we reflect on the results of the paper and in section 2.6 we summarize the contributions of this work.

2.2. The STAGE method

The goal of the STAGE method is to simultaneously design the stresses and the functional geometry of a flexure mechanism. Figure 2.1 shows an overview of the method with four steps. First the functional geometry is designed. The focus in this step is on the kinematics of the mechanism, for which currently available design methods can be used. At step two the stresses in the mechanism are designed by determining the possible stress fields and selecting one. At the third step, the inverse finite-element method is used to compute the stress-free fabrication geometry, required for production. At step four, the fabricated shape is assembled, after which it attains the functional geometry while exhibiting the desired stresses. In between steps 1 and 2 there can be iterations in order to obtain the optimal functional geometry and internal stresses. The four steps will now be explained in detail.

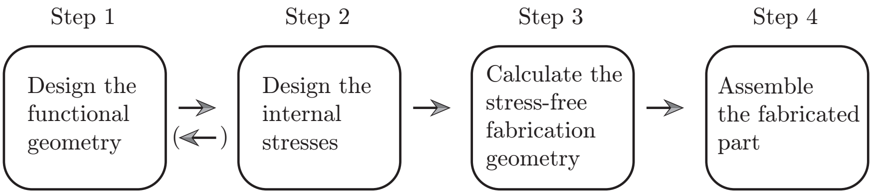
Step 1
Design the functional geometry
Step 2
Design the internal stresses
Step 3
Calculate the stress-free fabrication geometry
Step 4
Assemble the fabricated part

Figure 2.1: Steps of the STAGE method to design the stresses and the functional geometry of a flexure mechanism simultaneously.

2.2.1. Step 1: Design the functional geometry

The STAGE method starts with designing the functional geometry of the flexure mechanism. The focus in this step is on the kinematics of the mechanism, for which the currently available design methods [1–8] can be used, for example to obtain a linear guide or rotational hinge with different functional geometries. Instead of designing something new in this paper, for explanation of the method we have chosen the well-known crossed-flexure pivot (CFP) in Fig. 2.2 as an example of a desired functional geometry. The CFP design dates back to at least 1948 and initially served to replace knife-edge bearings [15, 18–20]. It consists of two thick plates connected by diagonal flexures. By bending of the flexures, the plates rotate with respect to each other. Table 2.1 shows the chosen properties of the CFP for this example. The lower plate is considered as the base.

Figure 2.3 illustrates the four steps of the STAGE method, with the CFP design as the resulting functional geometry in step 1, modeled using a two-dimensional representation.

2.2.2. Step 2: Design the internal stresses

In step two of the STAGE method, the internal stresses of the flexure mechanism are designed. For this a ‘release point’ is defined, where the mechanism is virtually cut open and where a force and moment are modeled, as shown in Fig. 2.3b. The force and moment define the stresses in the mechanism and will also be the input for step 3 in which

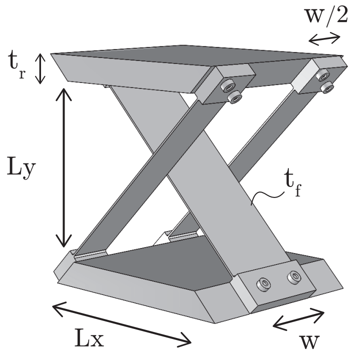

Figure 2.2: The well-known crossed-flexure pivot (CFP) [15, 18–20], which is chosen as example for explanation of the STAGE method.

Table 2.1: Properties of the CFP in Fig. 2.2.

Lx	100 $[mm]$
Ly	100 $[mm]$
w	30 $[mm]$
t_f	0.5 $[mm]$
t_r	10 $[mm]$
Young's modulus	114 [GPa]
Poisson's ratio	0.33 [−]

the fabrication geometry is calculated. In this section we present a graphical approach which helps to relate the stress fields and the modeled force and moment. We start with a single blade flexure, then generalize the theory to a more complex flexure system and finally apply the theory to the CFP.

In a two-dimensional representation, a blade flexure is essentially a slender beam in which stresses are induced by moments and transverse and axial forces. In general, the stresses in such a slender beam are dominated by its internal moments [21], and can be computed as [21]:

$$\sigma = M_i \frac{t_f}{2I}, \tag{2.1}$$

where σ is the maximum stress in the cross section, M_i is the internal moment in point i of the beam, t_f is the thickness of the beam, and I is the area moment of inertia belonging to the bending direction. Equation 2.1 shows that the stress and internal moment have a proportional relation which is solely dependent on the cross section of the beam. This means that we can use internal moments to visualize the stresses in flexure mechanisms if these are composed of slender flexures.

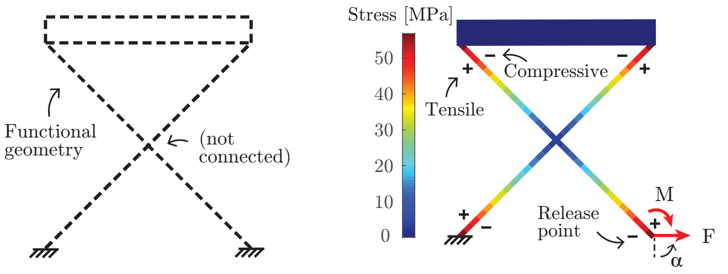
Functional
geometry
(not
connected)
Stress [MPa]
50
40
30
20
10
0
Compressive
Tensile
Release
point
M
F
α
+
−

(a) Step 1: Design of the functional geometry.

(b) Step 2: Design of the internal stresses by modeling a force and moment in a 'release point'.

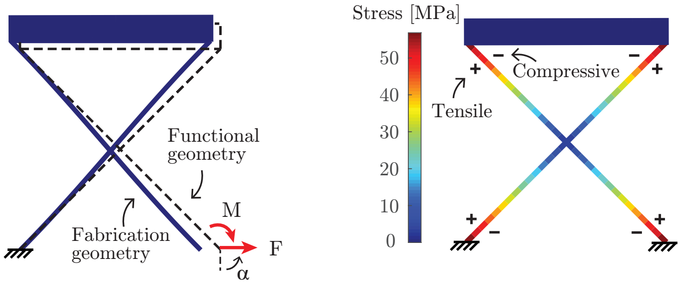
Functional
geometry
Fabrication
geometry
M
F
α
Stress [MPa]
50
40
30
20
10
0
Compressive
Tensile
+
−

(c) Step 3: Calculation of the stress-free geometry for fabrication.

(d) Step 4: Assembly of the fabricated part to obtain the functional geometry with the desired stresses.

Figure 2.3: The four steps of the STAGE method, explained with the crossed-flexure pivot. The geometry in the last step is the same as in the first step and exhibits the desired stresses.

In Fig. 2.4, a slender cantilever is illustrated, representing a blade flexure subjected to a force and moment. The graph shows its internal moment, derived using static equilibrium as [21]:

$$M_i(s) = cos(\alpha)F(L-s)-M, \tag{2.2}$$

where s is the coordinate along the length axis, L is the length of the beam and α is the angle of the force, as indicated in Fig. 2.4. The moment graph is a linear function. Also, it is independent of the cross section and stiffness of the beam because the system is statically determinate: the internal moments can be derived using solely static equilibrium equations.

Figure 2.5 shows how this theory applies for a slender beam with arbitrary curvature. The beam is considered fixed in the bottom left corner with a force F and a moment M acting in the right extremity of the beam. Here the internal moments are represented by

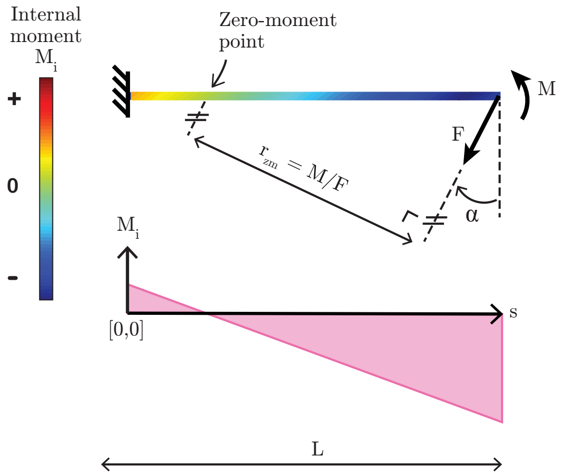

Figure 2.4: The internal moment distribution (bottom) in the cantilever beam (top) can be modified by the applied force and moment. For slender beams, this distribution is proportional to the stress field.

a linear field, with colors depicting the values. For a point i in the beam (and also in any point within the rest of the field) the internal moment can be calculated as:

$$M_i(r) = Fr - M, \tag{2.3}$$

where r is the moment arm between the point i and the line of action of the modeled force F. The line of points where $M_i(r)$ is zero is named the 'zero-moment line' as illustrated in Fig. 2.5. This is a unique feature in the visualization of the moment field.

Three design rules can be defined, relating the moment field to the modeled force and moment:

Rule 1 *The zero-moment line is always parallel to the direction of the modeled force.*

Two points in the field will experience the same internal moment if they have the same moment arm r with respect to the direction of the modeled force, as can be derived from equation 2.3. This also relates the points with zero moment.

Rule 2 *The distance between the zero-moment line and the line of action of the modeled force is* $r_{zm} = M/F$.

For points with moment arm $r = r_{zm}$ in equation 2.3, the moment applied at the end of the beam is in equilibrium with the moment due to the force at the end of the beam. Therefore the internal moment (and the bending stress) is zero at these points.

Rule 3 *The gradient of the moment field in the direction perpendicular to the zero-moment line is equal to the magnitude of the modeled force.*

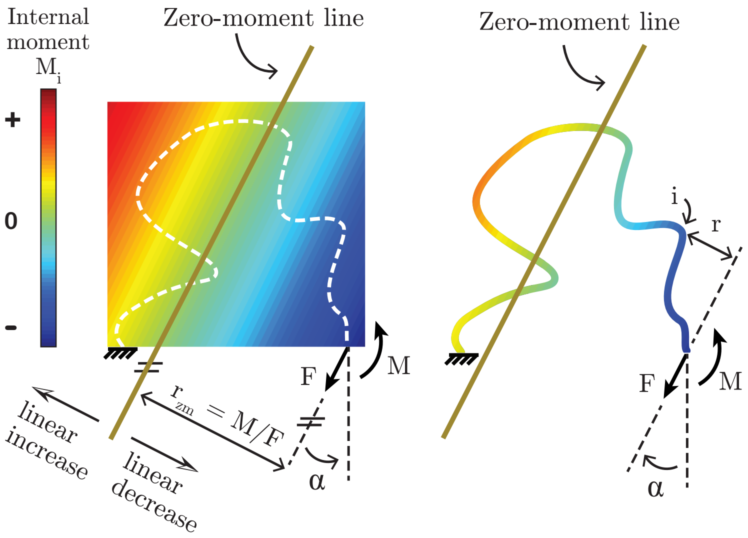

Figure 2.5: The internal moment field in an arbitrarily curved beam can be modified by means of a force F and a moment M in a point of the beam. The moment field is linear and can be visualized using the zero-moment line.

Equation 2.3 shows that the moment field is linear with a gradient of $\partial M_i/\partial r = F$.

We will now demonstrate the theory by designing the stresses in the CFP. First, a desired stress field is converted to a moment field, which is then used to calculate the required force and moment in a chosen release point. Suppose that we want the CFP to exhibit the stress field shown in Fig. 2.6a (in section 2.3 we will show that this particular stress field results in decreased peak stress during motion, compared to the traditional CFP design). A stress of ±57 MPa is defined in the four extremities of the flexures and between these points the field is assumed to be linear. The plus and minus signs indicate tensile and compressive stresses at the sides of the flexures, respectively. We convert these desired stresses into internal moments using equation 2.1 and the parameter values in table 2.1, which yields the moment field shown in Fig. 2.6b. A release point is chosen at the bottom right corner since this is a practical place to intersect the mechanism and assemble it after production of the fabrication geometry. Theoretically, however, any point in the mechanism could be chosen as a release point. The zero-moment line shows to be horizontal, laying in the middle of the four extremities as indicated. The distance between the zero-moment line and the release point therefore is $r_{zm} = L_y/2 = 50mm$. Then, following design rule 1, the modeled force in the release point should be parallel to the zero-moment line, which means that it should be horizontal in this case. The magnitude of the modeled force is equal to the gradient of the moment field according to rule 3, which yields $F = 71\ \text{Nmm}/50\ \text{mm} = 1.42\ N$. The modeled moment is calculated using the relation $r_{zm} = M/F$ from design rule 2, resulting in $M = -71$Nmm, which is correct because it is the opposite of the internal moment in that point.

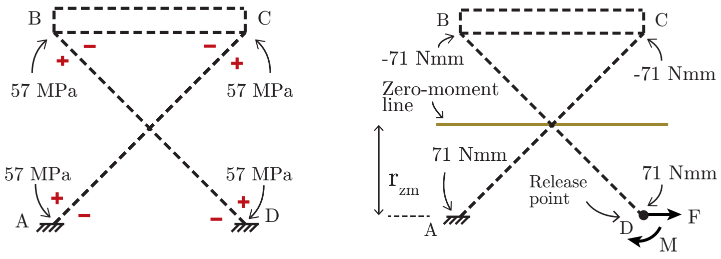

(a) Desired designed stress field

(b) Corresponding moment field

Figure 2.6: (a) The desired stress field defined at four points, where the plus and minus signs indicate tensile and compressive stresses at each side of the flexures; (b) Internal moments calculated from the stress field, with corresponding zero-moment line from which the modeled force and moment are derived.

2.2.3. STEP 3: CALCULATE THE STRESS-FREE FABRICATION GEOMETRY

In step three of the STAGE method, the stress-free fabrication geometry is computed. This is an inverse problem since from the stressed functional geometry with the modeled forces and moments acting on it, the stress-free geometry has to be obtained. If the deflections are sufficiently small, the stress-free geometry can be calculated using linear beam theory. However, if the deflections are large and no analytical solution is available, nonlinear inverse FEM can be used. Originally proposed in [22], inverse FEM was introduced to the flexure mechanisms community by [23]. The authors use finite beam elements, which are specifically suited for flexure mechanisms. In this section we start by explaining regular nonlinear FEM, and then show the difference with inverse FEM. Because the solution method is somewhat counter-intuitive, an illustrative example for a rigid-body mechanism is provided in appendix A.

In FEM, the investigated geometry is first discretized and represented with (beam) finite elements connected by nodes. The internal forces due to deformation are computed as (using a co-rotational formulation as described in [24]):

$$\mathbf{F}_{int} = \sum_{n=1}^{N} \mathbf{T}_n^{\mathsf{T}} \mathbf{k}_n \mathbf{u}_n, \tag{2.4}$$

where $\mathbf{F}_{int}$ is a vector containing the forces on each node, $\mathbf{k}_n$ is the element stiffness matrix, $\mathbf{u}_n$ is the displacement vector in local coordinates for the nth element, $\mathbf{T}_n$ is the coordinate transformation matrix for the nth element, and N is the total number of elements. The goal of the FEM analysis is to solve a residual equation containing the force imbalance, which is described as

$$\mathbf{R}(\mathbf{U}) = \mathbf{F}_{int}(\mathbf{U}) - \mathbf{F}_{ext} = \mathbf{0}, \tag{2.5}$$

where $\mathbf{U}$ is the displacement vector containing nodal translations and rotations in global coordinates. For large deflections, $\mathbf{F}_{int}(\mathbf{U})$, and therefore $\mathbf{R}(\mathbf{U})$, is in general nonlinear.

The solution to the residual equation can be found iteratively using Newton-Raphson with the gradient

$$\mathbf{K} = \frac{\partial \mathbf{R}(\mathbf{U})}{\partial \mathbf{U}}. \tag{2.6}$$

The residual equation in equation 2.5 is written in terms of the displacement vector U. To explain the difference between forward and inverse FEM, it is useful to write the residual equation in terms of the unstressed and stressed geometries instead. This can be done using the fact that the displacements are the difference between the stressed and the unstressed geometries. This means that:

$$\mathbf{U} = \mathbf{X}_s - \mathbf{X}_0, \tag{2.7}$$

where $\mathbf{X}_0$ and $\mathbf{X}_s$ are vectors containing the nodal coordinates and rotations of the stress-free and stressed geometry, respectively. We can now rewrite the residual equation as:

$$\mathbf{R}(\mathbf{X}_0, \mathbf{X}_s) = \mathbf{F}_{int}(\mathbf{X}_0, \mathbf{X}_s) - \mathbf{F}_{ext} = \mathbf{0}. \tag{2.8}$$

For regular, forward FEM, $\mathbf{X}_0$ is known and $\mathbf{X}_s$ can be found using the gradient of the residual equation

$$\mathbf{K}_{fwd} = \frac{\partial \mathbf{R}(\mathbf{X}_0, \mathbf{X}_s)}{\partial \mathbf{X}_s}. \tag{2.9}$$

For inverse FEM, on the contrary, $\mathbf{X}_s$ is known and $\mathbf{X}_0$ has to be found. We again use the gradient of the residual with respect to its unknowns, which is in this case

$$\mathbf{K}_{inv} = \frac{\partial \mathbf{R}(\mathbf{X}_0, \mathbf{X}_s)}{\partial \mathbf{X}_0}. \tag{2.10}$$

The residual equations of the forward and inverse analysis are the same, but different variables in the equation are unknown. Because of this, a different gradient needs to be computed to find the solution, while the rest of the calculations are similar for both analyses.

Instead of inverse FEM analysis, also regular nonlinear optimization methods for compliant mechanisms could be used to compute the stress-free geometry. However, in comparison the inverse FEM has a significantly lower computational cost since the nonlinear residual equations have to be solved only once [23].

MATLAB MODEL

Using the method described in section 2.2.3, a FEM code was written in Matlab for the computations in this article. We will refer to this as the ‘Matlab model’. The computations are checked using the commercially available software package Ansys and by experiments, in sections 2.3 and 2.4.

2.2.4. STEP 4: ASSEMBLE THE FABRICATED PART

In step four of the STAGE method the stress-free fabricated mechanism is assembled. As shown in Fig. 2.3d, it attains the functional geometry of step 1, and exhibits the desired stresses of step 2. The reactions on the lower right attachment point are equal to the force and moment modeled in the release point in step 2. We have now obtained a flexure mechanism with both a designed geometry and designed internal stresses.

2.2.5. DISCUSSION ON THE STAGE METHOD

Instead of using the STAGE method, direct prestress could be used to introduce stresses in a flexure mechanism. However, this will change its designed, functional geometry. For example, a flexure which is designed and fabricated as a straight member will become curved after pre-stress, which severely decreases its off-axis stiffness (stiffness in the supporting directions). Using the STAGE method, the functional geometry is unchanged after assembly.

The moment field in step two is independent of the functional geometry if the mechanism is statically determinate, because in that case the moments are fully determined by static equilibrium equations. For example, the stiff bar in the CFP does not change the moment field. The same holds if its flexures would have different cross sections. Note however that in that case, a different proportionality between stress and moments has to be taken into account, according to equation 2.1: thicker flexures subjected to the same moment will experience a lower stress. The independency of the moment field also allows to reconsider the functional geometry in step two. If a flexure is drawn in a certain moment field, it will attain the moment values of that field. This way, regions which are sensitive to fatigue failure could be designed such that they are close to the zero-moment line, and therefore experience lower bending moments.

The method to design the stresses in step two can be used directly if the mechanism is statically determinate, such as for the CFP. For statically indeterminate mechanisms, an approach can be to isolate a part of the mechanism such that a statically determined sub-mechanism is obtained. Alternatively, theory on statically indeterminate beam structures could provide a solution [21]. These approaches rely on stiffness and compatibility equations. If these approaches also do not suffice, a parameter sweep could be used. We will demonstrate this in section 2.4.

2.3. APPLICATION EXAMPLE: CFP WITH REDUCED PEAK STRESS

In this section we use the STAGE method to decrease peak stresses in the traditional CFP design during motion. The goal is to demonstrate one of the possible applications of the method. We first analyze the peak stresses of the traditional CFP at large rotations. From this, we determine a desired stress field which the CFP should exhibit in its central position. This stress field is introduced using the STAGE method. We then compare the stress peaks during motion of the traditional and the redesigned CFP. The outcomes are validated using the commercially available FEM software Ansys.

For large rotations, the flexures of the traditional CFP experience stress peaks close to their extremities, as shown in the FEM simulations in Fig. 2.7. The plus and minus signs indicate the tensile and compressive stresses at the sides of the flexures, respectively. The stress in point A ranges from -209.7 MPa to +96.05 MPa throughout the rotation. The peak stress can be reduced by introducing half of the difference, +56.83 MPa, at point A when the CFP is in its central position. This desired stress is shown in Fig. 2.6a. The desired stresses in points B, C and D have been determined using the same reasoning.

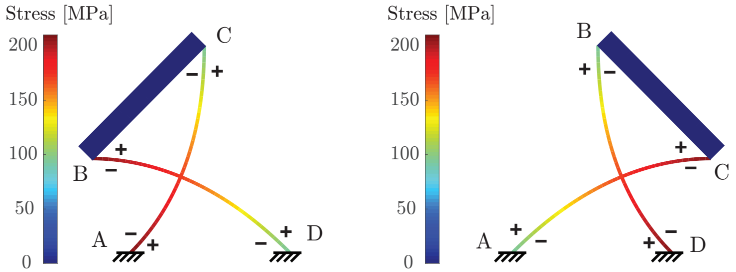

(a) +45 degrees rotation.

(b) -45 degrees rotation.

Figure 2.7: FEM simulations show the peak stresses of 210 MPa in the traditional CFP for large rotations.

Table 2.2: Check of the peak stresses with the Ansys model.

	Rotation angle [deg]	Peak stress Matlab [MPa]	Peak stress Ansys [MPa]	Error [%]
Traditional CFP	+45	209.742	209.517	0.107
	-45	209.742	209.517	0.107
Redesigned CFP	+45	161.295	161.123	0.107
	-45	161.296	161.308	0.007

Following sections 2.2.2, 2.2.3 and Fig. 2.3, the required stress-free fabrication geometry is obtained. After assembly, the redesigned CFP exhibits the stresses shown in Fig. 2.3d in its central position. At ±45 degrees rotation, it exhibits the stresses shown in Fig. 2.8. As compared to the traditional CFP, the stress field is significantly smoother and the peak stresses are 161 MPa, which is a reduction of 23%.

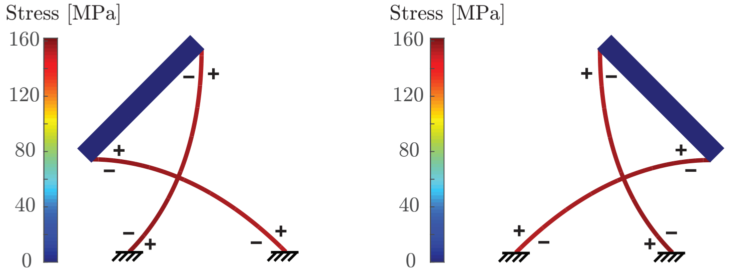

(a) +45 degrees rotation.

(b) -45 degrees rotation.

Figure 2.8: FEM simulations of the redesigned CFP showing peak stresses of 161 MPa, which is a reduction of 23 % compared to the traditional design. The fabrication geometry is shown in Fig. 2.3c.

The FEM results in this section are obtained using the FEM code written in Matlab in order to do the inverse computations, as described in section 2.2.3. The results were verified using Ansys as follows. First the fabrication geometry (shown in Fig. 2.3c) was imported in Ansys, virtually assembled and rotated 45 degrees back and forth. The peak stresses, occurring anywhere in the mechanism and anywhere in the motion range, were recorded. Beam 188 elements have been used, and the nonlinear analysis option was enabled. The stresses of the traditional CFP were also simulated in Ansys. In both simulations, 100 beam elements per flexure were used. Such a large number is not necessary for accuracy but allows to discretize the curved fabrication geometry of the redesigned CFP. The results are shown in table 2.2. The maximum error is 0.107 %, which can be considered small compared to the stress reduction. The Ansys APDL script containing the two full simulations is made available online.

As a second test, we simulated in Ansys how well the redesigned CFP attains the functional geometry after assembly. After assembly, the flexures should be straight, because the functional geometry has straight flexures. The maximum error in x and y direction of all nodal positions (101 per flexure) is 7.577e−4 mm, which can be considered significantly small as compared to the size of the total mechanism.

2.4. APPLICATION EXAMPLE: FOLDED LEAF SPRING WITH REDUCED PEAK STRESS

In this section we demonstrate the application of the STAGE method for reducing peak stresses in a folded leaf spring (FLS), by using a parameter sweep instead of the graphical approach in step 2 in order to find the optimal force and moment in the release point. This alternative approach can be useful if a desired stress field cannot be determined, or if the mechanism is too complex to use the graphical approach. The outcomes will be validated by two experimental tests and by Ansys simulations.

2.4.1. THE FOLDED LEAF SPRING

Figure 2.9 shows the folded leaf spring (FLS), which is well-known in industry but significantly less present in literature [25–27]. The FLS can be used to replace a wire flexure [25] and five or six FLS-elements can form a linear guide [25, 26]. In such a linear guide, a single FLS performs the up- and down motions shown in Fig. 2.10. The FEM simulations, based on the properties shown in table 2.3, show significant peak stresses in the flexure. The highest peak stress in the motion range of ±30 mm of the traditional FLS is 482.6 MPa.

Table 2.3: Properties of the folded leaf spring in Fig.2.9, used for analysis.

Lx	100 $[mm]$
Ly	50 $[mm]$
w	20 $[mm]$
t_f	0.5 $[mm]$
Young's modulus	114 [GPa]
Poisson's ratio	0.33 [−]

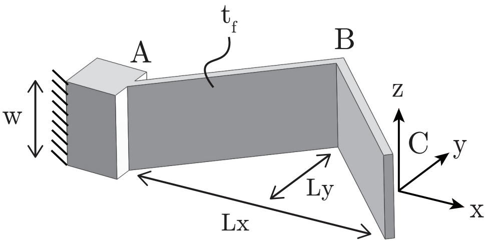

Figure 2.9: A folded leaf spring (FLS) with a fixed base.

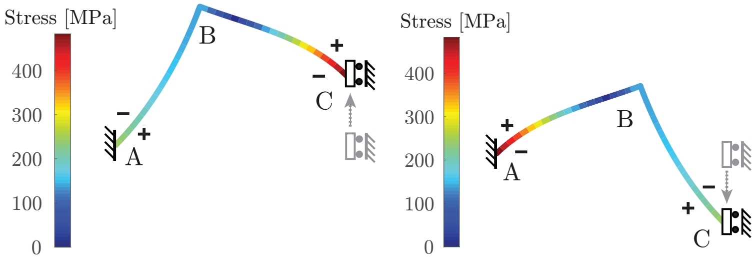

(a) After +30 mm displacement.

(b) After -30 mm displacement.

Figure 2.10: FEM simulations showing high peak stresses (482.6 MPa) in the traditional FLS at large displacements.

2.4.2. REDESIGN WITH THE STAGE METHOD AND A PARAMETER SWEEP

The goal here is to reduce peak stresses in the FLS while keeping its functional geometry unchanged. Therefore, we define the FLS design in Fig. 2.9 as the functional geometry in step 1 of the STAGE method. Step 2 is the design of a stress field and modeling of this field by a force and moment in a release point. We choose point C in Fig. 2.10 as a release point. We could have chosen any point in the flexure, but point C is a practical choice for assembling the produced geometry. We will use a parameter sweep to find the optimal force and moment in the release point. The parameter sweep encompasses steps 2, 3 and 4 of the STAGE method by varying the modeled force, its angle and the modeled moment, then calculating the respective fabrication geometry and analyzing the peak stresses of the assembled mechanism by moving it up and down ± 30 mm, as shown in Fig. 2.10. The design with the lowest peak stress is selected as a final result.

2.4.3. OPTIMAL REDESIGNED FLS

Figure 2.11 shows the optimal FLS design resulting from the parameter sweep with a peak stress of 347.1 MPa during motion, which is a reduction of 28% as compared to the traditional FLS in Fig. 2.10. Figure 2.11a shows its stress-free fabrication geometry and Fig. 2.11b shows the FLS after assembly. The peak stress of 347.1 MPa is reached in the extreme positions of ± 30 mm shown in Figs. 2.11c and 2.11d. The modeled force, force angle and moment in the release point corresponding to this design are resp. 6.76 N, 90.5 deg (approximately horizontal as shown in Fig. 2.11a), and 97.72 Nmm.

It is noted that a similar stress reduction cannot be achieved by simply shifting the motion range of the traditional FLS. The traditional FLS experiences the same peak stress in both the up- and down positions due to its symmetry along the vertical axis. Shifting the motion range will result in a lower peak stress in one direction, but in a higher peak stress in the other direction.

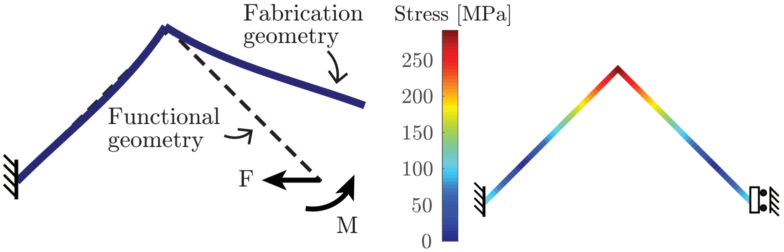

(a) Stress-free fabrication geometry.

(b) Assembled in the central position.

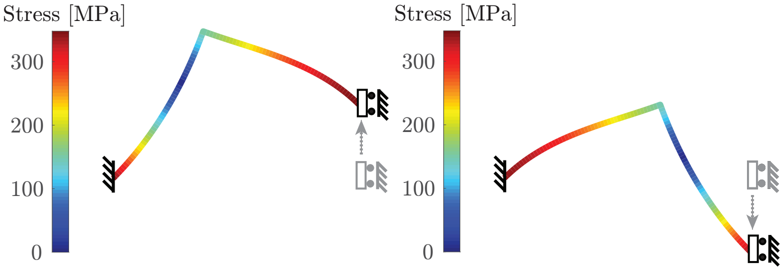

(c) After +30 mm displacement.

(d) After -30 mm displacement.

Figure 2.11: The redesigned folded leaf spring, showing a reduced peak stress of 28% as compared to the traditional FLS. This peak stress reduction cannot be achieved by shifting the motion range.

2.4.4. EXPERIMENTAL VALIDATION OF THE PEAK STRESS REDUCTION

The peak stress reduction in the FLS was validated by measuring the reaction forces and reaction moment in the attachment point A in Fig. 2.12 during motion, and comparing these to the FEM simulation data. This indirect approach is possible since the stresses throughout the entire FLS are determined by the reaction forces and reaction moment because the FLS is a statically determinate structure, as was explained in section 2.2.2.

Both the traditional and redesigned FLS were fabricated from Titanium grade 5 using Wire Electrical Discharge Machining (WEDM). The properties of the traditional FLS are shown in table 2.3. The redesigned FLS has the same width w and thickness t_f, but has a curved fabrication geometry shown in Fig. 2.11a, of which the data of the detailed shape is made available online. Figure 2.12 shows the setup used to measure the reaction forces and reaction moments of the FLS during motion. Point A of the FLS is attached to the base via a six degrees-of-freedom force and moment sensor (ATI MINI40-SI-40-2). Point B of the FLS is attached to a slider. The slider allows a rotation along its motion axis, which is needed to avoid forces due to misalignments. The displacement of the

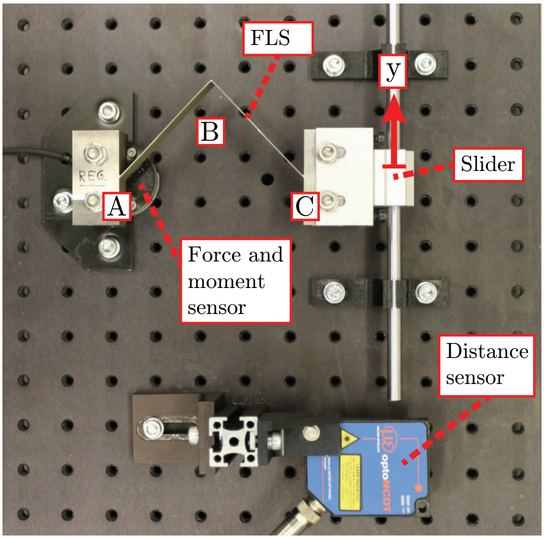

Figure 2.12: Experimental setup used to validate the stress reduction by measuring the reaction forces and the reaction moment of the traditional and the redesigned FLS.

slider in the y-direction is measured by an optical triangulation sensor (optoNCDT 1420). Both sensors are connected to a data acquisition unit (NI USB-6008) and a laptop for recording. In the experiments the slider was moved up and down four times slowly, to eliminate the influence of dynamic effects.

The mean of the measured reactions is taken as outcome. A Normalized Mean Absolute Error (NMAE) between model and experiment was computed, which is a regular MAE normalized by the maximum force:

$$\mathrm{NMAE} = \frac{\frac{1}{N}\sum_{n=1}^{N}|\hat{\zeta}_n - \zeta_n|}{max|\zeta|}, \tag{2.11}$$

in which N is the number of measured data points (at least 1500 in all measurements), $\hat{\zeta}_n$ the measured force and moment value and ζ_n is the value predicted by the FEM model written in Matlab. Figure 2.13 shows the experimental results of the traditional FLS design. The moment is divided by a characteristic length of 100 mm (the dimension of the FLS in x-direction) to make it compatible with the reaction forces. The NMAE between the FEM model in Matlab and the measurements of Fx, Fy, and M/100mm are 4.4%, 6.0% and 4.4%, respectively. Figure 2.14 shows the results of the redesigned FLS, together with the FEM data. The NMAE between the FEM model in Matlab and the measurements of Fx, Fy and M/100mm are 4.0%, 3.7% and 5.5%, respectively. The deviations between the experiments and the FEM models could be due to fabrication errors: a thickness variation in the flexures of 16 microns on the nominal thickness of 0.5 mm results in an error in the reaction force or reaction moment of 10%, due to the cubic relation between bending stiffness and flexure thickness. The stresses in the FLS scale proportionally to the reaction forces and reaction moments because bending stresses dominate and these

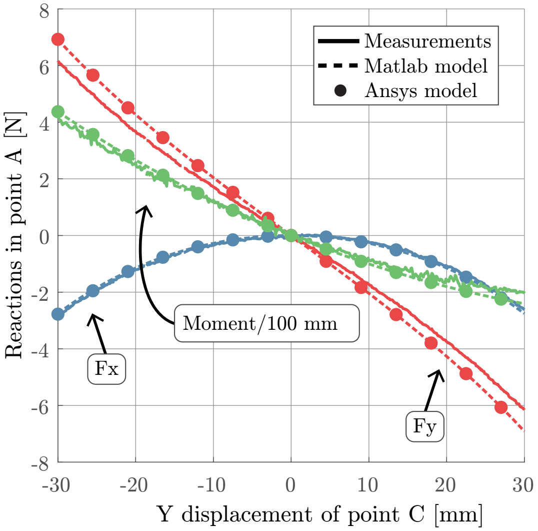

Figure 2.13: Experimental results of the traditional FLS compared to the two FEM models, showing a maximum NMAE of 6.0%.

scale proportional to force and moment. We conclude that the experiments validate the FEM models and thereby validate the peak stress reduction.

The errors between the Ansys model and the Matlab model are in the same order of magnitude of the round-off error (1e-3 mm) occurring when exporting the data.

2.4.5. EXPERIMENTAL VALIDATION OF THE FUNCTIONAL GEOMETRY

The goal of the second experiment is to measure how well the redesigned FLS obtains its functional geometry after assembly. Figure 2.15a shows the fabricated geometry of the redesigned FLS, while Fig. 2.15b shows the geometry after assembly, where it has obtained its functional geometry. In this evaluation, we will measure the waviness of the flexures from the images for both the redesigned and the traditional FLS as a reference case. The images are processed as follows.

First, two straight, connected line segments are drawn through the points A, B and C in Fig. 2.15b. The line segments are fitted such that a minimum waviness results.

Then, the deviations of the flexure edges with respect to these lines are plotted. The high-resolution pictures will be published online. Figure 2.16 shows the results for both the traditional and the redesigned FLS. Both plots show that the waviness is less than half the thickness of the flexure. This can be considered significantly small as compared to the deflections of the flexures during motion.

Additionally, the functional geometry is checked using Ansys. The fabrication geometry of the redesigned FLS is imported and virtually assembled. Using Beam 188 elements and the nonlinear analysis option enabled, the resulting maximum geometric error is 1e-3 mm, which is the same order of magnitude of the round-off error occurring when exporting the data.

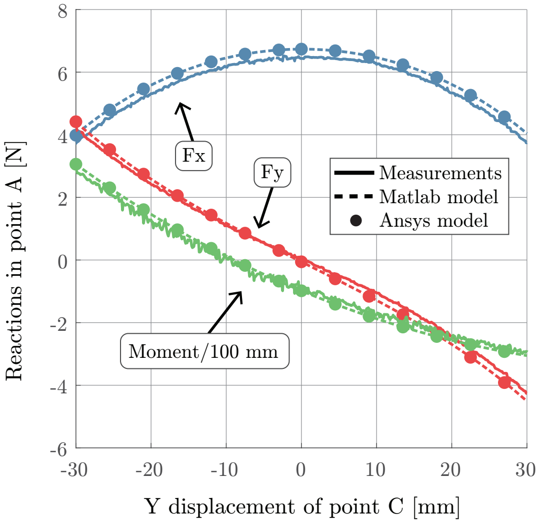

Figure 2.14: Experimental results of the redesigned FLS, compared to the two FEM models, showing a maximum NMAE of 5.5%.

2.5. DISCUSSION

The main idea behind the STAGE method is to consider the functional geometry and the fabrication geometry of a flexure mechanism as separate things. In current literature, the 'design of a flexure mechanism' refers to the functional geometry and also serves directly as the drawing for fabrication. This leads to the implicit assumption that the flexure mechanism on the drawing board is always stress-free, which is unnecessary and limits the solution space, as shown in this article by the redesigns of the CFP and the FLS.

Current CFP and FLS elements in machines could be directly replaced by the redesigned versions in this article because their attachment points remain unchanged. In fact, the replacement will not be visible to the naked eye because the only difference is that stresses are introduced. The WEDM fabrication technique used in this paper is commonly used for the production of flexure mechanisms in industry. This means that the curved geometries can also be produced using current production techniques.

This article showed the application of the STAGE method for peak stress reduction, but it could be used for other purposes. For example, actuation forces or eigenfrequencies could be reduced by designing the optimal stress fields, or deformations due to gravity could be mitigated. Furthermore, the functional geometry of the flexure does not necessarily have to be designed in its central position. For example, the functional geometry of the CFP could be designed at a 45 degrees rotation. If the flexures are designed as straight members in this configuration, the flexure will have a high support stiffness at this 45 degrees rotation. The STAGE method can be used to design the geometry of a flexure mechanism anywhere in its motion range.

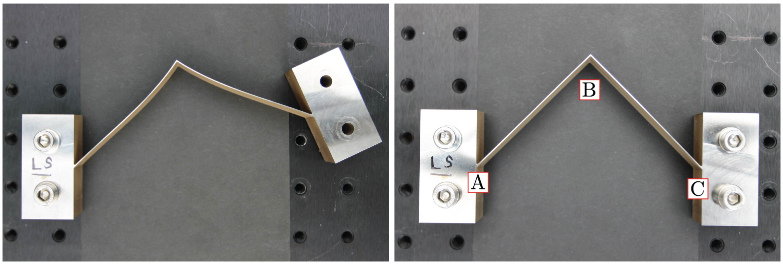

(a) (b)

Figure 2.15: The redesigned FLS in stress-free (as-fabricated) state (a) and after assembly in its central position (b).

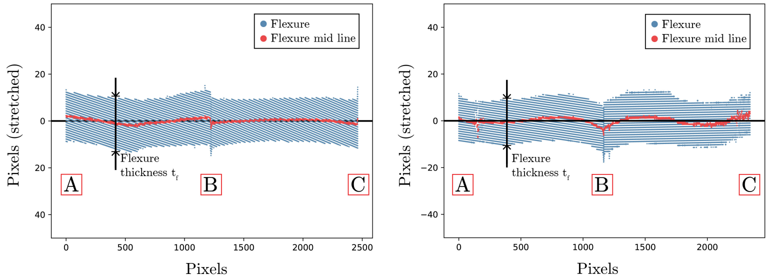

(a) Traditional FLS (b) Redesigned FLS after assembly

Figure 2.16: Waviness of the traditional (a) and redesigned (b) FLS after assembly, showing that the redesigned FLS attains the functional geometry well after assembly, with a waviness smaller than half the thickness of the flexures.

The amount of the peak stress reduction which can be achieved using the STAGE method is generally larger when the displacements of the flexures are large. For small displacements, the stress in each point is approximately equal in magnitude in both motion directions, meaning that the STAGE method will be less effective.

The flexures redesigned using the STAGE method are permanently stressed. Therefore a suitable material has to be selected for the mechanism to limit stress relaxation, similar to the design of springs used for permanent pre-stress.

2.6. CONCLUSIONS

In this work we proposed the Stress And Geometry (STAGE) method, to design the geometry and stress of flexure mechanisms simultaneously.

We have demonstrated the method by redesigning the stresses in the well-known crossed-flexure pivot, without changing its functional geometry, which resulted in a peak stress reduction of 23% for ± 45 degrees rotation.

Additionally, we showed how peak stresses in a folded leaf spring (FLS) can be reduced by 28%, using a parameter sweep to find the most optimal stress field. This alternative approach can be applied when it is not clear which stress field is most optimal, or if the mechanism is too complex.

The peak stress reduction in the FLS was validated by measuring its reaction forces during motion, showing a maximum normalized mean absolute error between model and experiment of 5.5%.

A second experiment showed that the functional geometry of the FLS is well attained after assembly, with a maximum waviness of half the flexure thickness.

ACKNOWLEDGMENT

This work is part of the research program “Möbius” with project number 14665, which is (partly) financed by the Netherlands Organization for Scientific Research (NWO).

REFERENCES

[1] J. B. Hopkins and M. L. Culpepper, *Synthesis of multi-degree of freedom, parallel flexure system concepts via freedom and constraint topology (fact)–part i: Principles,* Precision Engineering **34**, 259 (2010).

[2] J. B. Hopkins and M. L. Culpepper, *Synthesis of multi-degree of freedom, parallel flexure system concepts via freedom and constraint topology (fact). part ii: Practice,* Precision Engineering **34**, 271 (2010).

[3] L. C. Hale, *Principles and techniques for designing precision machines,* Tech. Rep. (Lawrence Livermore National Lab.(LLNL), Livermore, CA (United States), 1999).

[4] L. L. Howell, *Compliant mechanisms,* in *21st Century Kinematics* (Springer, 2013) pp. 189–216.

[5] C. J. Kim, S. Kota, and Y.-M. Moon, *An instant center approach toward the conceptual design of compliant mechanisms,* (2006).

[6] C. J. Kim, Y.-M. Moon, and S. Kota, *A building block approach to the conceptual synthesis of compliant mechanisms utilizing compliance and stiffness ellipsoids,* Journal of Mechanical Design **130** (2008).

[7] G. Radaelli, J. A. Gallego, and J. L. Herder, *An energy approach to static balancing of systems with torsion stiffness,* Journal of Mechanical Design **133** (2011).

[8] J. A. Gallego and J. Herder, *Synthesis methods in compliant mechanisms: An overview,* in *ASME 2009 International Design Engineering Technical Conferences and Computers and Information in Engineering Conference* (American Society of Mechanical Engineers Digital Collection, 2009) pp. 193–214.

[9] C. Burgoyne and R. Dilmaghanian, *Bicycle wheel as prestressed structure,* Journal of engineering mechanics **119**, 439 (1993).

[10] S. Awtar and J. M. Quint, *In-plane flexure-based clamp,* Precision engineering **36**, 658 (2012).

[11] B. D. Jensen and L. L. Howell, *Bistable configurations of compliant mechanisms modeled using four links and translational joints,* J. Mech. Des. **126**, 657 (2004).

[12] J. P. Stacey, M. P. O'Donnell, and M. Schenk, *Thermal prestress in composite compliant shell mechanisms,* Journal of Mechanisms and Robotics **11** (2019).

[13] J. van Eijk and J. F. Dijksman, *Plate spring mechanism with constant negative stiffness,* Mechanism and Machine Theory **14**, 1 (1979).

[14] K. Hoetmer, G. Woo, C. Kim, and J. Herder, *Negative stiffness building blocks for statically balanced compliant mechanisms: design and testing,* Journal of Mechanisms and Robotics **2** (2010).

[15] J. F. Gomez, J. D. Booker, and P. H. Mellor, *2d shape optimization of leaf-type crossed flexure pivot springs for minimum stress,* Precision Engineering **42**, 6 (2015).

[16] G. Krishnan, C. Kim, and S. Kota, *A metric to evaluate and synthesize distributed compliant mechanisms,* Journal of Mechanical Design **135** (2013).

[17] B. P. Trease, Y.-M. Moon, and S. Kota, *Design of large-displacement compliant joints,* (2005).

[18] W. Wittrick, *The theory of symmetrical crossed flexure pivots,* Australian Journal of Chemistry **1**, 121 (1948).

[19] J. Haringx, *The cross-spring pivot as a constructional element,* Flow, Turbulence and Combustion **1**, 313 (1949).

[20] F. Seelig, *Flexural pivots for space applications,* (1968).

[21] R. C. Hibbeler and S. Fan, *Statics and mechanics of materials*, Vol. 2 (Prentice Hall Upper Saddle River, 2004).

[22] S. Govindjee and P. A. Mihalic, *Computational methods for inverse finite elastostatics,* Computer Methods in Applied Mechanics and Engineering **136**, 47 (1996).

[23] A. E. Albanesi, M. A. Pucheta, and V. D. Fachinotti, *A new method to design compliant mechanisms based on the inverse beam finite element model,* Mechanism and Machine Theory **65**, 14 (2013).

[24] R. D. Cook, D. S. Malkus, M. E. Plesha, and R. J. Witt, *Concepts and Applications of Finite Element Analysis: 4th Edition* (2002).

[25] H. Soemers, *Design Principles for precision mechanisms* (T-Pointprint, 2011).

[26] A. Bos, *Position actuator for the ELT primary mirror*, Ph.D. thesis, Eindhoven University of Technology, The Netherlands (2017).

[27] L. Cacace, *An Optical Distance Sensor: Tilt robust differential confocal measurement with mm range and nm uncertainty*, Ph.D. thesis, Eindhoven University of Technology, The Netherlands (2009).

3

REDUCING ACTUATION FORCE AND PEAK STRESS OF A FLEXURE-BASED LINEAR GUIDE USING THE STAGE METHOD

Chapter 2 introduced the STAGE method, and showed its potential for peak stress reduction in two flexure mechanisms at large displacements. In this chapter we show how the method can be used to decrease actuation force in the linear guide from chapter 2. The STAGE method allows to reduce actuation force without changing its functional geometry and without adding elements, which is new with respect to literature. It also allows to simultaneously decrease peak stresses and actuation force in the linear guide and to make a trade-off between these two properties. In this chapter this is done using a parameter sweep, resulting in a design chart from which three redesigns are selected. The first has a reduction of actuation force of 96% at the cost of an increase in peak stress of 45% with respect to the traditional design. The second redesign has a similar peak stress as the traditional design, but a reduction in actuation force of 56%. The third redesign has both a reduction in actuation force (35%) and a reduction in peak stresses (28%). The actuation force of the traditional design and redesign 1 are tested experimentally, showing a reduction of 90% in peak actuation force. A second experiment shows that the redesign attains the functional geometry well after assembly, with geometric deviations of around half the thickness of the flexure.

This chapter is to be submitted to Mechanism and Machine Theory.

3.1. INTRODUCTION

In contrast to rigid-body mechanisms, flexure (or *compliant*) mechanisms use elastic deformation to gain mobility [1]. The principle of elastic deformation offers advantages such as the absence of friction and play, but also results in a stiffness in the motion direction which is often undesired because additional actuation force is required. This actuation force can be eliminated to a large extent by adding pre-stressed spring elements with a negative stiffness, an approach known as static balancing [2, 3]. Two strategies to design such elements can be distinguished. The first is a building-block approach, where the force-deflection characteristic of the element is designed such that it cancels out the actuation forces of the mechanism [4–7]. A second strategy is to simplify both the element and the flexure mechanism to a rigid-body mechanism with torsion springs [1]. This makes it possible to derive energy, force or stiffness equations which are then used to find the design parameters for which the mechanism is balanced [8–12]. In addition to the design strategies, numerical optimization can be used to obtain static balance [13, 14].

In this article, we will reduce the actuation force of a pre-existing linear guide flexure mechanism using the stress and geometry (STAGE) method from earlier work [15]. With the STAGE method, the geometry and stress of a flexure mechanism can be designed simultaneously. In this work we show that this allows to reduce the actuation forces of the linear guide by solely redesigning its stresses, without changing its geometry or adding elements such as in current literature. Furthermore, it allows to make a trade-off between actuation force and peak stresses, and to some extent reduce them simultaneously.

In section 3.2 we explain the pre-existing linear guide design and show how the STAGE method is used to reduce actuation forces and peak stresses. Three redesigns are selected from a design chart, of which one is tested experimentally in section 3.3. In section 3.4 we discuss the generality and implications of the work and in 3.5 we summarize the contributions to literature.

3.2. STATIC BALANCING OF THE LINEAR GUIDE DESIGN USING THE STAGE METHOD

In this section we first explain the design of the pre-existing linear guide flexure mechanism, which is based on six folded leaf springs (FLS). We then isolate one of the FLS elements, and explain the procedure used for static balancing using the STAGE method. This results in a design chart from which three designs are selected, all with a different actuation force and peak stress.

3.2.1. THE FOLDED LEAF SPRING LINEAR GUIDE DESIGN

Figure 3.1 shows the pre-existing linear guide consisting of six folded leaf springs [16–18]. This design is common in industry but has not been described extensively in literature. The folded leaf springs allow the linear motion of the middle body by in-plane bending, which is associated with a low stiffness. Motions in the other, undesired directions are constrained with a high stiffness because the leaf springs are loaded in their lateral directions in that case. Each folded leaf spring suppresses one degree of freedom of the middle body. This can be visualized by replacing each folded leaf spring by a thin rod (a wire flexure) through its fold line [16]. A more detailed explanation of the reasoning behind this is provided in [19, 20]. Five folded leaf springs suffice to create a linear guide and the sixth one is usually added to increase the stiffness in the supporting directions. Although the stiffness in the motion direction of the guide is generally orders of magnitude lower than the stiffness in supporting directions, it is still considerable and limits performance. Decreasing the motion stiffness significantly decreases the required actuator size and energy consumption.

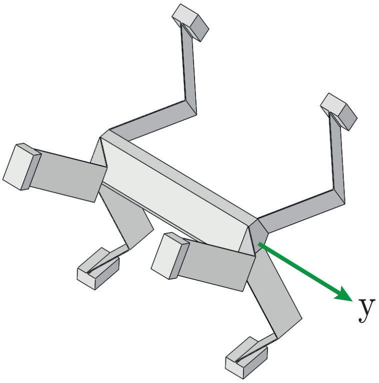

Figure 3.1: Pre-existing linear guide design [16–18] consisting of six folded leaf springs guiding a central body.

Figure 3.2 shows a single folded leaf spring, isolated from the linear guide design, and table 3.1 shows its properties. Figure 3.2b shows its deformations during motion in 2D, where the effect of the other five folded leaf springs is simulated by a slider. During the +-30 mm displacements, the peak stress is 483 MPa and the peak actuation force is 6.91 N.

Table 3.1: Properties of the FLS in Fig. 3.2.

Dimension	FLS
Lx	100 $[mm]$
Ly	50 $[mm]$
w	20 $[mm]$
t_f	0.5 $[mm]$
Young’s modulus	114 [GPa]
Poisson’s ratio	0.33 [-]

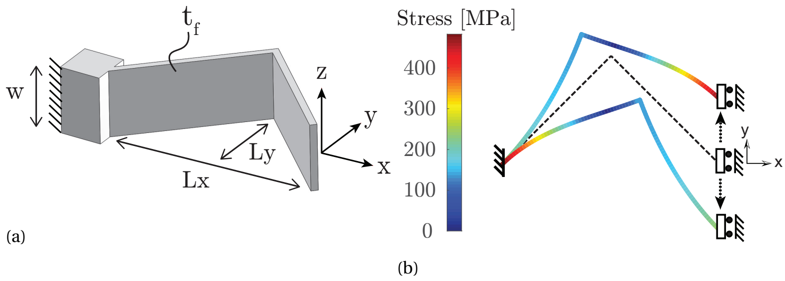

(a)

(b)

Figure 3.2: (a) The traditional folded leaf spring, shown isolated from the linear guide; (b) Deformations and stresses at the extreme displacements of +- 30 mm.

3.2.2. REDESIGNING PROCEDURE

In this section we explain how to use the STAGE method to decrease the actuation force and peak stresses of the FLS during motion. Figure 3.3 shows an overview of the procedure in five steps. The first four steps serve to introduce stress in the FLS without changing its functional geometry, and in the fifth step the performance is recorded. First, the functional geometry is defined, which is simply the FLS design from Fig. 3.2a. In step two, the mechanism is virtually cut and two forces and a moment are defined in that point. These determine the stresses in the flexure and are used as an input for step three, in which the stress-free fabrication geometry is calculated using an inverse finite-element model. The fabrication geometry is such, that after assembly shown in step four, it will attain the functional geometry while exhibiting the stresses introduced in step two. In step five, the performance is determined by evaluating the peak actuation force and the peak stresses in the flexure during motion. This performance is recorded for different stress fields. Technically this means that a parameter sweep is conducted where F_x, F_y and M form the input, and the peak actuation force and peak stress during motion form the output. In the following, the steps will be explained in more detail.

STEP ONE: DEFINE THE FUNCTIONAL GEOMETRY

In the first step, the functional geometry of the FLS is defined as shown in Fig. 3.3a. This is the geometry which is intended by the designer of the linear guide mechanism, providing the right kinematics for the design to work. This is commonly regarded as 'the design' of the folded leaf spring. All properties are defined except for the stresses.

STEP TWO: CHOOSE FORCES AND A MOMENT IN A RELEASE POINT

The second step of the STAGE method is to design stresses by virtually cutting the flexure and applying forces and a moment in this point, as shown in Fig. 3.3b. We call this particular point a release point, because it is 'released' when computing the fabrication geometry in step three. A different choice of forces and moment will result in different stresses.

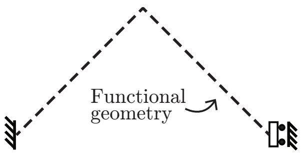

(a) Step 1: define the functional geometry.

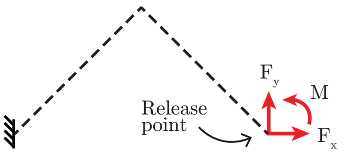

(b) Step 2: choose a force and a moment in a release point.

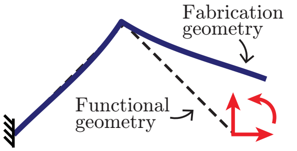

(c) Step 3: compute the fabrication geometry using inverse FEM.

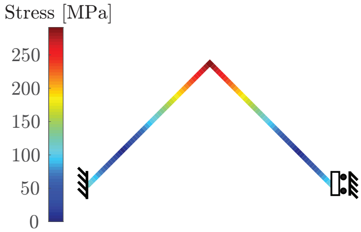

(d) Step 4: assemble.

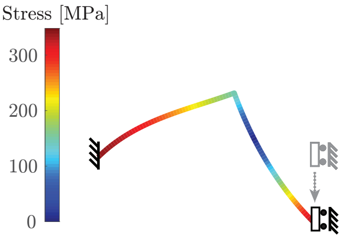

(e) Step 5: evaluate peak actuation force and stress (down).

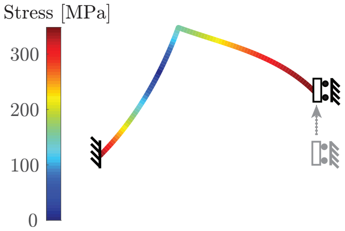

(f) Step 5: evaluate peak actuation force and stress (up).

Figure 3.3: Procedure for redesigning the stresses in the FLS. A sweep across the parameters F_x and F_y and M produces the design chart of Fig. 3.4.

STEP THREE: COMPUTE THE FABRICATION GEOMETRY USING INVERSE FEM

In step three, the stress-free fabrication geometry is computed. This is an inverse problem because the stressed functional geometry and the forces and moment defined in step two serve as an input, and the stress-free fabrication geometry is to be computed. Because of the nonlinearities arising in the large displacements, we use a non-linear inverse finite-element model to solve the problem. The inverse finite-element method was originally proposed in [21] and has been introduced to the compliant mechanisms community by [22]. It allows to find the stress-free geometry efficiently by solving the equilibrium equations just once, as opposed to the common shape optimization techniques often used for flexure mechanisms [22]. In this article, we use the Matlab code from [15], which will be validated using the commercial finite-elements package Ansys and experimental tests in section 3.3.

STEP FOUR: ASSEMBLE

In step four, the stress-free fabrication geometry is assembled as shown in Fig. 3.3d, where it attains the functional geometry defined in step one, while exhibiting the stresses introduced in step two. During assembly, the end point of the flexure is translated and rotated back to its original position and orientation.

Note that a different choice for the forces and moment in step two results in a different fabrication geometry and in different stresses after assembly, but does not change the geometry after assembly. This way, effectively only the stresses of the FLS are changed.

STEP FIVE: EVALUATE PERFORMANCE

For each different set of F_x, F_y and M chosen in step two, the peak actuation force and peak stress is recorded during a 30 mm up and down motion as shown in Figs. 3.3e and 3.3f. The peak stress is the maximum absolute stress anywhere in the flexure, anywhere in its displacement range.

3.2.3. RESULTING REDESIGNS

Figure 3.4 shows the results of the parameter sweep in the form of a design chart. Each dot represents a FLS with a different choice for F_x, F_y and M. The different parameters result in a different stress field after assembly but all redesigns have the same geometry after assembly, as explained in section 3.2.2. The performance of the traditional FLS design (for which $F_x = F_y = M = 0$) is also indicated. Three redesigns are selected and their performance relative to the traditional FLS is listed in table 3.2. The corresponding values F_x, F_y and M are listed in table 3.3. Figure 3.5 shows the fabrication geometries of the traditional FLS and the three redesigns.

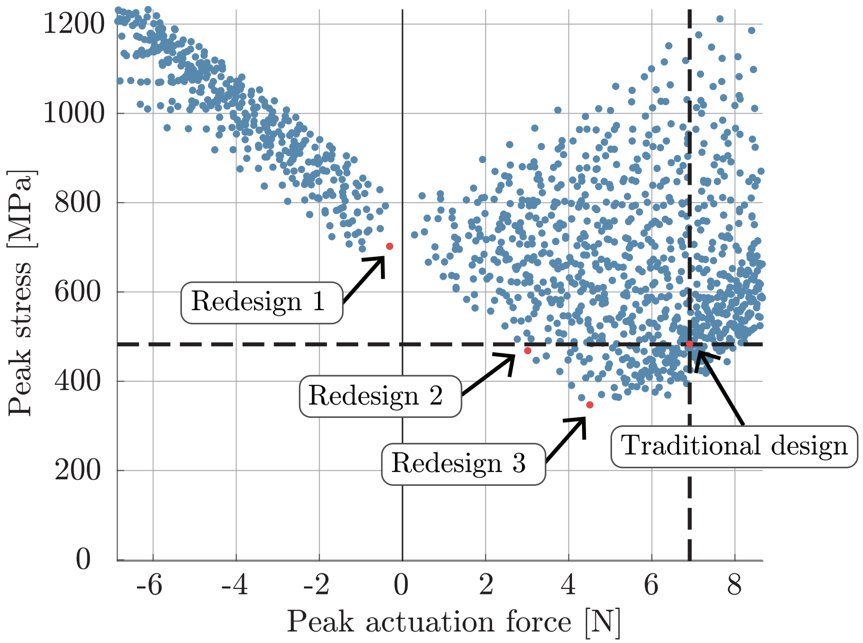

Figure 3.4: Design chart, resulting from the parameter sweep. Each dot represents a redesign with the same functional geometry but a different stress field, determined by F_x, F_y and M. The peak stress and actuation force during motion are recorded for each redesign and determine the position of the dot.

Table 3.2: Performance of the three selected redesigns from Fig. 3.4, relative to the traditional FLS.

Design	Peak act. force [N]	Peak stress [MPa]
Traditional	6.91 (100%)	483 (100%)
Redesign 1	-0.308 (-96%)	702 (+45%)
Redesign 2	3.01 (-56%)	469 (-2.9%)
Redesign 3	4.51 (-35%)	347 (-28%)

Table 3.3: Forces and moment belonging to the three selected redesigns selected from Fig. 3.4.

Design	F_x [N]	F_y [N]	M [Nmm]
Traditional	0	0	0
Redesign 1	-18.3	0.0720	441
Redesign 2	-11.0	0.146	219
Redesign 3	-6.73	0.0575	97.6

3.3. EXPERIMENTAL VALIDATION

In this section, we first validate the actuation force reduction of redesign 1 experimentally and numerically. A second experiment shows how well it attains its functional geometry after assembly in practice. The stress reduction of redesign 3 has been validated experimentally in [15].

3.3.1. TEST OF THE ACTUATION FORCE REDUCTION

Figure 3.6 shows redesign 1 as-fabricated (top) and after assembly (bottom). It is fabricated using wire-electrical discharge machining (WEDM) from titanium grade 5. The traditional FLS from Fig. 3.5a is also fabricated, using the same process, material and manufacturer.

Figure 3.7 shows the setup used to measure the actuation forces of the FLS designs during motion. The left side of the FLS is attached to the base via a force sensor (ATI MINI40-SI-40-2). The right side of the FLS is attached to a slider. The slider allows a rotation along its motion axis to avoid forces due to misalignments. The displacement in the y-direction is measured by an optical triangulation sensor (optoNCDT 1420). Both sensors are read out using a data acquisition unit (NI USB-6008) and a laptop. The slider is moved up and down four times and the averages of the measured values are computed and plotted in Fig. 3.8. The peak actuation force is 0.608 N for the redesign and 6.158 N for the traditional design, resulting in a 90% reduction observed in the experiment.

The FEM data in this section was generated using the FEM model written in Matlab from [15] and will be checked using the commercially available FEM software package Ansys. Beam 188 elements are used and the nonlinear analysis option is enabled. The difference between the actuation force predicted by the code written in Matlab and the Ansys simulations showed to be negligible compared to the achieved actuation force reduction, with an error smaller than 1-e3 N.

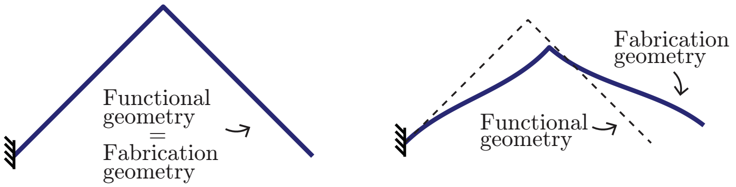

(a) Traditional design (b) Redesign 1

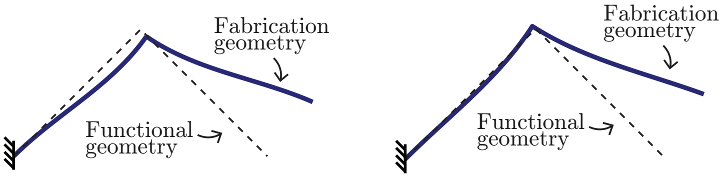

(c) Redesign 2 (d) Redesign 3

Figure 3.5: Fabrication geometries of the traditional FLS and the three selected redesigns from Fig. 3.4. After assembly, they all attain the same functional geometry, but with different stresses.

3.3.2. TEST OF THE GEOMETRY AFTER ASSEMBLY

A second experiment is carried out to test how well redesign 1 attains the functional geometry after assembly. Figure 3.6 shows redesign 1 as-fabricated (left) and after assembly (right), where it has obtained the functional geometry. The desired functional geometry consists of two connected straight lines AB and BC. The picture shown in Fig. 3.6b is processed with an automated script to show the waviness of both flexure segments AB and BC, and shown in Fig. 3.9. Here, the thin edge of the FLS is plotted on a horizontal line and highly stretched in the vertical direction.

Figure 3.9 shows that the waviness of the assembled redesign 1 is around half the thickness of the flexure. In [15] we have carried out a similar test for redesign 3 with a comparable result.

3.4. DISCUSSION

A first advantage of using the STAGE method to statically balance the linear guide is that its functional geometry is unchanged. A folded leaf spring linear guide in a machine could be replaced by one of the presented redesigns without a visible change: after assembly in the machine the sole difference is that the stresses in the mechanism have changed. The attachment points in the machine can be left unchanged. If the traditional linear guide would be balanced by simply adding pre-stress instead of using

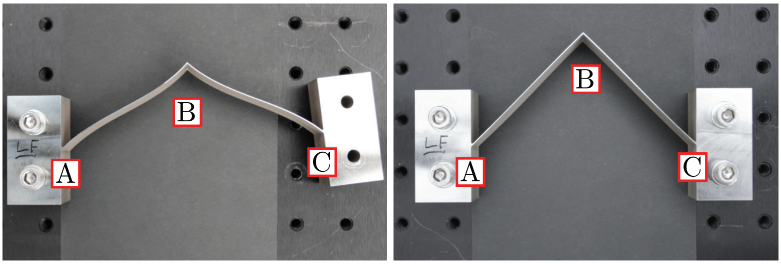

(a) (b)

Figure 3.6: Redesign 1 of the FLS in unstressed (as-fabricated) state (a) and after assembly (b).

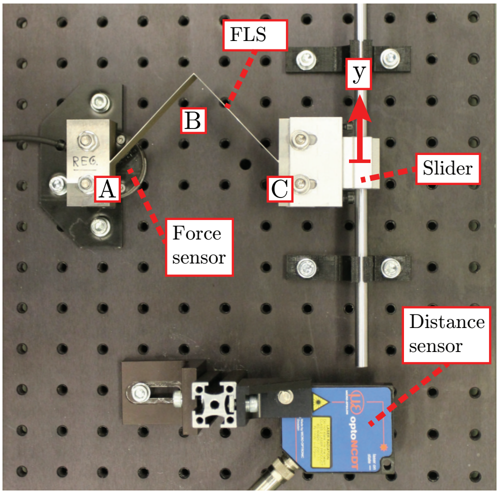

Figure 3.7: Setup used to validate the actuation force reduction of redesign 1.

the STAGE method, its geometry would change. The folded leaf springs would become curved, which significantly reduces their support stiffness [23, 24].

A second advantage is that no additional elements are needed such as in most current statically balanced designs. Often, these elements consist of a buckled blade flexure [4–7]. These increase build volume and could result in unwanted, low-frequency vibrations. An exception is the work of [9, 25], where a flexure-based transmission mechanism is balanced without additional elements, by pre-stressing. The support stiffness of this mechanism could be improved using the STAGE method by explicitly designing the flexures in their stressed states such that they are straight in certain desired positions.

A third advantage of the STAGE method is that the stresses are designed explicitly, which enables to simultaneously decrease the actuation force and peak stress in the linear guide. In current balancing methods, stresses are designed indirectly by regarding the force-deflection behavior or the total energy.

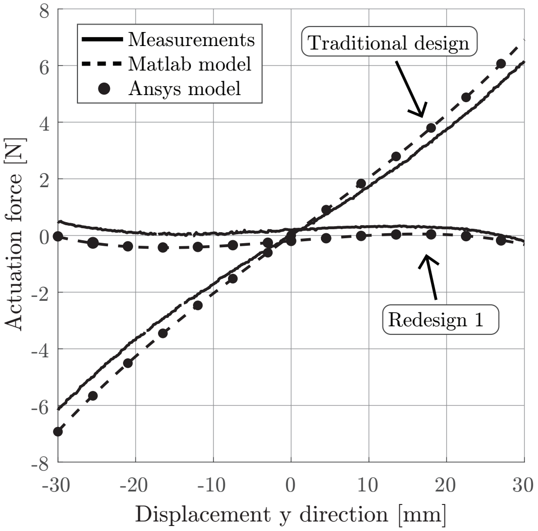

Figure 3.8: Actuation force of the traditional design and redesign 1 during motion. The measurement data shows a 90% reduction in actuation force.

The STAGE method can be used for static balancing, but is not a general balancing method. In the case of the linear guide, it was clear on forehand that this design had the potential of static balance. This is because a FLS element can be regarded as a spring placed perpendicular on a linear guide. Such a configuration is known to have a negative stiffness. Pseudo-rigid body models could be used to assess if a mechanism can be balanced without additional elements, before using the STAGE method.

In this article, we have regarded actuation force as an undesired property. It can however also be beneficial, for example to provide a clamping force or to balance gravity forces. The methods in this article could also be used to design a desired actuation force, by changing the scoring metrics on the two axes in the design chart in Fig. 3.4.

3.5. CONCLUSION

In this article we showed that the stress and geometry (STAGE) method from earlier work can be used to statically balance a pre-existing flexure-based linear guide. The method allows to statically balance the mechanism without changing its functional geometry and without adding elements, which is new with respect to current literature. The method results in a different fabrication geometry, which attains the functional (designed) geometry after assembly.

Because the stresses are designed directly using the STAGE method, it is possible to make a trade-off between peak stresses and peak actuation force. This was done using

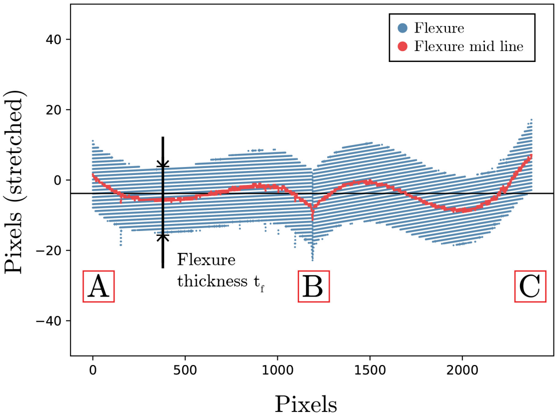

Figure 3.9: Waviness of redesign 1 after assembly.

a design chart, from which three redesigns were selected. The first has a reduction of actuation force of 96% at the cost of an increase in peak stress of 45% with respect to the traditional design. The second redesign has a similar peak stress as the traditional design, but a reduction in actuation force of 56%. The third redesign has both a reduction in actuation force (35%) and a reduction in peak stresses (28%).

The actuation force of the traditional design and redesign 1 were tested experimentally, showing a reduction of 90% in peak actuation force. A second experiment shows that the redesign attains the functional geometry well after assembly, with geometric deviations of around half the thickness of the flexure.

3.6. ACKNOWLEDGMENT

This work is part of the research program “Möbius” with project number 14665, which is (partly) financed by the Netherlands Organization for Scientific Research (NWO).

REFERENCES

[1] L. L. Howell, *Compliant mechanisms,* in *21st Century Kinematics* (Springer, 2013) pp. 189–216.

[2] J. L. Herder and F. P. van den Berg, *Statically balanced compliant mechanisms (sbcm's): an example and prospects,* in *International Design Engineering Technical Conferences and Computers and Information in Engineering Conference,* Vol. 35203 (American Society of Mechanical Engineers, 2000) pp. 853–859.

[3] J. van Eijk and J. F. Dijksman, *Plate spring mechanism with constant negative stiffness,* Mechanism and Machine Theory **14**, 1 (1979).

[4] K. Hoetmer, G. Woo, C. Kim, and J. Herder, *Negative stiffness building blocks for stat-*

ically balanced compliant mechanisms: design and testing, Journal of Mechanisms and Robotics **2** (2010).

[5] C. Kim and D. Ebenstein, *Curve decomposition for large deflection analysis of fixed-guided beams with application to statically balanced compliant mechanisms,* Journal of Mechanisms and Robotics **4** (2012), 10.1115/1.4007488.

[6] P. R. Kuppens, M. A. Bessa, J. L. Herder, and J. B. Hopkins, *Compliant mechanisms that use static balancing to achieve dramatically different states of stiffness,* Journal of Mechanisms and Robotics **13** (2021), 10.1115/1.4049438.

[7] J. Zhang, A. D. Shaw, M. Amoozgar, M. I. Friswell, and B. K. S. Woods, *Bidirectional torsional negative stiffness mechanism for energy balancing systems,* Mechanism and Machine Theory **131**, 261 (2019).

[8] A. Lamers, J. A. G. Sánchez, and J. L. Herder, *Design of a statically balanced fully compliant grasper,* Mechanism and machine theory **92**, 230 (2015).

[9] D. F. Machekposhti, N. Tolou, and J. L. Herder, *A statically balanced fully compliant power transmission mechanism between parallel rotational axes,* Mechanism and Machine Theory **119**, 51 (2018).

[10] A. r. Stapel and J. L. Herder, *Feasibility study of a fully compliant statically balanced laparoscopic grasper,* in *International Design Engineering Technical Conferences and Computers and Information in Engineering Conference*, Vol. 46954 (2004) pp. 635–643.

[11] K. A. Tolman, E. G. Merriam, and L. L. Howell, *Compliant constant-force linear-motion mechanism,* Mechanism and Machine Theory **106**, 68 (2016).

[12] G. Radaelli, J. A. Gallego, and J. L. Herder, *An energy approach to static balancing of systems with torsion stiffness,* Journal of Mechanical Design **133** (2011).

[13] G. Radaelli and J. L. Herder, *A monolithic compliant large-range gravity balancer,* Mechanism and Machine Theory **102**, 55 (2016).

[14] D. J. de Lange, M. Langelaar, and J. L. Herder, *Towards the design of a statically balanced compliant laparoscopic grasper using topology optimization,* in *International Design Engineering Technical Conferences and Computers and Information in Engineering Conference*, Vol. 43260 (2008) pp. 293–305.

[15] J. Rommers, A. Aragon, V. van der Wijk, and J. L. Herder, *The stage method for simultaneous design of the stress and geometry of flexure mechanisms.* To be submitted to Precision engineering (2021).

[16] H. Soemers, *Design Principles for precision mechanisms* (T-Pointprint, 2011).

[17] A. Bos, *Position actuator for the ELT primary mirror,* Ph.D. thesis, Eindhoven University of Technology, The Netherlands (2017).

[18] L. Cacace, *An Optical Distance Sensor: Tilt robust [...]*, Ph.D. thesis, Eindhoven University of Technology, The Netherlands (2009).

[19] J. B. Hopkins, *A visualization approach for analyzing and synthesizing serial flexure elements,* Journal of Mechanisms and Robotics **7** (2015).

[20] J. Rommers, V. van der Wijk, and J. L. Herder, *A new type of spherical flexure joint based on tetrahedron elements,* Precision Engineering **71**, 130 (2021).

[21] S. Govindjee and P. A. Mihalic, *Computational methods for inverse finite elastostatics,* Computer Methods in Applied Mechanics and Engineering **136**, 47 (1996).

[22] A. E. Albanesi, M. A. Pucheta, and V. D. Fachinotti, *A new method to design compliant mechanisms based on the inverse beam finite element model,* Mechanism and Machine Theory **65**, 14 (2013).

[23] D. Wiersma, S. Boer, R. Aarts, and D. Brouwer, *Design and performance optimization of large stroke spatial flexures,* Journal of Computational and Nonlinear Dynamics **9** (2014), 10.1115/1.4025669.

[24] M. Naves, D. Brouwer, and R. Aarts, *Building block-based spatial topology synthesis method for large-stroke flexure hinges,* Journal of Mechanisms and Robotics **9** (2017), 10.1115/1.4036223.

[25] H. van der Deijl, D. de Klerk, J. L. Herder, and D. F. Machekposhti, *Dynamics of a compliant transmission mechanism between parallel rotational axes,* Mechanism and Machine Theory **139**, 251 (2019).

4

DESIGN OF A FOLDED LEAF SPRING WITH HIGH SUPPORT STIFFNESS AT LARGE DISPLACEMENTS USING THE INVERSE FINITE ELEMENT METHOD

In chapters 2 and 3 the functional geometry of the flexure mechanisms have been designed in the middle of the displacement range. In this chapter a folded leaf spring is designed in its actuated (displaced) state, which results in a high support stiffness in that position. The inverse finite-element method is used to enable this design step. A combination element is presented consisting of two folded leaf springs, which provide support stiffness at different regions in the displacement range. The results are validated using the commercially available FEM package Ansys.

This chapter has been published in the IFToMM World Congress on Mechanism and Machine Science [1]. Minor style and word changes have been made and section 4.2.1 has been added.

4.1. INTRODUCTION

Conventional mechanisms based on sliding or rolling contacts (for example ball bearings) typically have limited precision due to the inherent friction and play. *Compliant mechanisms* provide motion differently, by deflection of slender segments called *flexures* [2, 3]. In essence, these mechanisms can be regarded as highly deformable structures and therefore do not suffer from friction or play. This results in a highly repeatable behavior which is essential in high precision applications. However, the support stiffness of a flexure element tends to drop dramatically when the mechanism has undergone a displacement in the actuated direction [4–7]. This limits the useful range of motion and results in bulky designs.

Efforts to increase support stiffness in the actuated state include the addition of torsion reinforcement structures [7, 8], using pre-curved flexures [7, 9, 10], addition of elements in parallel [11, 12] and thickening the middle part of a flexure [3, 13, 14]. These methods all aim at designing the flexure mechanism in its relaxed state, in which it will be fabricated. However, the loss of support stiffness occurs in the actuated (loaded) state, on which the methods do not have direct control.

In this paper, we show that a flexure element can be designed in its actuated state, such that it will provide a high support stiffness in that position. To enable this, we will use the *Inverse Finite Element (IFE) Method*, originally proposed by Givindjee and Mihalic [15] and recently introduced to the compliant mechanisms community by Albanesi et al. [16]. Albanesi et al. have used the IFE method before to design compliant mechanisms. However, the authors use the method to control contact forces (for example in a compliant gripper). Instead, we use the IFE method to alter the support stiffness of the compliant mechanism itself. In other previous work [7, 9, 10], flexures have been pre-curved in order to obtain a high support stiffness in the actuated state. However, the authors use an optimization method, whereas we will use the IFE method which is computationally more efficient. Furthermore, this paper focuses on a different flexure element which avoids the high actuation forces mentioned in [9, 10].

First, the essence of the IFE method will be outlined. Second, the method used to increase support stiffness will be demonstrated by redesigning an existing flexure element. We will reflect on the work in the Results and Discussion section and the main constributions to literature will be summarized in the Conclusions section.

4.2. METHOD

In this section, first the reason for the support stiffness reduction of a blade flexure in its actuated position is investigated. Then, the essence of the IFE method from [15, 16] will be outlined. Subsequently, the folded leaf spring will be introduced. Using the proposed method, this element will be redesigned in order to obtain a high support stiffness in its actuated state. Lastly, an application example will be given.

4.2.1. SUPPORT STIFFNESS REDUCTION OF A BLADE FLEXURE IN THE ACTUATED STATE

Figure 4.1a shows a typical blade flexure in its actuated state. The left block is attached to the fixed world and the right block is the end effector which is actuated. Originally

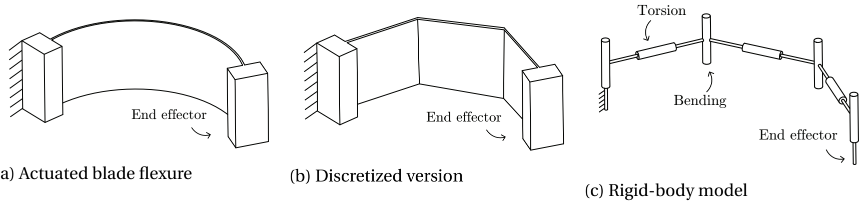

(a) Actuated blade flexure (b) Discretized version (c) Rigid-body model

Figure 4.1: Explanation of the support stiffness loss of a blade flexure in its actuated state due to curvature.

straight, the blade flexure has become curved after actuation, which results in a loss of support stiffness. Figure 4.1b shows a simplification of the blade flexure, where the curvature is discretized into two sharp folds, such that essentially three blade flexures in series result. Figure 4.1c shows a rigid-body model which is equivalent to the discretized version. Here, the deformation modes of the blade flexures with a low stiffness are represented by rigid bars connected by revolute joints, as in [11]. A blade flexure has a low stiffness in bending as well as torsion along its length axis, as indicated in the figure. The end effector is free in all six degrees of freedom, which can be proven as follows. A force in any direction on the end effector will have a moment arm around at least one of the revolute joints. The same holds for any moment. Because the revolute joints represent low-stiffness deformation modes, this means that the discretized flexure in Fig. 4.1b has a low support stiffness. The real curved flexure in Fig. 4.1a can be regarded as a large number of small blade flexures in series, which explains why it has a low support stiffness.

A folded leaf spring has a single sharp fold, which results in a single stiff translation at the place and in the direction of the fold line. A folded leaf spring therefore constrains one degree of freedom of its end effector, if it consists of two non-collinear straight blade flexures in series. A more detailed explanation can be found in [17].

4.2.2. THE INVERSE FINITE ELEMENT METHOD

The Inverse Finite Element (IFE) Method can be used to retrieve the relaxed (stress-free) shape of a structure when its loaded (stressed) shape and its external forces are specified [15, 16]. This includes analyses with large nonlinear deflections. Note that a compliant mechanism can be regarded as a structure undergoing large deflections.

First consider a regular (that is, forward) nonlinear Finite Element analysis in which the shape of a structure in its relaxed state is specified. The goal is to compute the unknown loaded shape as a result of specified external forces. Consider these forces to be independent of the shape (no follower-forces). The goal then is to solve

$$\vec{R}(\vec{U}) = \vec{0}, \tag{4.1}$$

which is the residual vector containing the imbalance of internal and external forces and moments in the loaded state. $\vec{U}$ is a vector containing the nodal displacements and rotations which need to be found. Note that for large deflections, $\vec{R}$ can have a nonlinear dependence on $\vec{U}$. We could also write

$$\vec{U} = \vec{X} - \vec{X}_0, \tag{4.2}$$

where $\vec{X}_0$ and $\vec{X}$ are the nodal coordinates in the relaxed and loaded states, respectively. Now we can write

$$\vec{R}(\vec{X}_0, \vec{X}). \tag{4.3}$$

In the forward FE method, $\vec{X}_0$ is specified and remains unchanged in the analysis. After applying boundary conditions, the residual equation is generally solved using some iterative method (for instance Newton-Rhapson) often relying on the gradient with respect to the unknowns $\vec{X}$:

$$\vec{K}_{fwd} = \frac{\partial \vec{R}(\vec{X}_0, \vec{X})}{\partial \vec{X}} \tag{4.4}$$

which is the stiffness matrix of the structure.

In the IFE method, the loaded shape $\vec{X}$ is specified as an input in $R(\vec{X}_0, \vec{X})$ which is then solved for the unknown relaxed shape $\vec{X}_0$ using the gradient with respect to these unknowns:

$$\vec{K}_{inv} = \frac{\partial \vec{R}(\vec{X}_0, \vec{X})}{\partial \vec{X}_0} \tag{4.5}$$

Note that mathematically, the IFE method is very similar to the regular forward FE method. Because of this similarity, their computational cost is also similar. Furthermore, note that the internal forces of the body are not needed as an input in the IFE method, since these are already determined once the loaded and unloaded shapes are known. Only the loaded shape, boundary conditions and external forces have to be known. The IFE routine can be modified such that instead of an external force, a displacement can be imposed. This modification is the same as in the case of the forward FE method (see for example [18]).

We have written an IFE code in Matlab using the 2D Euler-Bernoulli beam formulation. Large, nonlinear deflections are included using a co-rotational formulation as in [19]. The material is assumed to behave linearly elastic.

4.2.3. THE FOLDED LEAF SPRING

Figure 4.2 shows a linear guide commonly used in industry but less prevalent in literature [3, 20, 21]. Its central body is assumed rigid and is guided along the indicated Y direction by the six Folded Leaf Springs (FLS), which allow this motion by bending deformations. The blocks at the extremities of the leaf springs are attached to the fixed world. The design challenge typically is to provide a low stiffness along the actuated direction (Y in this case), while maintaining a high support stiffness in all other five spatial degrees of freedom of the central body.

Figure 4.3a shows one FLS element isolated from the mechanism. In its initial, relaxed state, the element provides a high support stiffness to the middle body in the indicated Z direction because it consists of two straight parts, as explained in section 4.2.1. Figure 4.3b shows a 2D representation of the same FLS in the XY-plane. The left side is attached to the fixed world. The right side is constrained in rotation and in the X-direction to simulate the connection to the central rigid body. The dashed line represents the relaxed state of the FLS, while the colored solid line shows the FLS in actuated (loaded) state. The colors indicate the stresses. In this loaded state the FLS inevitably becomes curved and thereby loses a significant part of its support stiffness in Z direction [4–7]. This issue will be addressed in the next section.

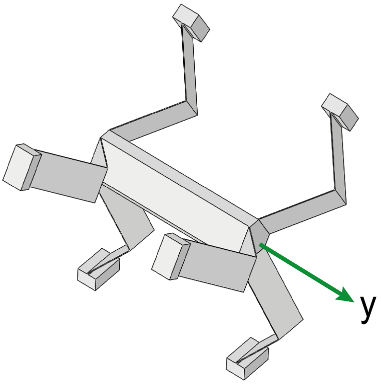

Figure 4.2: A compliant linear guide commonly used in industry, existing of six Folded Leaf Springs (FLS) [3, 20, 21]. These slender elements allow for movement in the Y direction by elastic bending deformations.

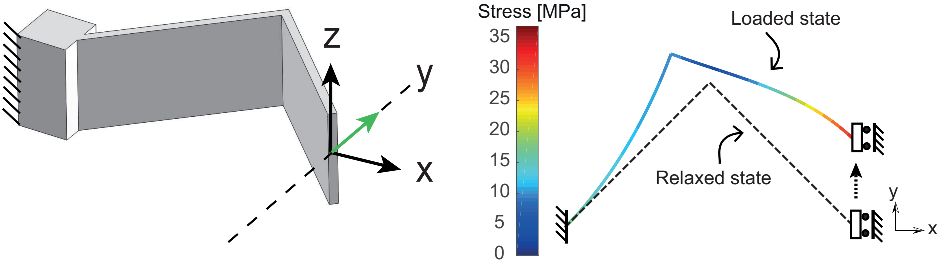
z
y
x
Stress [MPa]
35
30
25
20
15
10
5
0
Loaded state
Relaxed state
y
x

(a) Isolated FLS.

(b) FE simulation of the FLS

Figure 4.3: Figure a) shows a single FLS isolated from the linear guide from Fig. 4.2. Figure b) shows the curvature occurring in its loaded state, causing the dramatic decrease in support stiffness in Z direction.

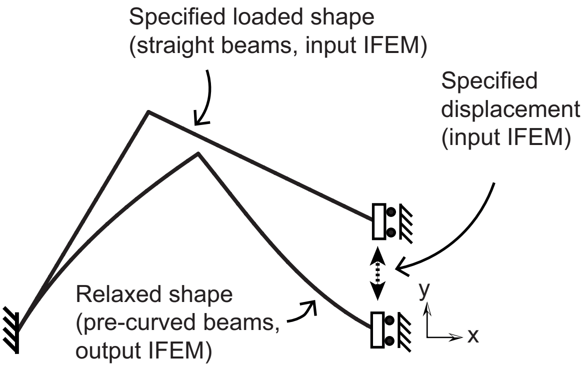

Figure 4.4: This FLS is initially curved such that it will attain a straight shape after actuation in Y direction, providing a high support stiffness in this position. The pre-curved relaxed shape can be computed efficiently using the IFE method.

4.2.4. REDESIGN OF THE FOLDED LEAF SPRING USING THE IFE METHOD

In this section, we will redesign the FLS element such that it provides a high support stiffness in its actuated (loaded) state, instead of in its relaxed home position. The main idea is to design the FLS such that it has an initial curvature in its relaxed state. This curvature should be such that the FLS becomes straight in its loaded state, thereby increasing its support stiffness. Figure 4.4 shows this FLS element. Using the IFE method, the FLS can be designed in its actuated state at some specified displacement. The IFE method will output the relaxed, pre-curved shape of the FLS. Note that only the loaded shape and displacement have to be specified to fully determine the relaxed shape shown in Fig. 4.4. The displacement is chosen as 21.4 mm. The straight beams both have a length of 111.8 mm. The choice of these numbers will be explained in the next section.

4.2.5. DESIGN AND VALIDATION OF THE COMBINATION ELEMENT

The pre-curved FLS designed in the previous section will provide a high support stiffness around its actuated position, but a low support stiffness around its home position. To realize a high support stiffness around both positions, we can add a pre-curved FLS to a regular FLS to form a *combination element* as in Fig. 4.5. Figure 4.5a shows this combination element in the relaxed state, where the mechanism is in its relaxed home position. Here, the regular, straight flexure provides support stiffness in the Z direction. In the actuated state shown in Fig. 4.5b, the pre-curved FLS has become straight and now provides support stiffness in its turn.

The combination element is designed as follows. First some properties and dimensions of the regular FLS are chosen as summarized in Table 4.1. Using the commercially available FE package Ansys™, the support stiffness of this FLS is computed while it is actuated along its motion range Y as in Fig. 4.3b. Beam188 elements are used, with the option for nonlinear geometry activated. Note that this data cannot be computed using the code written in Matlab, because that code only considers beams in 2D. Using

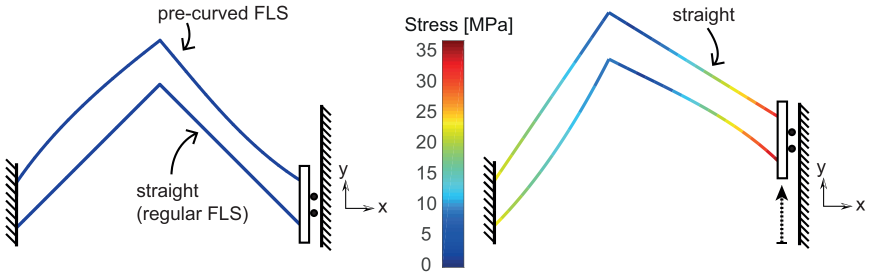

(a) Home position (relaxed)

(b) Actuated state (loaded)

Figure 4.5: Combination element in which a pre-curved FLS is combined with a regular FLS. In a), both flexures are relaxed and the straight flexure provides support stiffness in the Z direction. In its actuated state shown in b), the pre-curved flexure has become straight and provides support stiffness in its turn.

Table 4.1: Properties of the folded leaf spring as shown in Fig. 4.3.

Variable	Value
Size X direction	100 mm
Size Y direction	50 mm
Size Z direction	10 mm
Flexure thickness	1 mm
E-modulus (Polyactic Acid, PLA)	4 GPa

the obtained support stiffness data, we can now decide at which point in the displacement range the pre-curved FLS should become straight in order to compensate for the stiffness loss of the initially straight FLS. The shape of the relaxed pre-curved FLS will be computed using the IFE code written in Matlab. Finally we will validate the support stiffness of the combination element over its full range using Ansys. For a fair comparison with the state-of-the-art, the combination element will be compared to an element consisting of two regular, initially straight FLS elements.

4.3. RESULTS AND DISCUSSION

Figure 4.6 shows the support stiffness of the combination element shown in Fig. 4.5 along its displacement range (red solid line). This stiffness is compared to that of an element with two regular, initially straight FLS elements shown by the black solid line. As anticipated, the combination element shows a lower support stiffness for small displacements because only one of the FLS elements provides support stiffness at this point. However, at larger displacements, the combination element outperforms the double regular FLS design because the pre-curved flexure has become straight. Furthermore, the

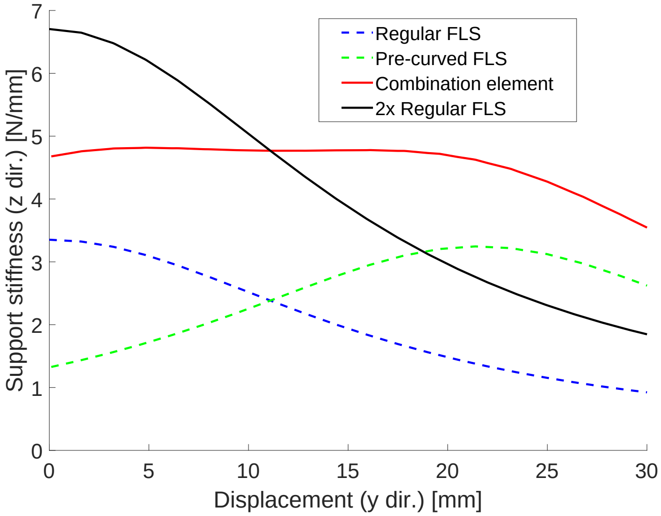

Figure 4.6: Support stiffness of the combination element shown in Fig. 4.5 (red), compared to the case with two regular, straight flexures (black), showing an extension of the range with high support stiffness. The dashed lines in green and blue show the contributions of the two flexures forming the combination element.

support stiffness of the combination element is more constant along the displacement range. This results in a more straight trajectory of the mechanism under influence of gravity forces.

More pre-curved FLS elements could be added to cover a larger region of high support stiffness. These can be designed such that they cover the region in the negative Y direction, using the same proposed method. Adding more elements will increase the stiffness in the actuation direction y, which is generally not desired. However, this could be dealt with by *static balancing techniques* [22].

The green dashed line in Fig. 4.6 shows the support stiffness of the pre-curved redesigned FLS. The stiffness peak is shifted to the actuated state, but its shape is similar to the stiffness peak of the regular FLS shown in dashed blue. This result validates the use of the IFE code in Matlab to shift support stiffness from the home position to the actuated state. The shifting distance is specified as 21.4 mm, in order to provide an optimal stiffness overlap resulting in a constant support stiffness of the combination element.

Computing the shape of the pre-curved FLS shown in Fig. 4.4 was done efficiently using the IFE code written in Matlab. Such a computation takes around half a second using the code on a regular laptop. Using IFE routines to shift support stiffness will be more advantageous when considering flexure mechanisms exhibiting complex spatial behavior. When shell elements need to be used instead of beam elements, the analysis can become computationally too expensive for the use of optimization methods. The IFE method could be used in these cases to provide a solution.

The validation of the combination element was done only theoretically. Flexures are often fabricated out of high-strength steels using Wire-Electrical Discharge Machining.

This technique readily allows for fabrication of initially curved flexures. However, it is anticipated that considerable attention should be paid to tolerances in thickness of the flexures, since the bending stiffness has a cubic relation to this property. Furthermore, the combination element in Fig. 4.5 is partly *overconstrained* (see [3] for a detailed explanation). Overconstraints could result in unpredictable behavior under the influence of temperature changes or manufacturing errors. However, this overconstraint is only present in the region of the displacement range where the two FLS elements provide comparable support stiffness. In the other configurations, only one of the FLS elements effectively provides support stiffness and so the system can be considered to not be overconstrained.

4.4. CONCLUSION

In this paper, we showed that the Inverse Finite Element (IFE) Method can be used to efficiently design flexure elements such that they have a high support stiffness in their actuated state. This is beneficial because most existing flexure elements only provide support stiffness at their relaxed home position. The method is efficient because it does not need design iterations, as is the case in optimization methods.

As an example, a Folded Leaf Spring (FLS) element with a high support stiffness in its actuated state was designed using an IFE code written in Matlab. The resulting *pre-curved* design was analyzed using the commercial Finite Element software package Ansys™. The results show that the element indeed has a large support stiffness in its actuated state instead of in its home position.

We showed an example implementation of this pre-curved FLS, in which it is combined with a regular FLS element such that it will provide a high support stiffness in both its home position and its actuated state. Using Ansys, this combination element was compared to a benchmark design consisting of two regular FLS elements. As expected, the benchmark design has a higher support stiffness at the home position, but the combination element outperforms it at the actuated positions and shows a more constant support stiffness along its range of motion.

The proposed method could aid in improving support stiffness of flexure mechanisms in their actuated state, resulting in more compact designs with larger range of motion.

4.5. ACKNOWLEDGMENT

This work is part of the research programme Möbius with project number 14665, which is (partly) financed by the Netherlands Organisation for Scientific Research (NWO).

REFERENCES

[1] J. Rommers and J. Herder, *Design of a folded leaf spring with high support stiffness at large displacements using the inverse finite element method,* in *IFToMM World Congress on Mechanism and Machine Science* (Springer, 2019) pp. 2109–2118.

[2] L. L. Howell, S. P. Magleby, and B. M. Olsen, *Handbook of compliant mechanisms* (John Wiley & Sons, 2013).

[3] H. Soemers, *Design Principles for precision mechanisms* (T-Pointprint, 2011).

[4] S. Awtar, A. H. Slocum, and E. Sevincer, *Characteristics of beam-based flexure modules,* Journal of Mechanical Design **129**, 625 (2007).

[5] D. M. Brouwer, J. P. Meijaard, and J. B. Jonker, *Large deflection stiffness analysis of parallel prismatic leaf-spring flexures,* Precision Engineering **37**, 505 (2013).

[6] M. Nijenhuis, J. P. Meijaard, D. Mariappan, J. L. Herder, D. M. Brouwer, and S. Awtar, *An analytical formulation for the lateral support stiffness of a spatial flexure strip,* Journal of Mechanical Design **139** (2017), 10.1115/1.4035861.

[7] D. Wiersma, S. Boer, R. G. Aarts, and D. M. Brouwer, *Design and performance optimization of large stroke spatial flexures,* Journal of computational and nonlinear dynamics **9**, 011016 (2014).

[8] M. Naves, D. Brouwer, and R. Aarts, *Building block-based spatial topology synthesis method for large-stroke flexure hinges,* Journal of Mechanisms and Robotics **9** (2017), 10.1115/1.4036223.

[9] D. M. Brouwer, J. P. Meijaard, and J. B. Jonker, *Elastic element showing low stiffness loss at large deflection,* in *Proceedings of the 24th Annual Meeting of the American Society of Precision Engineering, Monterey, CA* (2009) pp. 30–33.

[10] S. E. Boer, R. Aarts, D. M. Brouwer, and J. B. Jonker, *Multibody modelling and optimization of a curved hinge flexure,* in *The 1st joint international conference on multibody system dynamics, Lappeenranta* (2010) pp. 1–10.

[11] B. P. Trease, Y.-M. Moon, and S. Kota, *Design of large-displacement compliant joints,* Journal of mechanical design **127**, 788 (2005).

[12] G. Hao and H. Li, *Extended static modeling and analysis of compliant compound parallelogram mechanisms considering the initial internal axial force,* Journal of mechanisms and robotics **8**, 041008 (2016).

[13] H. Malaeke and H. Moeenfard, *A novel flexure beam module with low stiffness loss in compliant mechanisms,* Precision Engineering **48**, 216 (2017).

[14] M. Bakhtiari-Shahri and H. Moeenfard, *Topology optimization of fundamental compliant mechanisms using a novel asymmetric beam flexure,* International Journal of Mechanical Sciences **135**, 383 (2018).

[15] S. Govindjee and P. A. Mihalic, *Computational methods for inverse finite elastostatics,* Computer Methods in Applied Mechanics and Engineering **136**, 47 (1996).

[16] A. E. Albanesi, M. A. Pucheta, and V. D. Fachinotti, *A new method to design compliant mechanisms based on the inverse beam finite element model,* Mechanism and Machine Theory **65**, 14 (2013).

[17] J. Rommers, M. Naves, D. Brouwer, and J. Herder, *A large range spatial linear guide with torsion reinforcement structures,* in *International Design Engineering Technical Conferences and Computers and Information in Engineering Conference*, Vol. 51807 (American Society of Mechanical Engineers, 2018).

[18] A. F. Bower, *Applied mechanics of solids* (CRC press, 2009).

[19] R. D. Cook, D. S. Malkus, M. E. Plesha, and R. J. Witt, *Concepts and Applications of Finite Element Analysis: 4th Edition* (2002).

[20] A. Bos, *Position actuator for the ELT primary mirror,* Ph.D. thesis, Eindhoven University of Technology, The Netherlands (2017).

[21] L. Cacace, *An Optical Distance Sensor: Tilt robust [...]*, Ph.D. thesis, Eindhoven University of Technology, The Netherlands (2009).

[22] J. L. Herder, *Design of spring force compensation systems,* Mechanism and machine theory **33**, 151 (1998).

5

A FLEXURE-BASED LINEAR GUIDE WITH TORSION REINFORCEMENT STRUCTURES

In this chapter, a flexure-based linear guide with a motion range comparable to its footprint is presented. The design consists of two folded leaf springs on which torsion reinforcement structures are added. Due to these structures, only two folded leaf springs are needed instead of a minimum of five as in pre-existing designs. The new design is compared to such a pre-existing design, after optimizing both on a support stiffness metric. The new design scores over twice as high on the support stiffness metric, while occupying a smaller (-33%) and a less obstructive build volume. Stress, build volume and manufacturing limitations are taken into account. Additionally, a variation on the new design using three torsion reinforced folded leaf springs is presented and optimized. This design occupies a build volume similar to the pre-existing design, but scores four times higher on the support stiffness metric. A prototype of the new design is built and its parasitic eigenfrequencies are measured, validating the theoretical models (Normalized Mean Absolute Error of 4.3%).

This chapter has been published in the Journal of Mechanisms and Robotics [1]. An earlier version has been published in the proceedings of the ASME IDETC conference in 2018 [2].

5.1. INTRODUCTION

Unlike rigid-body mechanisms which gain their mobility through rolling or sliding contacts, flexure (or compliant) mechanisms use the elastic deformation of slender segments to enable motion. The inherent absence of friction and play makes these mechanisms particularly suitable for precision positioning applications due to their excellent repeatability [3–9]. This work focuses on flexure based linear guides, which allow a single translational motion of the end effector along a straight line.

The majority of the linear guide designs in literature are planar, meaning that they are fabricated monolithically from a single plate. The simplest design is composed of two leaf springs and a rigid body in a parallelogram configuration [10]. This design suffers from parasitic motions, which can be mitigated by nesting two parallelograms [11]. However, this results in an unconstrained intermediate body which decreases both the static and dynamic performance [4, 12, 13]. Efforts to solve this problem include a design in which the intermediate body is coupled to the main stage by means of a lever system [10, 14], one where the intermediate bodies of two double parallelogram building blocks are connected [15], and a constraining mechanism cleverly nested inside the parallelogram [12]. Not all designs in literature are based on the parallelogram. Examples are a design based on the Robert's mechanism [16] and on the Watt's mechanism [14, 17].

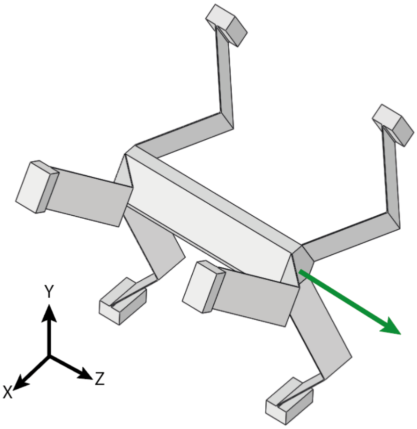

Figure 5.1: The pre-existing 6 Folded Leaf Spring (6FLS) linear guide which needs at least five FLS elements to constrain the five motions, leading to a large and obstructive build volume.

Some spatial linear guides are described in literature. These designs generally have larger motion ranges compared to the planar designs because self-collisions can be avoided. The two main designs are based on diaphragm flexures [18–20] and on folded leaf springs [10, 20–23]. The diaphragm design has a low-cost potential but suffers from a trade-off between parasitic rotation and range of motion [19]. The linear guide consisting of six folded leaf springs (6FLS) is shown in Fig. 5.1. The 6FLS design is highly suitable for large ranges, but its protruding elements result in an obstructive build volume. This is because at least five folded leaf springs are necessary to constrain five degrees of freedom of its end effector, as will be explained in more detail in section 5.2.1. The design is mostly known in industry, and has not been described extensively in literature [10, 20–23].

In this work, we present a new linear guide with a motion range comparable to its footprint. The design consists of two folded leaf springs on which torsion reinforcement structures are added: Torsion Reinforced Folded Leaf Springs (TR-FLS). Due to the reinforcements, only two elements are needed rather than five or six as in pre-existing designs. This results in a smaller and less obstructive build volume than the pre-existing 6FLS design shown in Fig. 5.1. We call the new design the 2-TR-FLS. We will optimize and compare the 2-TR-FLS and the 6FLS design, focusing on support stiffness and build volume. Limits on stress and manufacturing techniques are taken into account. Additionally, we present a variation on the new design called the 3-TR-FLS, which has a build volume comparable to the 6FLS design. This design will be optimized and compared in the same manner.

In section two, the three linear guides are presented. Section three explains the optimization and comparison procedure. Section four contains an experimental validation of the theoretical models, using a prototype based on the optimized 2-TR-FLS design. We reflect on the results in the Discussion section and summarize the contributions to literature in the Conclusions section.

5.2. LINEAR GUIDE DESIGNS

In this section, first the working principle of the pre-existing 6FLS design will be described. Then, the Torsion Reinforced Folded Leaf Spring (TR-FLS) will be explained. Subsequently, the two new linear guides composed of this element are presented.

5.2.1. THE 6 FOLDED LEAF SPRING (6FLS) LINEAR GUIDE

Figure 5.2 shows one of the Folded Leaf Springs (FLS) of the 6FLS guide illustrated in Fig. 5.1. The FLS is fixed at the left side and the block at the right side represents its end effector e. The lower part of Fig. 5.2 shows a rigid-body model, in which the deformation modes with low stiffness are visualized using revolute joints [11]. Bending of the leaf springs is represented by the vertical revolute joints, and torsional deformation is represented by a revolute joint coincident with the length axis of the flexures. The end effector e is extended in order to reach the point underneath the fold line, at which the arrow engages. At this point, motion in z-direction is not possible in the kinematic model, meaning that it is constrained in the real FLS. This is only true for a point on the indicated dashed line running through the fold line [10, 24]. Rotations of the end effector are free because the revolute joints span the full space. This means that the FLS only constrains one translation. A FLS could be replaced by a wire flexure (essentially a slender rod) placed at the fold line without changing the kinematics of the mechanism [10, 24, 25]. The advantage of a FLS over a wire flexure is that it does not suffer from a shortening effect, which makes it specifically suitable for large ranges of motion.

Because a single FLS constrains only one degree-of-freedom of its end effector, at

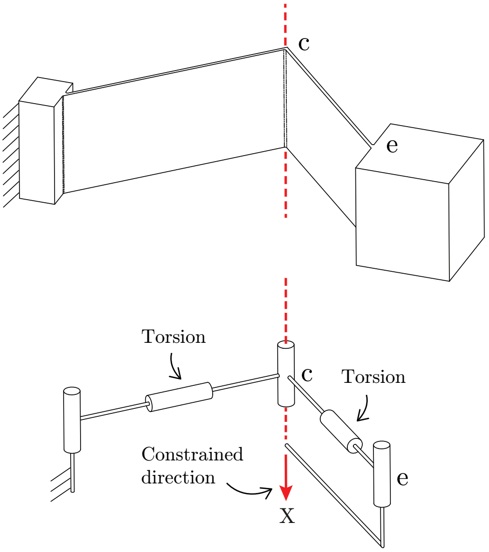

Figure 5.2: The Folded Leaf Spring (FLS) and its rigid-body model. The arrow shows its single translational constraint.

least five FLS elements are needed to create a linear guide. A sixth FLS is usually added to improve symmetry.

In pseudo-rigid body models [3] a blade flexure is often represented without the revolute joint which represents torsion. This representation is valid for planar mechanisms with planar loads, but if spatial loads are present the torsional compliance needs to be taken into account [25, 26]. To illustrate this, consider a typical blade flexure with length $L = 100$ mm, height (in x-direction in Fig. 5.2) $h = 20$ mm, thickness $t = 0.2$ mm, $E = 210$ GPa and $G = 80$ GPa. The torsional stiffness is [27]:

$$K_T = \frac{GJ}{L}, \tag{5.1}$$

where $J = \frac{1}{3}ht^3$ for wide cross sections [27]. The bending stiffness (rotation around the x-direction in Fig. 5.2) is [28]:

$$K_{rx} = \frac{EI_{rx}}{L} \tag{5.2}$$

where the area moment of inertia around the x-axis is $I_{rx} = \frac{1}{12}ht^3$. The in-plane bending stiffness of the blade flexure is:

$$K_{ipb} = \frac{EI_{ipb}}{L} \tag{5.3}$$

where $I_{ipb} = \frac{1}{12}th^3$. For the chosen dimensions this results the stiffness values $K_T =$ 4.3e−2 Nm/rad, $K_{rx} =$ 2.8e−2 Nm/rad, and $K_{ipb} =$ 2.8e2 Nm/rad. The torsion stiffness K_T has the same order of magnitude as stiffness K_{rx}, which are both indeed considered as free in the kinematic model. The in-plane bending stiffness K_{ipb} is four orders of magnitude higher and is considered as constrained in the kinematic model. The low torsional stiffness of the blade flexures is the reason that the FLS only provides a translation stiffness at point c in the X-direction. For example, the stiffness in x-direction at the end effector e due to the torsional stiffness of the left blade flexure is (assuming for simplicity that the two blades are at an angle of 90 degrees):

$$K_{xe,T} = \frac{K_T}{l^2}. \tag{5.4}$$

Note that the total stiffness at point e is actually lower because not all deformations are taken into account. The stiffness at c in the x-direction is not dependent on the torsional stiffness, but on the lateral stiffness of the two blade flexures, as [10]:

$$K_{xc} = \left[\frac{2L^3}{3EI_{ipb}} + \frac{12L}{5Gth}\right]^{-1} \tag{5.5}$$

For the chosen blade flexure dimensions, stiffness $K_{xc} = 4.1\text{e}4$ N/m and $K_{xe,T} = 4.3$ N/m. The stiffness at point c is at least four orders of magnitude higher than the stiffness at point e, which validates that the FLS provides a constraint at c and not at e. For blade flexures with a smaller length to height ratio, additional stiffness due to constrained warping has to be taken into account when computing the torsion stiffness in equation 5.1 [29]. However, this effect is small compared to the difference in free and constrained stiffness terms [29].

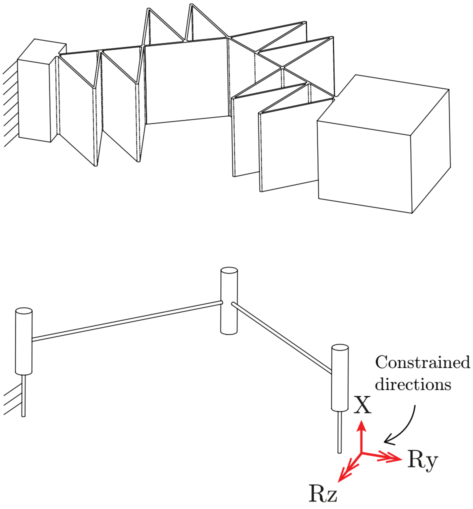

Figure 5.3: The TR-FLS element and its rigid-body model, showing the three constrained directions.

5.2.2. THE TORSION REINFORCED FOLDED LEAF SPRING (TR-FLS)

Figure 5.3 shows the TR-FLS element, consisting of a folded leaf spring with torsion reinforcement structures. These structures are proposed in earlier work [29, 30], in which they are used to create a flexure joint with high stiffness in its supporting directions, at large rotations. Instead, we will use the torsion reinforcement structures to add two rotational constraints to the FLS. The lower part of Fig. 5.3 shows this, using a rigid-body model of the TR-FLS. The two revolute joints representing torsion in Fig. 5.2 are now removed, resulting in a planar linkage. The TR-FLS only allows movements in the xy-plane because translation in Z and rotation around X and Y are constrained. Furthermore, the TR-FLS constrains motion in z-direction at any place, contrarily to the FLS in which the motion is only constrained for points on the line running through the fold line.

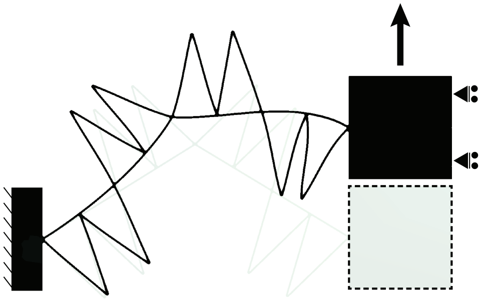

Figure 5.4: Visualization of the deformations in the TR-FLS (scale 1:1). Note that the triangular shapes consist of blade flexures, resulting in distributed strains. The flexure thickness in the figure is equal for all parts.

It is important to note that the torsion reinforcement structures in the TR-FLS are not rigid, but behave as leaf springs. This results in a smooth strain distribution, as visualized in Fig. 5.4. If the torsion reinforcement structures would be rigid, all strains would be localized between the triangular shapes, which would lead to high peaks in the distribution.

5.2.3. THE 2-TR-FLS LINEAR GUIDE

Figure 5.5 shows the 2-TR-FLS linear guide. As shown in Fig. 5.3, a single TR-FLS only allows in-plane motions. The intersection of the motion planes of the two TR-FLS elements forms a line, over which the end effector of the linear guide moves. This is similar to the well-known rigid link Sarrus mechanism. The 2-TR-FLS has a less obstructive build volume than the 6FLS guide shown in Fig. 5.1. The end effector is accessible through a 270 degrees angle. Note that the two TR-FLS elements do not necessarily have to be at a 90 degrees angle, as long as the two motion planes are not parallel. Similar to the Sarrus (and the 6FLS) mechanism, the rotation around the Z axis of the 2-TR-FLS is *overconstrained*. This will be discussed in section 5.5.

5.2.4. 3-TR-FLS LINEAR GUIDE

Figure 5.6 shows the 3-TR-FLS linear guide, constructed by adding a third TR-FLS element to the 2-TR-FLS design. The motion plane of this third TR-FLS element again in-

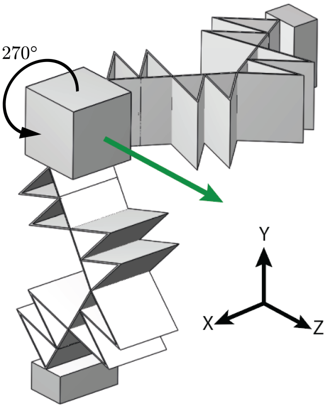

Figure 5.5: 2-TR-FLS linear guide, showing a smaller and less obstructive build volume than the 6FLS design. The end effector can be reached through a 270 degrees angle.

tersects at the motion axis. This design is mainly considered for comparative purposes, because the 6FLS can be constructed such that it has the same build volume as the 3-TR-FLS design. This will be explained in the next section.

5.3. OPTIMIZATION AND COMPARISON

The 2-TR-FLS, 3-TR-FLS and 6FLS design will be optimized and compared on a support stiffness performance metric, while subjected to the same optimization constraints such as build volume and maximum stress. First, this performance metric will be defined more precisely. Then, the optimization variables, constraints and algorithm are described. Finally, the results are presented.

5.3.1. PERFORMANCE METRIC

All three linear guides are optimized on support stiffness, which is defined as the lowest translational stiffness in the XY-plane in Fig. 5.5. The lowest support stiffness value throughout the full range of motion is chosen as the performance metric. A higher value is considered better. This performance metric is chosen because the lowest parasitic eigenfrequency of the linear guide is anticipated to correspond to a translational mode shape, thus determining the dynamic behavior of the mechanism. A translational mode shape is expected because the end effector is small compared to the flexures, and therefore has a relatively low rotational inertia compared to its mass.

5.3.2. OPTIMIZATION VARIABLES AND CONSTRAINTS

Figure 5.7 shows the design variables which are varied in the optimization routine. P depicts the point in which the support stiffness is determined and at which the mechanism

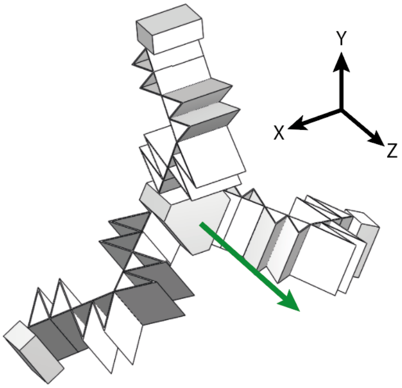

Figure 5.6: 3-TR-FLS linear guide for comparison purposes.

is actuated. The y-coordinate of this point has the fixed value W_{end} and the variable L_{end} is the distance between this point and the attachment of the flexure. The variable θ is introduced to allow the design to rotate with respect to its motion path. Variables t_t and t_{ff} depict the thickness of the flexures of the torsion reinforcement and the folded leaf spring itself, respectively. The height of the flexures in the third dimension is not drawn and is named H. L_{ff}, W_{ff} and W_t are the distance between the two attachment points of the flexure, the width of the main flexure and the width of the torsion reinforcement structures, respectively. Note that the 6FLS design only contains part of the variables depicted in Fig. 5.7. A spacing of 75 mm between the leaf springs of the 6FLS design is chosen. This way, the footprint measure as depicted in Fig. 5.8 will approximate those of the other mechanisms, allowing for a fair comparison. Tables 5.1 and 5.2 show the constraints and the fixed values used in the optimizations, respectively. A maximum of 50 mm for the height H of the flexures is chosen, because the cross-section of the end effector measures 50 by 50 mm.

Constraint	Value
Maximum stress $[Mpa]$	600
Minimum flexure thickness t_{ff} and t_{tr} $[mm]$	0.2
Maximum flexure height H $[mm]$	50
Maximum Y dimension L_Y $[mm]$	150
Maximum driving force $[N]$	10
No collisions	-

Table 5.1: Optimization constraints, depicted in Fig. 5.7.

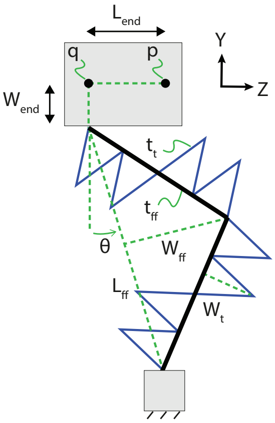

Figure 5.7: Design variables of the TR-FLS. P depicts the point in which the stiffnesses are determined. The height of the flexures in the third dimension is not drawn and is named H. Variables t_t and t_{ff} depict the thickness of the torsion reinforcement structure and the folded leaf spring itself, respectively.

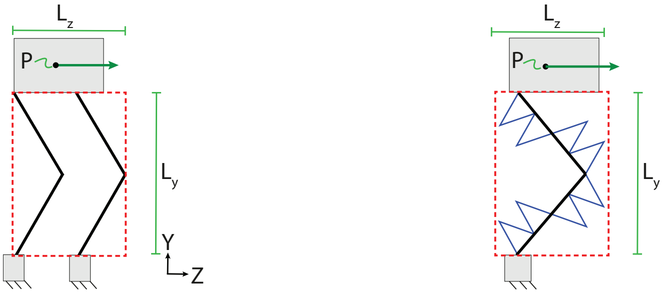

(a) 6FLS design

(b) TR-FLS designs

Figure 5.8: Footprint measures for (a) the 6FLS design and (b) the 2-TR-FLS and 3-TR-FLS linear guides. The 2-TR-FLS design uses only two of these blocks, whereas the other two designs need three blocks.

5.3.3. OPTIMIZATION ALGORITHM

A derivative-free function comparison search method based on the Nelder-Mead optimization algorithm [31] is used to find the set of design variables for each of the three linear guide designs which scores highest on the performance metric defined in section 5.3.1. To include all constraints from Table 5.1, the algorithm is adapted in order to ensure feasible solutions within the solution space as in earlier work of two of the authors [30]. The performance metric is computed using the flexible multibody software SPACAR [32]. SPACAR uses nonlinear 3D finite beam elements which include geometric non-linearities. Due to the specific choice of discrete deformation modes, only a limited number of elements is required to produce both fast and accurate results. Computational cost is further reduced by taking into account symmetry conditions of the full mechanisms.

Fixed parameter	Value
Motion range in z-direction $[mm]$	-50 to +50
End effector W_{end} $[mm]$	25
E modulus $[GPa]$	210
Poisson ratio $[-]$	0.3125

Table 5.2: Fixed parameters in the optimizations, depicted in Fig. 5.7.

5.3.4. OPTIMIZATION RESULTS

Figure 5.9 shows the support stiffness of the three optimized linear guides along their motion range. Support stiffness was defined as the lowest translational stiffness in the XY plane. The minimum support stiffness in the motion range is shown in Table 5.3. Note that this was the performance metric in the optimization.

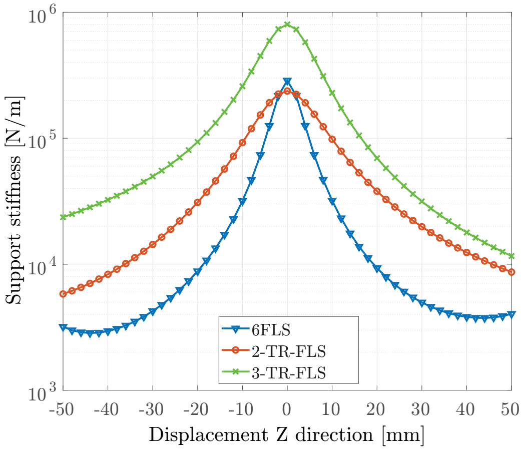

Figure 5.9: Support stiffness versus displacement of the three optimized designs, defined as the lowest translational stiffness in the XY-plane.

Figures 5.10 and 5.11 show the stiffness of the optimized linear guides in other directions. Note that the designs are not optimized on these measures. Figure 5.10 shows the rotational support stiffness, defined as the lowest rotational stiffness in the XY-plane. Figure 5.11 shows the torsional stiffness around the motion axis Z.

Table 5.4 shows the design variables resulting from the optimizations. In all optimizations, the thickness of the flexure elements results in the lower bound of 0.2 mm. Furthermore, all designs result in the maximum driving force of 10 N and all reach the maximum stress of 600 MPa. The height H of the flexures (approximately) reached the upper bounds of 50 mm for the 2-TR-FLS and 3-TR-FLS designs, whereas the 6FLS design has

Design	Minimum support stiffness
6FLS (pre-existing)	2840 $[N/m]$
2-TR-FLS	5811 $[N/m]$
3-TR-FLS	11620 $[N/m]$

Table 5.3: Minimum support stiffness throughout the range of motion (100 mm) for each optimized design.

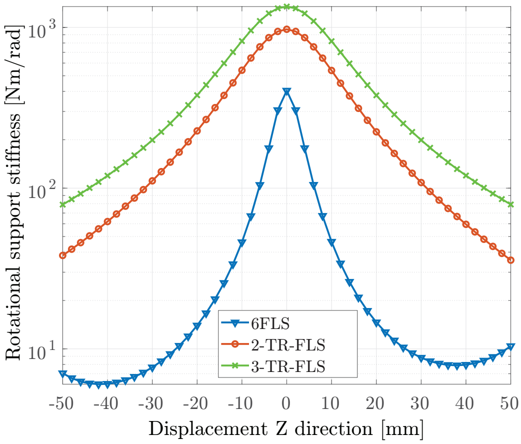

Figure 5.10: Rotational support stiffness versus displacement of the three optimized designs, defined as the lowest rotational stiffness vector in the XY-plane.

a H value of 22 mm. Dimensions L_Z and L_Y are measures for the footprint of the mechanisms, as depicted in Fig. 5.8.

5.4. EXPERIMENTAL VALIDATION

In order to validate the theoretical model, a prototype based on the optimized 2-TR-FLS design is tested experimentally. In this section we describe the design of the prototype and the measurement setup, and present the results.

5.4.1. PROTOTYPE

The prototype is built from Polyamide 12 (Nylon) using a Selective Laser Sintering (SLS) process. Using Nylon instead of steel (as in the optimizations) has the advantage that the stiffness of the steel support frame can be neglected and therefore does not need to be modeled. Material properties of printed Nylon using the SLS process are experimentally tested by [33]. Taking the printing direction into account, the authors report a Young's modulus of 1.62 GPa and a Poisson ratio of 0.387. Figure 5.12 shows the design of the prototype. The two TR-FLS elements forming the 2-TR-FLS linear guide are printed separately and then joined using four bolts. The printing direction for each TR-FLS is in the direction perpendicular to the drawing plane of Fig. 5.7. Both TR-FLS elements

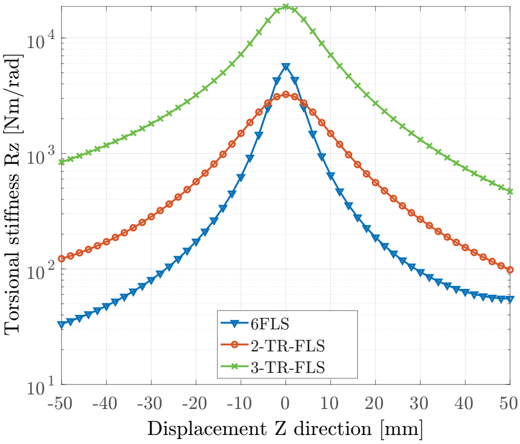

Figure 5.11: Torsional stiffness around the motion axis versus displacement, of the three optimized designs.

of the prototype in Fig. 5.12 have staircase-shaped end effectors which fit on to each other. Some dimensions of the optimized design are changed in the prototype. Figure 5.12 shows that the end effector of the horizontal TR-FLS is elongated by 12.5 mm. This is to avoid collisions of the triangular segments with the other TR-FLS element. This has as result that W_{end} of the top TR-FLS is changed from 25 mm to 37.5 mm, and that the center of mass of the end effector is shifted. The new center of mass is located 6.25 mm in negative x-direction from point q, as indicated in Fig. 5.12. Furthermore, the triangular segments closest to the attachment points of the TR-FLS elements in Fig. 5.12 are at the left side of the main leaf spring, whereas these were positioned at the right side in the optimization result. Lastly, the thickness of the flexures t_t and t_{ff} (see Fig. 5.7) is set to 1 mm because of the changed material properties and limitations of the SLS manufacturing process. The thickness of the leaf springs and torsion reinforcements are measured at 14 positions using a micrometer with a force restrictor. The average value is used in the SPACAR model. The dimensions L_{ff} (see Fig. 5.7) and height H of the additively manufactured prototype is checked using a caliper. Sharp corners are rounded off with 1 mm radius fillets to avoid stress concentrations.

5.4.2. MEASUREMENT SETUP

The support stiffness of the linear guide is validated indirectly by measuring the eigenfrequencies of the prototype. This way, inaccuracies due to stress relaxation are mitigated. The lowest eigenfrequency of the unactuated stage should have a mode shape in which the end effector moves in its intended motion direction. This frequency is ideally low, indicating a low motion stiffness. The mode shapes in the undesired directions are considered parasitic and ideally occur at high frequencies, indicating a high support stiffness.

The mass and inertia of the end effector are calculated using the CAD software Solid-

Dimension	6FLS	2-TR-FLS	3-TR-FLS
L_{ff} [mm]	150	149	150
W_{ff} [mm]	36	46	75
t_{ff} [mm]	0.2	0.2	0.2
W_t [mm]	-	41	28
t_t [mm]	-	0.2	0.2
H [mm]	22	50	49
α [rad]	0	0	0
L_{end} [mm]	37.5	39.4	63
L_Z [mm]	111	104	97
L_Y [mm]	150	150	150

Table 5.4: Optimized design variables with corresponding footprints (depicted in Figs. 5.7 and 5.8) for the three designs in Figs. 5.1, 5.5 and 5.6. All designs use the maximum driving force of 10 N and maximum stress of 600 MPa.

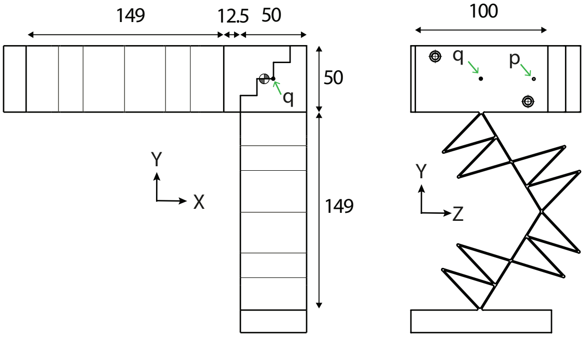

Figure 5.12: Prototype of the 2-TR-FLS, dimensions in mm. Point p and q correspond to Fig. 5.7.

works. These values are used in the SPACAR model to perform the dynamic analysis. To check the CAD software and the manufacturing process, two tests are carried out. Firstly, the density value used in the CAD software is checked. The mass of a single TR-FLS arm is calculated using the CAD software. The printed TR-FLS arm will then be weighed and compared. As a second test, the three rotational moments of inertia (MOI) I_{xx}, I_y and I_z are checked analytically. For this, we assume that the end effector forms a rectangular block of homogeneous density with the outer dimensions depicted in Fig. 5.12. The inertia can then be calculated, for example around the X axis, as:

$$I_x = \frac{m(a^2 + b^2)}{12} + mc^2 \tag{5.6}$$

from [28], where a and b are the dimensions of the end effector in the directions Y and Z, and c is the distance from the center of mass to the point where the inertia is to be calculated, perpendicular to the chosen axis. Likewise, inertias I_y and I_z can be calculated. To estimate the mass in equation 5.6, the volume of a solid block with the outer dimensions of the end effector in Fig. 5.12 is calculated and the mass is calculated using the previously validated value for the density. The nuts and bolts are weighed and added to this mass. The inertia is calculated around point P in Fig. 5.12, which is also the point of actuation.

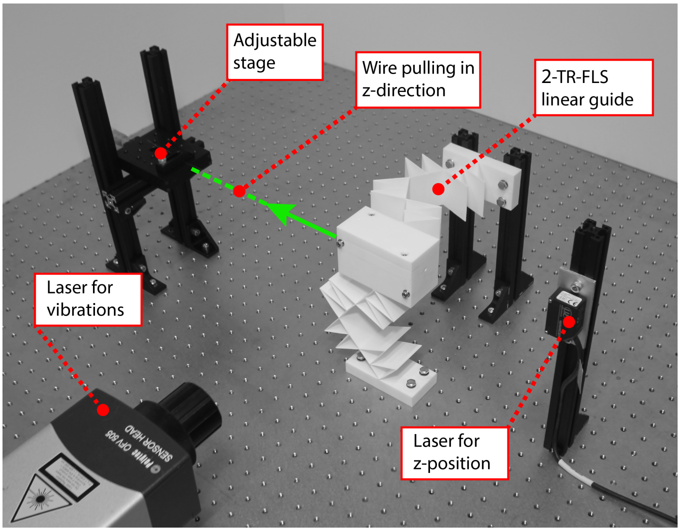

Figure 5.13: Experimental setup for measuring the eigenfrequencies of the 2-TR-FLS design along its range of motion.

Figure 5.13 shows the measurement setup, built on a vibration isolation table. The prototype is driven (actuated) by a thin wire, which is pulled in the Z-direction using the depicted adjustable stage. The z-position is measured using a triangulation laser sensor (optoNCDT 1420). At 11 different z-positions (between every 10 mm of the displacement range), an impulse is applied at different places on the prototype using an impact hammer. The parasitic eigenfrequencies are measured using a laser doppler sensor (Polytec OFV505) aimed perpendicular to the Z-direction. The velocity-time signal is read out by its controller unit (OFV2200), without using the filtering options. This analog signal is converted to digital using a NI USB-6008 DAQ device. The same device is used to read-out the triangulation sensor, ensuring that both data sets have the same time stamp, independently from the processing speed of the laptop which is used to read out this digital signal. The velocity-time signal is analyzed in the frequency domain using the Fast-Fourier Transform (FFT) function in the software package Matlab. From the resulting graphs, the eigenfrequencies on the z-positions can be read out by examining their peaks. The eigenfrequency in the motion direction is measured by removing the wire and using the laser sensor in Z-direction. Because the frequencies are low in this direction, the sample frequency of the triangulation laser suffices. To avoid that modes are not measured, the impulses using the impact hammer are applied at different positions on the end effector and on the rest of the setup. For the same reason, the laser measuring the vibrations are pointed at different positions and angles on the end effector.

5.4.3. EXPERIMENTAL RESULTS

Figure 5.14 shows the experimentally measured parasitic eigenfrequencies of the Nylon prototype when the end effector is positioned at $z = +50\ mm$. Note that higher frequencies are not measured, probably due to the damping of the Nylon. At all 11 z-positions, such a frequency spectrum is plotted and the three lowest frequencies are read out. These are compared to the theoretical data, shown in Fig. 5.15. Each line represents the frequency of a different mode shape, computed with the SPACAR model. The line with lowest values is called the first parasitic mode shape. The black dots represent the experimental data. The eigenfrequency in motion direction at $z = 0$ is 2.1 Hz, as measured with the triangulation sensor. The raw data for all frequency plots, the postprocessing script and the SPACAR model will be published on the Journal of Mechanisms and Robotics website.

To quantify how well the measurements correspond to the SPACAR model, a Normalized Mean Absolute Error (NMAE) is computed for each of the three measured mode shapes. The NMAE is a regular MAE normalized by the maximum value in the displacement range as:

$$\text{NMAE} = \frac{\frac{1}{N}\sum_{n=1}^{N}|\hat{y}_n - y_n|}{max|y|}, \tag{5.7}$$

in which N is the amount of measured data points (11 per mode shape), $\hat{y}$ is the measured data, and y is the SPACAR model data. For the first, second and third parasitic mode shape, the NMAE is 1.3 %, 2.0 % and 4.3 %, respectively. Note the outlier in the third mode shape at z=20 mm, shown in Fig. 5.15. This outlier is included in the NMAE of the third mode shape and causes the higher resulting value.

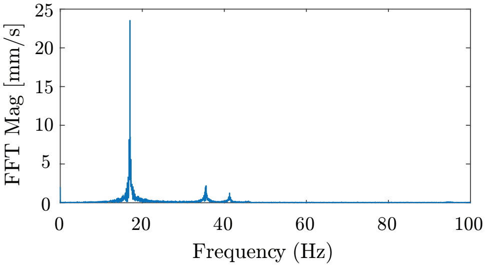

Figure 5.14: Parasitic eigenfrequencies when the end effector is at +50 mm displacement in the z-direction.

The eigenfrequencies in Fig. 5.15 are calculated using the SPACAR software, which in turn uses mass and inertia values at point P of the end effector, calculated by the CAD software Solidworks. The density value used in the CAD software is checked by weighing a single TR-FLS arm. This results in a value of 0.280 kg, whereas the CAD software predicts 0.282 kg. This is an error of 0.71%. The inertia values calculated with the CAD model for I_x, I_y and I_z are 8.56e-4 kgm^2, 9.01e-4 kgm^2 and 1.83e-4 kgm^2, respectively. To check these values first the nuts, bolts and washers connecting the end effector are weighed, resulting in a value of 20.2e-3 kg. The hand calculation of the Nylon part of the

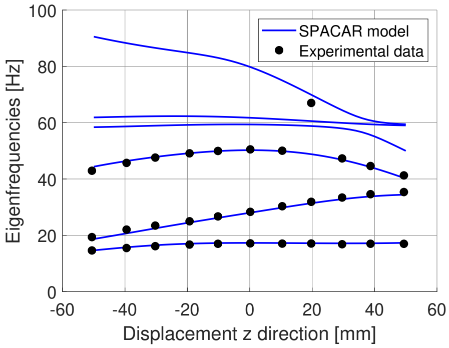

Figure 5.15: Measured and modelled parasitic eigenfrequencies of the Nylon prototype of the 2-TR-FLS design. The eigenfrequency in motion direction (not displayed) is 2.1 Hz.

end effector results in 0.297 kg. The total of these masses is 0.317 kg, which is used to approximately calculate the inertia values, using equation 5.6. This results a I_x, I_y and I_z of 8.22e-4 kgm^2, 8.72e-4 kgm^2 and 1.82e-4 kgm^2, respectively. These values correspond within 5% to the values calculated by the CAD software.

The thickness t_t and t_{ff} measured with a micrometer at 14 positions are 0.99 mm on average, with a maximum deviation of 9 micrometer. The dimensions L_{ff} and H are checked using a caliper, resulting in the expected values of 149 and 40 mm, respectively.

5.5. DISCUSSION

The 2-TR-FLS design has a smaller and less obstructive build volume than the 6FLS, yet it outperforms the 6FLS on the support stiffness metric in table 5.3. The 3-TR-FLS design occupies a build volume similar to that of the 6FLS, but scores four times higher on the support stiffness metric.

The experimental test of the Nylon prototype shown in Fig. 5.15 validates the SPACAR model. There is one outlier in the graph. This measured value could correspond to one of the higher mode shapes. The rest of the data shows good correspondence, as shown in Fig. 5.15. The printing process showed to be very precise, according to the measurements on density and flexure thickness in the Results section. This could explain the good correspondence between experiment and model.

Figures 5.9 and 5.10 show that the support stiffness of the 6FLS design increases at large displacements, which is unexpected. The simulations show that at the point of the support stiffness increase, the material coordinate at the fold line starts moving in the direction opposite to the motion direction (the FLS appears to be ’stretched’). This might explain the support stiffness increase, either because of the decrease in curvature in the leaf springs or because the increase in motion stiffness, which also has a component in the constraining directions.

All designs in this paper have a range comparable to their footprint. This is large compared to existing literature, in which a fraction of the footprint is common. All other properties of the mechanism, such as maximum stress and flexure thickness, are kept in a practically feasible range considering Wire Electrical Discharge Machining of steel, albeit at the upper limit of what is currently possible. Often in industry, shot peening is used to increase the fatigue life of flexures. This postprocessing technique can not directly be applied when torsion reinforcement structures are present.

The optimized 6FLS design has a flexure height H of 22 mm, whereas the other two designs approximate the upper bound of 50 mm in the optimization. This lower value is detrimental to the support stiffness of the 6FLS. The reason that the 6FLS has a lower H value is that the stiffness in the motion direction should be low enough to satisfy the other optimization constraints. Namely, the actuation force should not exceed the 10 Newton limit, while the end effector should reach the intended range of motion. In theory, the thickness t_{ff} could be made very small, solving this problem. However, due to manufacturing limitations this is not a practically feasible solution, and therefore a lower limit of 0.2 mm was imposed on this variable. If there would be no limit on the actuation force, infinitely many flexure elements could be used, increasing the support stiffness indefinitely.

An additional advantage of both the new designs and the 6FLS design is that inaccuracies in the thickness of the flexures have less impact on the motion path, compared to a planar parallelogram design. The TR-FLS element in Fig. 5.3 will constrain the indicated directions, regardless of the motion path of the flexures in the xy plane. This is different from the parallelogram design, in which the in-plane axial constraints of the flexures are necessary to provide linear motion. An inaccuracy in the flexure thickness will affect their motion path, directly affecting the motion of the end effector.

Similar to most planar linear guides, the three spatial linear guides analyzed in this paper are 'overconstrained' [25]. This could be a disadvantage, for example when temperature gradients are present. The 6FLS design has one overconstraint in rotation around the Z axis. This could, for example, be dealt with by adding a notch flexure to one of the flexure elements, or by creating a torsionally compliant end effector [10]. The 2-TR-FLS linear guide has the same overconstraint which could be removed in the same manner. Removing overconstraints in the 3-TR-FLS does not seem practical because of the large number of overconstraints.

Note that a single TR-FLS arm is not overconstrained. To understand this, observe a single triangle in the TR-FLS arm in Fig. 5.3. This triangle consists of a main leaf spring and a torsion reinforcement structure, which in itself is a small folded leaf spring. As explained in Fig. 5.2 and [10], a folded leaf spring adds one constraint to a system. This single constraint is used to suppress the torsional degree-of-freedom of the main flexure. Because the different triangles in the TR-FLS arm are placed in series, no overconstraints are present in a single TR-FLS element.

The 2-TR-FLS design could be further improved. For example, more triangular elements might increase support stiffness. However, in practice the fillets required at the attachment points of these elements will result in a large accumulations of material, increasing the stiffness in the motion direction. This will in turn increase stresses in the mechanism. A more feasible improvement would be to make the flexures tapered in the X and Y direction. The flexures would then fill up the open space in the left figure in Fig. 5.12.

5.6. CONCLUSION

In this work, a new flexure element called the TR-FLS is presented. This element is created by adding torsion reinforcement structures to a folded leaf spring, which increases its constraining directions from one to three. An advantage of this is that only two instead of five or six folded leaf springs are needed to create a linear guide.

A new linear guide consisting of two TR-FLS elements is presented, called the 2-TR-FLS. The design is compared to a pre-existing linear guide consisting of six regular folded leaf springs (6FLS), after optimizing both designs on a support stiffness metric. Compared to the 6FLS design, the 2-TR-FLS design scores over twice as high on the support stiffness metric, while occupying a smaller (-33%) and less obstructive build volume.

A variation on the new linear guide is presented, called the 3-TR-FLS. This linear guide is designed such that it occupies a build volume similar to that of the 6FLS design. After optimizing this design, it scores four times higher on the support stiffness metric compared to the 6FLS design.

A prototype of the 2-TR-FLS design is built and the parasitic eigenfrequencies along its range of motion are measured, validating the SPACAR software used for modelling (Normalized Mean Absolute Error of 4.3%).

ACKNOWLEDGMENT

This work is part of the research programme Möbius with project number 14665, which is (partly) financed by the Netherlands Organisation for Scientific Research (NWO).

REFERENCES

[1] J. Rommers, M. Naves, D. Brouwer, and J. L. Herder, *A flexure-based linear guide with torsion reinforcement structures,* Journal of Mechanisms and Robotics , 1 (2021).

[2] J. Rommers, M. Naves, D. Brouwer, and J. Herder, *A large range spatial linear guide with torsion reinforcement structures,* in *International Design Engineering Technical Conferences and Computers and Information in Engineering Conference,* Vol. 51807 (American Society of Mechanical Engineers, 2018).

[3] L. L. Howell, S. P. Magleby, and B. M. Olsen, *Handbook of compliant mechanisms* (John Wiley & Sons, 2013).

[4] S. T. Smith, *Flexures: elements of elastic mechanisms* (CRC Press, 2000).

[5] R. Leach and S. T. Smith, *Basics of precision engineering* (CRC Press, 2018).

[6] F. Cosandier, S. Henein, M. Richard, and L. Rubbert, *The art of flexure mechanism design* (Epfl Press, 2017).

[7] S. Awtar and G. Parmar, *Design of a large range xy nanopositioning system,* Journal of Mechanisms and Robotics **5** (2013).

[8] Q. Xu, *New flexure parallel-kinematic micropositioning system with large workspace,* IEEE Transactions on Robotics **28**, 478 (2011).

[9] K.-S. Chen, D. Trumper, and S. Smith, *Design and control for an electromagnetically driven x–y–θ stage,* Precision Engineering **26**, 355 (2002).

[10] H. Soemers, *Design Principles for precision mechanisms* (T-Pointprint, 2011).

[11] B. P. Trease, Y.-M. Moon, and S. Kota, *Design of large-displacement compliant joints,* (2005).

[12] R. M. Panas and J. B. Hopkins, *Eliminating underconstraint in double parallelogram flexure mechanisms,* Journal of Mechanical Design **137**, 092301 (2015).

[13] S. Awtar, A. H. Slocum, and E. Sevincer, *Characteristics of beam-based flexure modules,* Journal of Mechanical Design **129**, 625 (2007).

[14] D. M. Brouwer, A. Otten, J. Engelen, B. Krijnen, and H. Soemers, *Long-range elastic guidance mechanisms for electrostatic comb-drive actuators,* in *International Conference of the European Society for Precision Engineering and Nanotechnology (EUSPEN), May* (2010) pp. 41–50.

[15] M. Olfatnia, S. Sood, J. J. Gorman, and S. Awtar, *Large stroke electrostatic comb-drive actuators enabled by a novel flexure mechanism,* Journal of Microelectromechanical Systems **22**, 483 (2013).

[16] N. B. Hubbard, J. W. Wittwer, J. A. Kennedy, D. L. Wilcox, and L. L. Howell, *A novel fully compliant planar linear-motion mechanism,* in *ASME 2004 International Design Engineering Technical Conferences and Computers and Information in Engineering Conference* (American Society of Mechanical Engineers, 2004) pp. 1–5.

[17] B. Krijnen and D. M. Brouwer, *Flexures for large stroke electrostatic actuation in mems,* Journal of micromechanics and microengineering **24**, 015006 (2013).

[18] C. Lee and R. Pan, *Flexure bearing analysis procedures and design charts,* in *Cryocoolers 9* (Springer, 1997) pp. 413–420.

[19] S. Awtar and A. H. Slocum, *Flexure systems based on a symmetric diaphragm flexure,* ASPE1803 (2005).

[20] A. Bos, *Position actuator for the ELT primary mirror*, Ph.D. thesis, Eindhoven University of Technology, The Netherlands (2017).

[21] L. Cacace, *An Optical Distance Sensor: Tilt robust differential confocal measurement with mm range and nm uncertainty*, Ph.D. thesis, Eindhoven University of Technology, The Netherlands. ISBN 978-90-386-2069-5 (2009).

[22] H. Haitjema, P. Rosielle, and H. Steijaert, *A calibration platform for generating parallel displacements with nanometre accuracy,* Proc. of the 9th IPES-4UME, Braunschweig, Germany **2**, 456 (1997).

[23] P. Schellekens, N. Rosielle, H. Vermeulen, M. Vermeulen, S. Wetzels, and W. Pril, *Design for precision: current status and trends,* Cirp Annals **47**, 557 (1998).

[24] J. B. Hopkins, *A visualization approach for analyzing and synthesizing serial flexure elements,* Journal of Mechanisms and Robotics **7** (2015).

[25] L. C. Hale, *Principles and techniques for designing precision machines*, Tech. Rep. (Lawrence Livermore National Lab.(LLNL), Livermore, CA (United States), 1999).

[26] J. B. Hopkins and M. L. Culpepper, *Synthesis of multi-degree of freedom, parallel flexure system concepts via freedom and constraint topology (fact)–part i: Principles,* Precision Engineering **34**, 259 (2010).

[27] F. S. Ugural AC, *Advanced Strength and Applied Elasticity* (Prentice Hall PTR, 2003).

[28] R. Hibbeler, *Mechanics of Materials* (Prentice Hall, 2005).

[29] D. Wiersma, S. Boer, R. Aarts, and D. Brouwer, *Design and performance optimization of large stroke spatial flexures,* Journal of Computational and Nonlinear Dynamics **9** (2014), 10.1115/1.4025669.

[30] M. Naves, D. Brouwer, and R. Aarts, *Building block-based spatial topology synthesis method for large-stroke flexure hinges,* Journal of Mechanisms and Robotics **9** (2017), 10.1115/1.4036223.

[31] J. A. Nelder and R. Mead, *A simplex method for function minimization,* The computer journal **7**, 308 (1965).

[32] J. Jonker and J. Meijaard, *Spacar—computer program for dynamic analysis of flexible spatial mechanisms and manipulators,* in *Multibody systems handbook* (Springer, 1990) pp. 123–143.

[33] M. Faes, Y. Wang, P. Lava, and D. Moens, *Variability in the mechanical properties of laser sintered pa-12 components,* in *Proceedings of the 26th annual international solid freeform fabrication symposium. Solid freeform fabrication symposium* (2015) pp. 847–56.

6

A NEW TYPE OF SPHERICAL FLEXURE JOINT BASED ON TETRAHEDRON ELEMENTS

In this chapter, a new tetrahedron element is presented, which is a generalized version of the blade flexure with torsion reinforcement (here referred to as a triangular prism element). The tetrahedron element is used to create two new spherical flexure joint designs, which are the compliant equivalent of a ball-and-socket joint. The tetrahedron elements are connected in series without intermediate bodies, which is new with respect to the designs currently found in literature and which helps to increase the range of motion. For detailed investigation, equivalent representations of the tetrahedron and prism elements are presented which are used to prove that three of the four constraint stiffness terms depend solely on the properties of the main blade flexure. Furthermore, equations for these stiffness terms are derived which are compared to finite-element simulations, showing a good correspondence for the prism element with a Normalized Mean Absolute Error (NMAE) of 1.9%. For the tetrahedron element, the equations showed to only capture the qualitative behaviour with a NMAE of 34.9%. Also, an equation for the optimal width of the prism element regarding rotational stiffness is derived.

This chapter has been published in the journal of Precision Engineering [1]. A video can be found here.

6.1. INTRODUCTION

Spherical flexure joints can provide a high-precision alternative for traditional ball-and-socket joints. This is because they gain their motion due to the deflection of slender segments such as thin spring steel plates, which eliminates friction and backlash in the rolling and sliding surfaces in these traditional joints. Four types of spherical flexure joint designs can currently be distinguished in literature [2], all allowing solely three rotations in a single point.

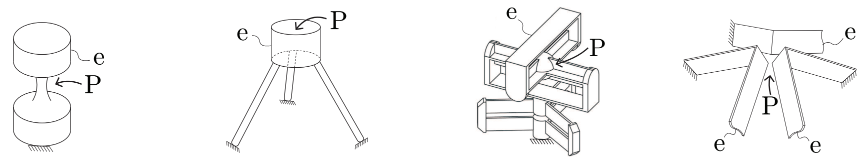

(a) (b) (c) (d)

Figure 6.1: Overview of the current state-of-the-art spherical flexure joints from [2], where *P* denotes the center of rotation and *e* the end effector: (a) a spherical notch joint or short wire flexure [3]; (b) three wire flexures with intersecting axes [4, 5]; (c) three revolute flexure joints in series with intersecting motion axes [6, 7]; (d) three folded leaf springs with intersecting fold lines [2, 4, 8].

The first type consists of a rod with a thinner part or short wire as illustrated in Fig. 6.1a [3], which allows solely three rotations because all strains are concentrated in the thinner part. The second type consists of three wire flexures or slender rods which intersect in a common point as shown in Fig. 6.1b [4, 5], where each wire flexure constrains one translational motion. The third design type is based on the traditional (rigid-body) spherical linkage in which the axes of three revolute joints intersect in a single point. The revolute joints have been replaced by a flexure-based counterpart for which there are various possibilities, for example as illustrated in Fig. 6.1c [6, 7]. The fourth type shown in Fig. 6.1d can be regarded as the design of Fig.1b with the wire flexures replaced with 'folded leaf springs' [2, 4, 8], which each also constrains one translational motion [4].

The second, third and fourth design types have special configurations where they degenerate to planar joints which allow two in-plane translations and one rotation. For example in design type two in Fig. 6.1b, where the length axes of the wire flexures intersect in the rotation point *P*. If point *P* is shifted to infinity in the vertical direction, the wire flexures become parallel and a planar joint results. In a similar way, design type four shown in Fig. 6.1d degenerates into a planar joint when the fold lines of the folded leaf springs become parallel. The third design type shown in Fig.6.1c also has a planar version which consists of two links and three revolute flexure joints with parallel rotation axes.

In this paper, we present a new type of spherical flexure joint which is formed by a serial connection of tetrahedron-shaped elements. We present two design variations named the Tetra I and Tetra II, and also present their planar derivatives in which the tetrahedron elements degenerate into triangular prisms. We have published one of these planar versions in earlier work [9] where the triangular prism was inspired by the 'infinity hinge' from [10, 11]. In this paper we show that the tetrahedron element is a generalized version of the triangular prism.

In section 6.2 we present the joint designs and explain how they function. The tetrahedron element is studied in detail in section 6.3 by means of an equivalent representation. Equations for the stiffness terms are derived and compared to finite-element simulations. In section 6.4 we discuss the results and in section 6.5 we summarize the contributions of this work.

Throughout the article, we refer to motions of a body as being *free* when a significantly low stiffness is being experienced in that direction, and as *constrained* in the case of a significantly high stiffness. A flexure typically adds *constraints* to a body, meaning that it stiffens certain motion directions of the body [12].

6.2. DESIGNS OF THE TWO NEW SPHERICAL FLEXURE JOINTS AND THEIR PLANAR DERIVATIVES

In this section we first present the designs of two new spherical flexure joints and subsequently we present their planar derivatives. The designs consist of tetrahedron elements connected in series. In the first design, the elements are connected along two arms as illustrated in Fig. 6.2, while in the second design the elements form a nested configuration as illustrated in Fig. 6.5.

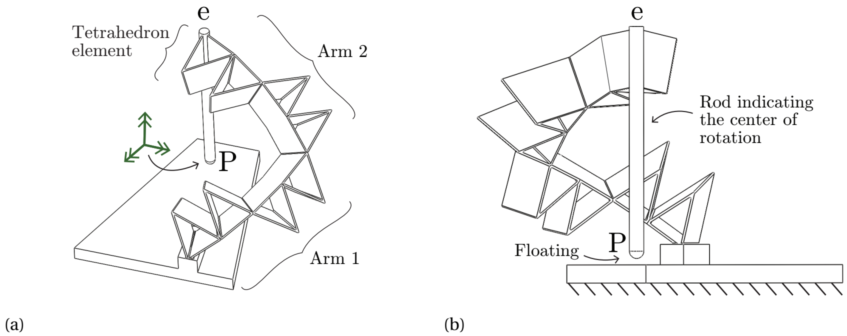

Figure 6.2: The Tetra I spherical flexure joint design, shown from two sides, based on two arms under an angle consisting each of four tetrahedron elements. Point P is the remote center of rotation, indicated by the rod eP.

The first design, named Tetra I, is shown in Fig. 6.2a. It can be considered as consisting of two arms, each built up from four tetrahedron elements and with e as the end-effector. For illustration, in e a rod is placed which ends in point P, the remote center of rotation of the flexure joint which floats in space. The flexures constrain the end effector e such that solely the three rotations about point P are free. If, for example, a horizontal force is applied at the top of the joint in e, the joint rotates about point P as shown in the two deformed states (scaled 1:1) in Fig. 6.3.

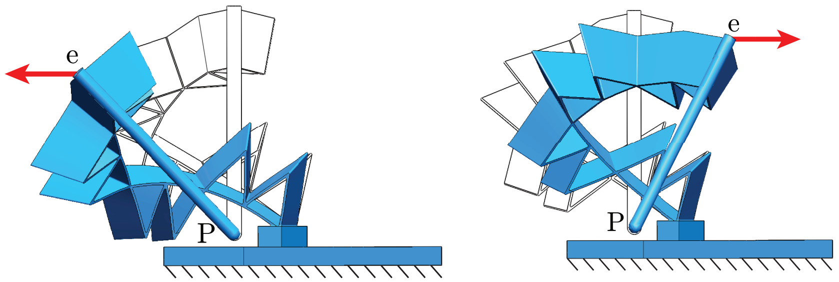

(a) (b)

Figure 6.3: The Tetra I design subjected to a horizontal load at e, showing that it rotates about point P (scaled 1:1).

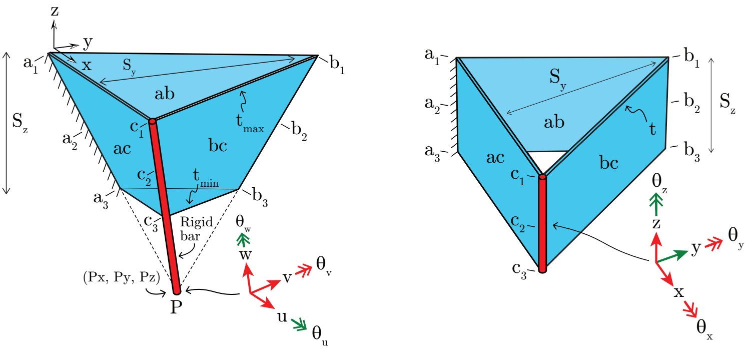

(a) (b)

Figure 6.4: (a) Tetrahedron element formed by three blade flexures, with its parameters; (b) Specific degenerated case when P lies at infinity, for which the form reduces to a triangular prism.

The working principle of the Tetra I design is as follows. The two arms each consist of four tetrahedron elements. A single tetrahedron element, shown isolated in Fig. 6.4, consists of three blade flexures ac, ab and bc. Edges a_1a_3 and c_1c_3 are the interfaces at which other tetrahedron elements can be connected and therefore blade flexure ac is considered as the main (connecting) blade flexure. In the isolated view, we consider edge a_1a_3 as fixed and the rigid bar through edge c_1c_3 as the end effector. The three blade flexures have a trapezoidal shape and the lines through their edges form a tetrahedron shape, as illustrated in Fig. 6.4. Coordinate system xyz is placed with its origin at point a_1. Axis x is aligned with line a_1c_1 and axis y is in the plane formed by points $a_1b_1c_1$. Coordinate system uvw has the same orientation as system xyz, except that it is rotated around the x-axis such that v is perpendicular to the plane of blade flexure ac. The rigid bar is free to rotate around the axes u and w, which lie in the plane of blade flexure ac. This is because the planes formed by the three blade flexures intersect in point P, as will be explained in more detail in section 6.3.2. In order to achieve spherical motion, rotation around the third axis v perpendicular to the plane of blade flexure ac should also be free. This is accomplished by connecting a second tetrahedron under an angle with respect to the first tetrahedron, such that the main blade flexures of the two tetrahedron elements are not coincident. For example, the fourth and fifth tetrahedron of the Tetra I design shown in Fig. 6.2a are connected under an angle with respect to each other in order to free the rotation around the third axis. The tetrahedron elements should be connected such that their rotation points coincide, which means that the planes of all blade flexures in the spherical joints intersect point *P*. In principle, the spherical flexure joint design needs solely two tetrahedrons under an angle to function properly. However, each of the tetrahedrons can also be replaced by a set of tetrahedrons in series in order to increase the range of motion and to avoid collisions, such as in the Tetra I design in Fig. 6.2a which consists of four tetrahedrons in each arm, paired two by two on each side.

The second new design of a spherical flexure joint named Tetra II is shown in Fig. 6.5a. This design also consists of tetrahedron elements, however assembled in a nested configuration. The tetrahedron elements are constructed in series, similar as in the Tetra I design in which the two arms are formed by a serial connection of tetrahedron elements. Also in the Tetra II design, point *P* is the remote center of rotation. If, for example, a horizontal force is applied at point *e*, the joint rotates about *P* as shown in the deformed state (scaled 1:1) in Fig. 6.5b. A movie of this design can be found online using the DOI of this article, in which the motions of an additively manufactured titanium version are demonstrated. Two tetrahedron elements connected under an angle are sufficient for spherical motion, while the third element was added to improve the range of motion. Note that the three tetrahedron elements not only differ in size, but also in shape. This is different from the Tetra I design, where all tetrahedron elements have the same shape and size. Changing the shape of the tetrahedron elements does not change the kinematics of the spherical joint, as long as the planes of all three blade flexures forming the tetrahedron elements coincide in point *P*. This will be explained in more detail in section 6.3.2.

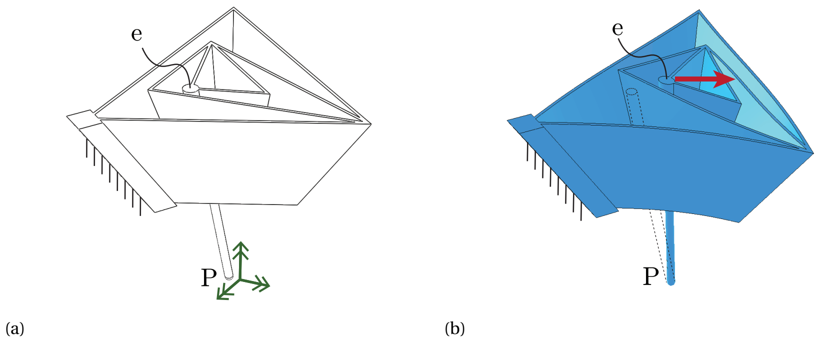

(a) (b)

Figure 6.5: (a) The Tetra II spherical flexure joint design based on nested tetrahedron elements; (b) Deflected pose due to a load showing the rotational motion about *P*.

Both of the spherical joint designs Tetra I and II in Figs. 6.2 and 6.5 have a specific case for which they become planar joints, shown in Figs. 6.6a and 6.6b, respectively. Here the tetrahedron elements have become triangular prism elements as shown in Fig. 6.4b. The mobility of the end effector e is no longer spherical. In both designs the end effectors have 3-DoF planar motion capability, with an x- and y-translation and an in-plane rotation θ_z. The transformation from spherical to planar mobility can be understood as follows. The end effector e of a spherical joint moves over the surface of a sphere. If the radius of this sphere is infinitely large, the spherical surface degenerates to a plane. This means that the motions of the joint also become planar. A requirement for the planar joints is that the planes of all blade flexures should be parallel to a single axis, as will be explained in more detail in section 6.3.2. In [9] we have already shown how planar joint 1 can be applied for the design of a linear guide.

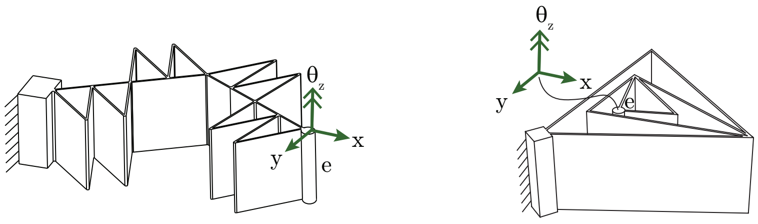

(a) (b)

Figure 6.6: (a) 3-DoF planar joint 1, derived as special case from the Tetra I design in Fig. 6.2a; (b) 3-DoF planar joint 2, derived as special case from the Tetra II design in Fig. 6.5a.

The four joint designs presented in this section are based on distributed compliance, which enables a significant range of motion. Figure 6.7 shows a finite-element simulation of planar joint 1, forced in a straight-line motion. The flexures show a gradual curvature, which means that the strains are well distributed over the whole joint. If the prism elements would be solid, high peak stresses would occur in the connection points which would significantly limit the range of motion.

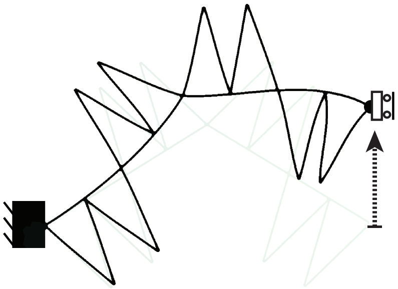

Figure 6.7: Illustration of the distributed compliance by a finite-element simulation of planar joint 1 forced in a straight-line motion [9]. The distributed strains enable a large range of motion.

6.3. THE TETRAHEDRON AND PRISM ELEMENTS IN DETAIL

At the core of the four presented joints lie the tetrahedron and prism elements, of which we explain the functioning in detail in this section. Using equivalent representations we analyze their degrees of freedom and derive stiffness equations for their constraining directions, which we compare to finite-element simulations. We assume that blade flexures ab and bc have equal lengths, and that for the tetrahedron element $P_x = L_{a_1c_1}/2$ and $P_y = 0$, with P_x and P_y the x- and y-coordinates of the remote center of rotation as illustrated in Fig. 6.4a.

6.3.1. EQUIVALENT REPRESENTATIONS OF THE TETRAHEDRON AND PRISM ELEMENTS

Analysis of the tetrahedron and prism elements is not evident because the three blade flexures form a hybrid serial and parallel configuration: blade flexures ab and bc form a serial path from ground to the end effector (edge c_1c_3), and blade flexure ac forms a second, parallel path. It is not directly clear which stiffness blade flexure bc applies to the end effector because it is connected to the fixed world via blade flexure ac. The goal of the equivalent representation is to simplify the tetrahedron and prism element such that they consist of two parallel flexure elements. This is done by replacing blade flexures ab and bc with a single wire flexure and extending the end effector using a rigid bar, as illustrated in Fig. 6.8. Points a_2, b_2 and c_2 are in the middle of the edges. Edge c_1c_3 in the equivalent mechanism is still the end effector, which is extended such that it forms the rigid part. Two parallel paths are present: the wire flexure and blade flexure ab. In the following, we explain why these equivalent representations are valid.

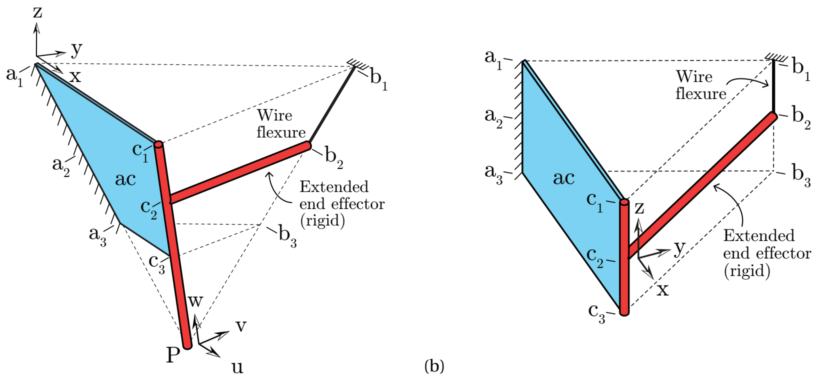

(a)

(b)

Figure 6.8: (a) Equivalent representation of the tetrahedron element where blade flexures ab and bc are replaced with a rigid part and a wire flexure; (b) Similar equivalent representation of the prism element.

We start with the equivalent representation of the special prism element. Blade flexures ab and bc in the original prism element form a folded leaf spring (or double blade flexure), as illustrated in Fig. 6.9a. An equivalent rigid-body model of this folded leaf

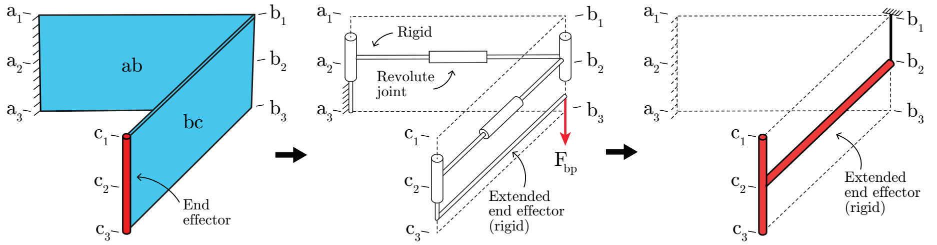

(a) (b) (c)

Figure 6.9: Blade flexures *ab* and *bc* of the prism element form a folded leaf spring as illustrated in a), which solely counteracts forces collinear with edge $b_1 b_3$ as shown in the equivalent rigid-body model in b). Therefore, they can be modeled with a wire flexure and rigid bar illustrated in c).

spring is illustrated in Fig. 6.9b, in which the deformation modes with low stiffness are represented by revolute joints connected by rigid bars, as in [6]. The end effector is extended with a rigid bar which runs to underneath point b_2. The force F_{bp} is constrained because it either intersects or is parallel to each of the rotation vectors of the revolute joints [13], such that it does not result in a moment around any of the revolute joints. This is solely the case for forces collinear with the rotation axis of the revolute joint at b_2. Moments are not counteracted by the folded leaf spring because the rotation vectors of the revolute joints span the full space. A wire flexure coincident with edge $b_1 b_3$ constrains the same motions and is therefore kinematically equivalent to the folded leaf spring. Therefore, the rigid bar and wire flexure illustrated in Fig. 6.9c can be used to replace blade flexures *ab* and *bc*. The same reasoning can be used to explain why the equivalent representation of the tetrahedron is valid. Also in this case, the folded leaf spring formed by blade flexures *ab* and *bc* of the tetrahedron element solely resists forces collinear with edge $b_1 b_3$. A wire flexure placed at this edge can replace blade flexures *ab* and *bc*, as illustrated in Fig. 6.8a. In earlier work [9], we presented an explanation largely similar to the one in this paragraph. A different explanation can be found in [14] where instead of adding the free directions of the two blade flexures *ab* and *bc*, the author analyzes the overlap of their constraints using an ‘intermediate constraint space’.

The equivalent representations in Fig. 6.8 are only valid for small deflections from the initial shape since the wire flexure suffers from a shortening effect at larger displacements. This shortening does not occur in a folded leaf spring.

6.3.2. DEGREES OF FREEDOM OF THE TETRAHEDRON AND PRISM ELEMENTS

Using the equivalent representations and constraint-based design (CBD) methods [12, 13, 15], the degrees of freedom of the tetrahedron and prism elements can be understood. We start with the tetrahedron element. Using CBD, the blade flexure *ac* is represented by three ‘constraint lines’ running through points $a_1 c_1$, $a_3 c_3$ and $a_1 c_3$ in Fig. 6.8a. A fourth constraint line at the place of the wire flexure represents this element. The CBD methods state that the end effector is solely free to rotate around axes which intersect all constraint lines. This means that the tetrahedron element is solely free to rotate around the axes which lie in the plane of blade flexure ac and intersect point P. This results in the two independent rotations around axes u and w illustrated in Fig. 6.4a.

The same method can be applied to the prism element, which is created by shifting the rotation point P of the tetrahedron element at infinity in the z-direction. Assume that the first of the two independent rotation axes of the tetrahedron element is collinear with edge c_1c_3, and the second one is perpendicular to this edge (but in the plane of blade flexure ac). In the prism element, the first axis still intersects all constraint lines because the constraint line representing the wire flexure is intersected at infinity. This means that the prism is free to rotate around the y-axis in Fig. 6.8b. The second rotation axis perpendicular to edge c_1c_3 and in the plane of blade flexure ac lies at infinity because point P lies at infinity in the z-direction. This rotation at infinity results in the translational degree of freedom of the prism element in the direction perpendicular to blade flexure ac. In CBD, this freedom line is represented by a 'hoop' in the plane of blade flexure ac.

6.3.3. EQUIVALENT STIFFNESS OF THE WIRE FLEXURE

In order to calculate the stiffness terms of the tetrahedron and prism elements in the next sections, we need to know the longitudinal stiffness of the wire flexure such that it represents the stiffness due to blade flexures ab and bc. In the prism element, blade flexures ab and bc form a folded leaf spring with parallel edges, of which this stiffness K_{bp} is given by [4] using linear beam theory, as:

$$K_{bp} = \left[\frac{L_{a_2b_2}^3 + L_{b_2c_2}^3}{3EI_p} + \frac{6(L_{a_2b_2} + L_{b_2c_2})}{5Gth} \right]^{-1}, \tag{6.1}$$

where $L_{a_2b_2} = \sqrt{L_{a_2c_2}^2/4 + S_y^2}$ is the distance between point a_2 and b_2, or the length of blade flexure ab. S_y is the width of the total element, which is the dimension in the y-direction in Fig. 6.4b. E and G are the Young's modulus and shear modulus, respectively. The area moment of inertia is $I_p = tS_z^3/12$, where t and S_z are the thickness and height of the blade flexures as indicated in Fig. 6.4b. The first and second term in brackets in equation 6.1 describe the displacement due to bending and shear, respectively. Because we assume that the lengths of the blade flexures ab and bc are equal, $L_{a_2b_2} = L_{b_2c_2}$ and equation 6.1 can be simplified to:

$$K_{bp} = \left[\frac{2L_{a_2b_2}^3}{3EI_p} + \frac{12L_{a_2b_2}}{5Gth} \right]^{-1}. \tag{6.2}$$

The equivalent stiffness of the wire flexure for the tetrahedron element is more complex to calculate, because the blade flexures have a trapezoidal outline and therefore linear beam theory is not directly applicable. To approximate the lateral stiffness of blade flexure ab, we take the average stiffness of two beams, one with length $L_{a_1b_1}$ and one with $L_{a_3b_3}$, as indicated in Fig. 6.4. In this way, the equivalent stiffness for the wire flexure K_b is approximated as:

$$K_b = \left[\frac{4}{3EI/L^3_{a_1 b_1} + 3EI/L^3_{a_3 b_3}} + \frac{24}{5GA/L_{a_1 b_1} + 5GA/L_{a_3 b_3}} \right]^{-1}, \tag{6.3}$$

where

$$L_{a_1 b_1} = \sqrt{L^2_{a_1 c_1}/4 + S^2_y} \tag{6.4}$$

and

$$L_{a_3 b_3} = \frac{P_z - S_z}{P_z} L_{a_1 b_1}. \tag{6.5}$$

The thickness in the blade flexures of the tetrahedron varies linearly in the z-direction, indicated by t_{max} and t_{min} in Fig. 6.4a. The thickness changes proportionally with the length of the line segments of the top triangle $a_1 b_1 c_1$ and the bottom triangle $a_3 b_3 c_3$. This is to make sure that the bending stresses due to displacement in the motion direction have an even distribution in the z-direction of the element. This means that:

$$t_{max} = \frac{P_z}{P_z - S_z} t_{min}. \tag{6.6}$$

We approximate the height of the blade flexures by S_z, which is the height of the total tetrahedron excluding the rigid bar in Fig. 6.4a. The cross-sectional area in equation 6.3 is then:

$$A = (t_{min} + t_{max}) S_z/2. \tag{6.7}$$

Note that we approximate the shear deformation in equation 6.3 by using the shear constant for a rectangular cross section. The moment of inertia I for the trapezoidal cross-section is given by [16] as:

$$I = \frac{S^3_z \left(t_{\text{min}}{}^2 + 4\, t_{\text{min}}\, t_{\text{max}} + t_{\text{max}}{}^2 \right)}{36(t_{min} + t_{max})}, \tag{6.8}$$

where we also approximate the height of the blade flexures by S_z.

6.3.4. CONSTRAINT STIFFNESS TERMS OF THE PRISM ELEMENT

In this section we derive analytic expressions for the stiffness of the end effector (edge $c_1 c_3$) in the four constraining directions of the prism element illustrated in Fig. 6.4b, using its equivalent representation. Throughout the following sections we use linear beam equations to calculate the stiffness of the blade flexures, which can be found in for example [16, 17]. We neglect the stiffness in the free (low-stiffness) directions of the blade and wire flexures.

We start with K_{θ_x}, which is the rotational stiffness of edge $c_1 c_3$ around the x-axis as illustrated in Fig. 6.8b. For this we apply a moment M_{ext} around the x-axis, determine the reactions on the blade and wire flexure, compute their corresponding displacements and from this determine the rotation around the x-axis. Figure 6.10a shows the rigid part of the equivalent representation, in the yz-plane. The external moment M_{ext} is applied at edge $c_1 c_3$ and results in forces F_{cp} from the blade flexure, and F_{bp} from the wire flexure. Note that both the blade and the wire flexure are free to rotate around the x-axis and

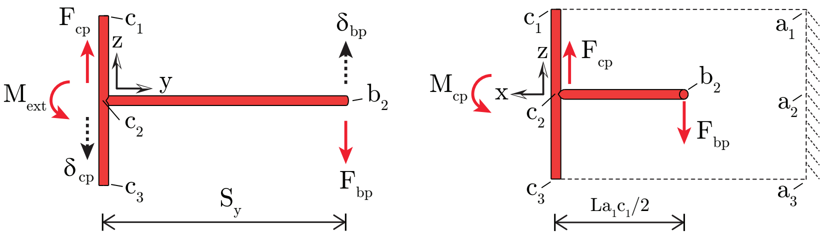

(a) (b)

Figure 6.10: Model for determining the rotational stiffness K_{θ_x} around the x-axis of the prism of Fig. 6.4b by considering a moment M_{ext} at c_2 on the rigid part of the equivalent representation, shown in the yz-plane (a) and xz-plane (b).

therefore cannot exert a moment in the yz-plane. The displacements δ_{bp} and δ_{cp} fully determine the rotation around the x-axis, which means that the rotational stiffness can be written as:

$$K_{\theta_x} = \frac{M_{ext}}{\delta_{bp} S_y + \delta_{cp} S_y}. \tag{6.9}$$

What is left is to determine δ_{bp} and δ_{cp} as a result of M_{ext}. We start with δ_{bp}. Static equilibrium in the yz-plane gives:

$$\delta_{bp} = \frac{F_{bp}}{K_{bp}} = \frac{M_{ext}/S_y}{K_{bp}}, \tag{6.10}$$

where K_{bp} is the equivalent stiffness of the wire flexure from equation 6.1. Displacement δ_{cp} is more complex to calculate since M_{ext} not only results in a force F_{cp} on the blade flexure but also introduces a moment M_{cp}, as illustrated in 6.10b where the rigid part is showed in the xz-plane. This moment counteracts the displacement caused by the force F_{cp}. The total displacement can be calculated as:

$$\delta_{cp} = F_{cp}\left[\frac{L_{a_2c_2}^3}{3EI_p} + \frac{6L_{a_2c_2}}{5Gth}\right] - M_{cp}\frac{L_{a_2c_2}^2}{2EI_p}, \tag{6.11}$$

where the first term is the displacement due to the force and the last term is the displacement due to the moment. Using the free-body diagrams in Fig. 6.10 it can be shown that $M_{cp} = F_{cp}L_{a_2c_2}/2$ and $F_{cp} = M_{ext}/S_y$, which gives:

$$\delta_{cp} = \frac{M_{ext}}{S_y}\left[\frac{L_{a_2c_2}^3}{12EI_p} + \frac{6L_{a_2c_2}}{5Gth}\right]. \tag{6.12}$$

Substituting equations 6.12, 6.10, and 6.1 in 6.9 and rearranging gives the stiffness around the x-axis as:

$$K_{\theta_x} = S_y^2 \left[\frac{\frac{L^3_{a_2c_2}}{4} + L^3_{a_2b_2} + L^3_{b_2c_2}}{3EI_p} + \frac{6(L_{a_2c_2} + L_{a_2b_2} + L_{b_2c_2})}{5Gth} \right]^{-1}, \tag{6.13}$$

where $L_{a_2b_2} = L_{b_2c_2} = \sqrt{L^2_{a_2c_2}/4 + S_y^2}$.

The stiffness terms in the other constraining directions of the prism element solely depend on blade flexure ac. This can be proven as follows, using the equivalent representation in Fig. 6.8b. If the wire flexure contributes to the stiffness, it causes a reaction force in the z-direction on the rigid part in point b. Moment equilibrium in the yz-plane can then not be satisfied, because the blade and wire flexure are free to rotate in this plane. Solely the stiffness K_{θ_x} is dependent on the wire flexure, because in that case the external moment M_{ext} in Fig. 6.10a makes moment equilibrium possible. The translational stiffness in z-direction of edge c_1c_3 is therefore simply equal to the lateral stiffness of blade flexure ac as:

$$K_z = \left[\frac{L^3_{a_2c_2}}{3EI_p} + \frac{6L_{a_2c_2}}{5Gth} \right]^{-1}. \tag{6.14}$$

Using the same reasoning, a moment around the y-axis is solely counteracted by flexure ac and therefore the rotational stiffness around the y-axis is:

$$K_{\theta_y} = \frac{EI_p}{L_{a_2c_2}}, \tag{6.15}$$

and finally the translational stiffness in x-direction is:

$$K_x = \frac{EtS_z}{L_{a_2c_2}}. \tag{6.16}$$

6.3.5. CONSTRAINT STIFFNESS TERMS OF THE TETRAHEDRON ELEMENT

In this section, we derive equations for the stiffness in the four constraining directions of the tetrahedron element, as illustrated in Fig. 6.4a. The procedure is similar to that of the prism, except that we approximate the stiffness of the flexures because of their trapezoidal shape. For simplicity, we assume that $P_y = 0$ in Fig. 6.4a, such that blade flexure ac is vertical and coordinate system uvw aligns with system xyz.

We start with the translational stiffness at point P in v-direction K_v, as illustrated in Fig. 6.4a. Consider the equivalent representation shown in Fig. 6.8a. The free-body diagram of the rigid part after application of a force F_{ext} at point P in the v-direction is shown in Fig. 6.11. The displacement of P δ_P in the v-direction is fully defined by the displacements δ_b and δ_c. Because the deformations are small, we can calculate the contributions of the two displacements δ_b and δ_c to the displacement of P separately and then add them [17]. We start with the contribution of δ_b. Static equilibrium gives:

$$\frac{F_{ext}}{F_b} = \frac{S_y}{\sqrt{S_y^2 + P_z^2}}. \tag{6.17}$$

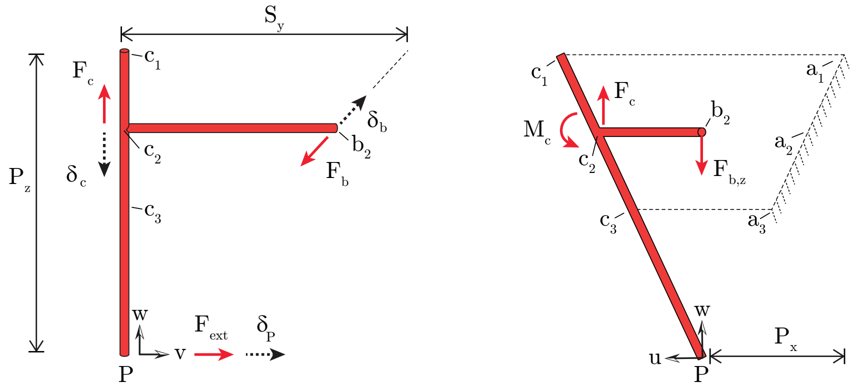

(a) (b)

Figure 6.11: Model for determining the translation stiffness K_v in point P of the tetrahedron element in Fig. 6.4a by considering a force F_{ext} on the rigid part of the equivalent representation, shown in the vw-plane (a) and uw-plane (b).

The displacements are related by the reciprocal of this transmission ratio [4] as:

$$\frac{\delta_{P,b}}{\delta_b} = \frac{\sqrt{S_y^2 + P_z^2}}{S_y}, \tag{6.18}$$

where $\delta_{P,b}$ is the displacement of P in v-direction due to the displacement δ_b. The displacement of P in the v-direction as a result of displacement δ_c can be derived in the same way as:

$$\frac{\delta_{P,c}}{\delta_c} = \frac{P_z}{S_y}. \tag{6.19}$$

The stiffness K_v is the external force divided by the total displacement in v-direction of point P:

$$K_v = \frac{F_{ext}}{\delta_{P,c} + \delta_{P,b}} = \frac{F_{ext}}{\frac{P_z}{S_y}\delta_c + \frac{\sqrt{S_y^2+P_z^2}}{S_y}\delta_b}. \tag{6.20}$$

What remains is to find the displacements δ_b and δ_c due to force F_{ext}. The displacement δ_b is simply the force F_b divided by the stiffness of the wire flexure:

$$\delta_b = \frac{F_b}{K_b} = \frac{\frac{\sqrt{S_y^2+P_z^2}}{S_y}F_{ext}}{K_b}, \tag{6.21}$$

where K_b is the equivalent stiffness of the wire flexure from equation 6.3. The displacement δ_c is computed in a similar way as for the prism element. The free-body diagram in Fig. 6.11b shows that, similar to the computation for the prism, a moment counteracts the displacement due to the force F_c. Note that $F_{b,z}$, the component of F_b in z-direction, is equal to F_c. This force acts on an arm which is half the length of blade flexure ac, and therefore the term between the brackets in equation 6.12 for the prism element can be used to compute the displacement δ_c. However, because the blade flexures have a trapezoidal shape, we compute their average stiffness using the two lengths $L_{a_1c_1}$ and $L_{a_3c_3}$, similar to the procedure for the equivalent wire flexure for the tetrahedron element in section 6.3.3. Noting that $F_c = F_{ext}P_z/S_y$, the displacement δ_c is approximated as:

$$\delta_c = F_{ext}\frac{P_z}{S_y}\left[\frac{2}{12EI/L^3_{a_1c_1}+12EI/L^3_{a_3c_3}}+\frac{12}{5GA/L_{a_1c_1}+5GA/L_{a_3c_3}}\right], \tag{6.22}$$

where

$$L_{a_3c_3} = \frac{P_z-S_z}{P_z}L_{a_1c_1}. \tag{6.23}$$

Substituting equations 6.22, 6.21 and 6.3 in 6.20 yields the stiffness K_v in v-direction at point P:

$$\begin{aligned} K_v = S_y^2\Bigg[&\frac{2P_z^2}{12EI/L^3_{a_1c_1}+12EI/L^3_{a_3c_3}}+\frac{12P_z^2}{5GA/L_{a_1c_1}+5GA/L_{a_3c_3}} \\ &+\frac{4(S_y^2+P_z^2)}{3EI/L^3_{a_1b_1}+3EI/L^3_{a_3b_3}}+\frac{24(S_y^2+P_z^2)}{5GA/L_{a_1b_1}+5GA/L_{a_3b_3}}\Bigg]^{-1} \end{aligned} \tag{6.24}$$

The stiffness in the other three constraining directions of the tetrahedron element solely depend on blade flexure ac. This is because a reaction force in the wire flexure has a component in the v-direction, which is not counteracted by the blade flexure because it is free in that direction. Therefore, the wire flexure is only active in the case of a force at P with a component in the v-direction, which means that solely constraint stiffness K_v depends on the wire flexure.

To compute the translation stiffness in the w-direction K_w, consider a force at P in the w-direction on the equivalent representation in Fig. 6.11b. This force will induce a force and a moment at edge c_1c_3 on blade flexure ac, which counteracts its displacement in the same way as when computing equation 6.22. Because again the moment arm of the force is half of the length of blade flexure ac, we can simply use the terms in brackets in equation 6.22:

$$K_w = \left[\frac{2}{12EI/L^3_{a_1c_1}+12EI/L^3_{a_3c_3}}+\frac{12}{5GA/L_{a_1c_1}+5GA/L_{a_3c_3}}\right]^{-1}. \tag{6.25}$$

To compute the stiffness in the u-direction K_u, consider the uw-view of the equivalent representation in Fig. 6.11b. The stiffness K_u is dependent on the axial deformation of blade flexure ac and the torsional stiffness around its v-axis with moment arm $P_z - S_z/2$ as:

$$K_u = \left[\frac{L_{a_2c_2}}{EA}+\frac{(P_z-S_z/2)^2L_{a_2c_2}}{EI}\right]^{-1}, \tag{6.26}$$

where we approximate the length of blade flexure ab using $L_{a_2c_2} = (L_{a_1c_1} + L_{a_3c_3})/2$. Similarly, the rotational stiffness K_{θ_v} is:

$$K_{\theta_v} = EI/L_{a_2c_2} \tag{6.27}$$

6.3.6. COMPARISON OF THE EQUATIONS TO FINITE-ELEMENT SIMULATIONS

In this section we compare the stiffness equations to simulations with the finite-element modeling (FEM) software package Comsol. For this we define a 'standard design' for both the tetrahedron and prism element. As a second test, we vary the design parameters one-by-one from this standard design and compare the effect on the stiffness change using graphs and an error metric.

Variable	Tetrahedron	Prism
$L_{a_1c_1}$	50 [mm]	50 [mm]
S_y	50 [mm]	50 [mm]
S_z	25 [mm]	25 [mm]
t_{min}	0.5 [mm]	-
t	-	0.5 [mm]
P_x	25 [mm]	25 [mm]
P_y	0 [mm]	0 [mm]
P_z	50 [mm]	infinite
E	210 [GPa]	210 [GPa]
G	80 [GPa]	80 [GPa]

Table 6.1: Parameters of the chosen standard designs of the tetrahedron and prism element.

Stiffness term	FEM	Equations	Error
K_x [N/m]	5.32e7	5.25e7	1.36%
K_y [N/m]	3.14e3	free	-
K_z [N/m]	2.78e6	2.74e6	1.36%
K_{θ_x} [Nm/rad]	2.27e3	2.23e3	1.75%
K_{θ_y} [Nm/rad]	2.81e3	2.73e3	2.52%
K_{θ_z} [Nm/rad]	3.19e0	free	-

Table 6.2: Outcomes of the comparison for the prism, showing a small error between the equations and the finite-element model, for the standard design defined in table 6.1.

The dimensions and material parameters chosen for the standard design of the tetrahedron and prism element are listed in Table 6.1. The dimensions are chosen such that the standard design is roughly similar to the elements used in the four joint designs in section 6.2. The tetrahedron and prism elements as shown in Fig. 6.4 were modelled in Comsol using shell elements. Edge a_1a_3 is fixed and the end effector (edge c_1c_3) is defined as rigid using the 'rigid connector' option. In the tetrahedron element, this rigid edge is extended to reach point P. The results for the prism and tetrahedron element are

Stiffness term	FEM	Equations	Error
K_u [N/m]	4.06e6	3.62e6	11.0%
K_v [N/m]	2.87e6	2.38e6	16.9%
K_w [N/m]	2.37e7	2.61e7	10.1%
K_{θ_u} [Nm/rad]	1.18e2	free	-
K_{θ_v} [Nm/rad]	5.90e3	5.27e3	10.7%
K_{θ_w} [Nm/rad]	1.98e1	free	-

Table 6.3: Outcomes of the comparison for the tetrahedron, showing a larger error between the equations and the finite-element model, for the standard design defined in table 6.1.

listed in Tables 6.2 and 6.3 respectively, together with their relative error.

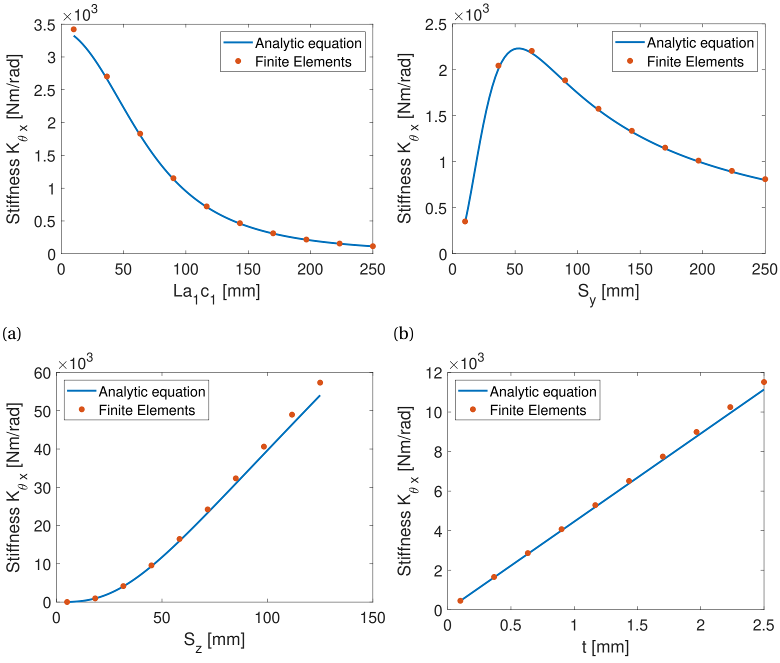

(a) (b)

(c) (d)

Figure 6.12: Outcomes of the comparison of the analytic equation for stiffness K_{θ_x} with finite-element simulations for the prism in Fig. 6.4b, showing a good correspondence with a NMAE of 1.9%. The design parameters are varied one-by-one from the standard design defined in Table 6.1.

As a second test, the parameters from the standard design are varied one-by-one and the stiffness terms K_{θ_x} (for the prism) and K_v (for the tetrahedron) are compared to finite-element simulations. These two particular stiffness terms are chosen because they are dependent on all three blade flexures. The results for the prism are shown in Fig. 6.12. The design parameters range from a fifth of their standard value to five times their stan-

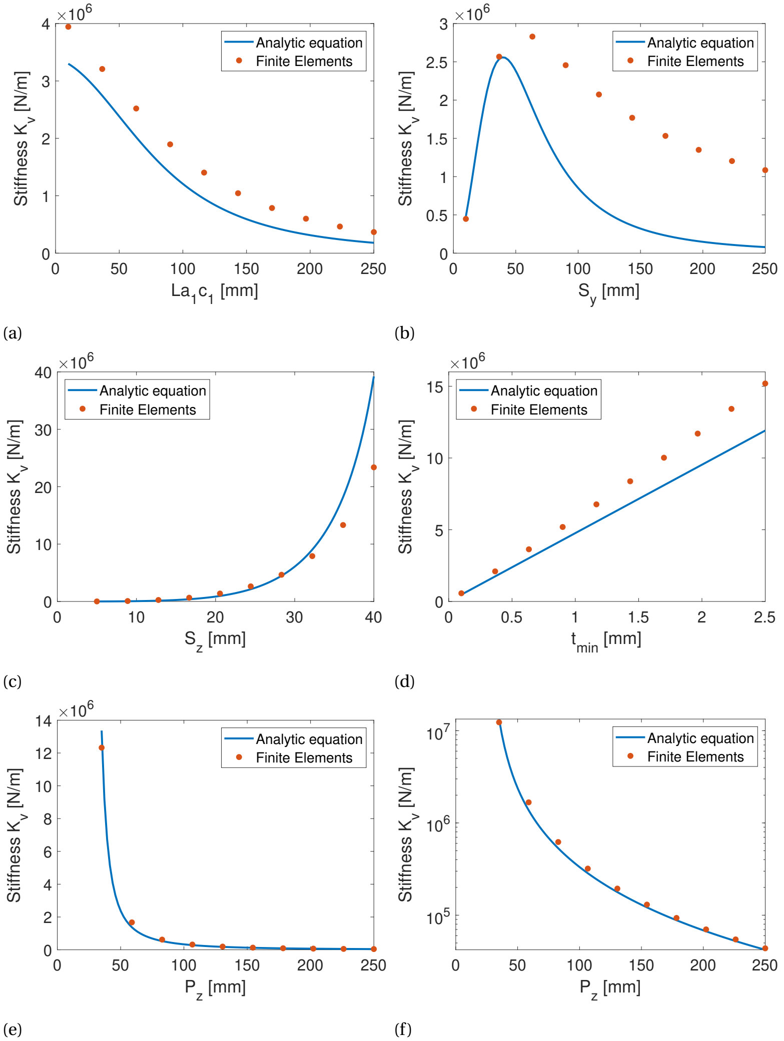

(a) (b)

(c) (d)

(e) (f)

Figure 6.13: Outcomes of the comparison of the analytic equation for stiffness K_v with finite-element simulations for the tetrahedron in Fig. 6.4a, showing that only the qualitative behavior is captured with a NMAE of 34.9%. Graph f) shows the same data as graph e) but uses a log scale for the y-axis.

dard value. This is expected to be large enough to cover most practical uses. The results for the tetrahedron element are listed in Fig. 6.13. The parameters are again changed to one-fifth and five times the standard value, with two exceptions. The height S_z has a maximum value of 40 mm, because larger values will (almost) close off the bottom of the element. For the same reason, the minimum value of P_z is chosen as 35 mm. The plots in Figs. 6.13e and 6.13f contain the same information but the latter has a log-scale for the y-axis.

To quantify the errors, a normalized mean absolute error (NMAE) is computed. The

NMAE is a regular MAE normalized by the maximum value in the displacement range as:

$$\text{NMAE} = \frac{\frac{1}{N}\sum_{n=1}^{N}|\hat{y}_n - y_n|}{max|y|}, \tag{6.28}$$

in which N is the amount of measured data points (10 per design parameter), $\hat{y}$ is the value from te equations and y is the data from the finite-element model.

The stiffness equations for the prism show a good correspondence with the finite-element simulations, with a maximum NMAE of 1.9%. The equations for the tetrahedron do capture the qualitative behavior but show significantly larger errors with a maximum NMAE of 34.9% in the case where the width S_y is varied. This is expected to be caused by the approximation of the trapezoidal blade flexures. Also, to compute the equivalent stiffness of blade flexures ab and bc in equation 6.3, the lateral stiffness of the blade flexures is used. This is correct in the case of the prism element because the force F_{bp} in Fig. 6.9 is perpendicular to the two blade flexures. For the tetrahedron element this is not the case. A continuum mechanics approach is expected to give better results in this situation.

The stiffness in the directions denoted as ‘free’ in Tables 6.3 and 6.2 are significantly lower than the stiffness in the other directions. This validates that these are the degrees of freedom of the elements, as was derived in section 6.3.2.

6.4. DISCUSSION

The prism element has an optimal width S_y for which the rotational stiffness K_{θ_x} is highest. For the standard design this is the optimum in the graph in Fig. 6.12b. A larger width S_y results in a larger moment arm of the equivalent wire flexure (representing blade flexures ab and bc) which increases stiffness K_{θ_x}, but it also results in longer blade flexures ab and bc which decreases stiffness K_{θ_x}. The optimal width $S_{y_{opt.}}$ can be calculated by first setting the derivative of K_{θ_x} with respect to S_y to zero as:

$$\frac{\partial K_{\theta_x}(S_y)}{\partial S_y} = 0. \tag{6.29}$$

Solving for S_y gives the optimal width $S_{y_{opt.}}$ as:

$$S_{y_{opt.}} = \frac{1}{2}\left[\sqrt{4\,L_{a_2c_2}^4 + \frac{48\,L_{a_2c_2}^2\,S_z^2\,(\nu+1)}{5}} + L_{a_2c_2}^2 + \frac{12\,S_z^2\,(\nu+1)}{5}\right]^{\frac{1}{2}}, \tag{6.30}$$

where ν is Poisson’s ratio $\nu = 2G/E - 1$. The graph in Fig. 6.12b shows that the width S_y of 50 mm of the standard design is close to its optimal value. Table 6.2 shows that for the standard design, stiffness terms K_{θ_x} and K_{θ_y} are of comparable magnitude.

The insights from the analysis of the isolated tetrahedron and prism elements can be used when designing complete joints consisting of multiple elements in series. For example, it is useful to know that the rotational stiffness terms K_{θ_x} and K_{θ_y} are of comparable magnitude for the standard prism design. If one of these stiffness terms would be much lower, the joint should be designed such that a large moment arm between the end effector and such a low-stiffness rotation axis are avoided. Note that equations for coupling terms are not derived, which are needed for a full analysis of the stiffness at the end effector of a serial chain of elements. These could be derived using the procedure in this paper, but will result in lengthy equations. In this case, a numerical optimization is expected to be more useful.

Because of the specific shape of the tetrahedron element it can be connected in series without intermediate bodies, which is new with respect to the designs currently found in literature. Edges a_1a_3 and c_1c_3 of the tetrahedron in Fig. 6.4a form the interfaces at which other elements can be connected. If two tetrahedron elements are connected such that their connecting edges and corresponding vertices coincide (as in the two presented spherical joint designs), no intermediate bodies are needed. Connecting elements in series helps to increase the range of motion, because the strains due to displacement in the motion direction of the joint are distributed over the elements [18, 19]. The state-of-the-art designs two, three and four shown in Fig. 6.1 could also be connected in series to increase their range of motion, if the joints are redesigned such that their rotation points coincide. However, this results in intermediate bodies which increase build volume, weight and material usage, and often deteriorate dynamic performance due to uncontrolled vibrations [2, 14].

In [19], a distinction is made between flexure systems and flexure elements, of which the first type possesses rigid bodies and the latter does not. In this perspective, the designs presented in this paper are considered as a flexure element rather than a flexure system.

The Tetra II design shown in Fig. 6.5 could be fabricated using Wire Electrical Discharge Machining (WEDM), instead of using additive manufacturing of titanium as in the demonstration movie that can be found online using the DOI of this article. WEDM is a proven technique for the fabrication of flexure mechanisms and angles of 45 degrees are feasible.

6.5. CONCLUSION

In this paper we have presented designs of two spherical flexure joints named Tetra I and Tetra II, together with their derived planar versions. The designs are formed by tetrahedron-shaped elements, each composed of three blade flexures with a trapezoidal shape, that are connected in series without intermediate bodies. This is new with respect to the designs currently found in literature and helps to increase the range of motion. The Tetra I design consists of two arms, each built up from four tetrahedron elements in series. The Tetra II design consists of three tetrahedron elements which are also connected in series, but form a nested configuration.

We showed that the tetrahedron element is a generalized version of the triangular prism from earlier work. The tetrahedron changes into a triangular prism in the special case where the rotation point of the spherical joints is chosen at infinity.

We developed equivalent representations of the tetrahedron and prism elements consisting of a blade flexure and a wire flexure connected by a rigid part. Using these representations we have proven that three of the four constraint stiffness terms solely depend on the properties of the main blade flexure.

From the equivalent representations we derived equations for the constraint stiffness terms for both the prism and the tetrahedron, resulting also in an equation for the optimal width for which the prism has the highest rotational stiffness along the torsion axis of the main blade flexure.

By comparing the analytic equations to finite-element simulations, a good correspondence for the prism was found with a normalized mean squared error (NMAE) of 1.9%. For the tetrahedron element, the equations showed to only capture the qualitative behaviour with a NMAE of 34.9%, which is expected to be caused by the approximation of the trapezoidal blade flexures.

6.6. ACKNOWLEDGMENT

This work is part of the research programme Möbius with project number 14665, which is (partly) financed by the Netherlands Organisation for Scientific Research (NWO).

REFERENCES

[1] J. Rommers, V. van der Wijk, and J. L. Herder, *A new type of spherical flexure joint based on tetrahedron elements,* Precision Engineering **71**, 130 (2021).

[2] M. Naves, R. Aarts, and D. Brouwer, *Large stroke high off-axis stiffness three degree of freedom spherical flexure joint,* Precision Engineering **56**, 422 (2019).

[3] N. Lobontiu and J. S. Paine, *Design of circular cross-section corner-filleted flexure hinges for three-dimensional compliant mechanisms,* J. Mech. Des. **124**, 479 (2002).

[4] H. Soemers, *Design Principles for precision mechanisms* (T-Pointprint, 2011).

[5] L. L. Howell, S. P. Magleby, and B. M. Olsen, *Handbook of compliant mechanisms* (John Wiley & Sons, 2013).

[6] B. P. Trease, Y.-M. Moon, and S. Kota, *Design of large-displacement compliant joints,* (2005).

[7] C. Brecher, N. Pyschny, and J. Behrens, *Flexure-based 6-axis alignment module for automated laser assembly,* in *International precision assembly seminar* (Springer, 2010) pp. 159–166.

[8] P. Schellekens, N. Rosielle, H. Vermeulen, M. Vermeulen, S. Wetzels, and W. Pril, *Design for precision: current status and trends,* Cirp Annals **47**, 557 (1998).

[9] J. Rommers, M. Naves, D. Brouwer, and J. Herder, *A large range spatial linear guide with torsion reinforcement structures,* in *International Design Engineering Technical Conferences and Computers and Information in Engineering Conference,* Vol. 51807 (American Society of Mechanical Engineers, 2018).

[10] D. Wiersma, S. Boer, R. Aarts, and D. Brouwer, *Design and performance optimization of large stroke spatial flexures,* Journal of Computational and Nonlinear Dynamics **9** (2014), 10.1115/1.4025669.

[11] M. Naves, D. Brouwer, and R. Aarts, *Building block-based spatial topology synthesis method for large-stroke flexure hinges,* Journal of Mechanisms and Robotics **9** (2017), 10.1115/1.4036223.

[12] L. C. Hale, *Principles and techniques for designing precision machines*, Tech. Rep. (Lawrence Livermore National Lab.(LLNL), Livermore, CA (United States), 1999).

[13] D. L. Blanding, *Exact constraint: machine design using kinematic principles* (American Society of Mechanical Engineers, 1999).

[14] J. B. Hopkins, *A visualization approach for analyzing and synthesizing serial flexure elements,* Journal of Mechanisms and Robotics **7** (2015).

[15] J. B. Hopkins and M. L. Culpepper, *Synthesis of multi-degree of freedom, parallel flexure system concepts via freedom and constraint topology (fact)–part i: Principles,* Precision Engineering **34**, 259 (2010).

[16] J. Gere, *Mechanics of Materials. 6th ed.* (Brooks/Cole-Thomas Learning, 2004).

[17] R. Hibbeler, *Mechanics of Materials* (Prentice Hall, 2005).

[18] E. G. Merriam, J. M. Lund, and L. L. Howell, *Compound joints: Behavior and benefits of flexure arrays,* Precision Engineering **45**, 79 (2016).

[19] J. Hopkins, *Designing hybrid flexure systems and elements using freedom and constraint topologies,* Mechanical Sciences **4**, 319 (2013).

7

DISCUSSION

This chapter contains a general discussion on the two parts of this thesis, in addition to the specific discussions per chapter. First, it reflects on the STAGE method in the context of current design methods, and discusses its limitations and further opportunities. Then, a different perspective on the results from the last two chapters is presented.

7.1. DISCUSSION ON PART 1 (CHAPTERS 2-4)

The challenge when designing flexure mechanisms with a large motion range is that they are essentially structures subjected to large deflections, and analytic expressions for their motion and stiffness behavior have only been derived in specific cases due to nonlinearities. Current design methods deal with this by either assuming infinitesimal changes in geometry as in constraint-based design [1–3], or by severely simplifying the flexure mechanism to a rigid-body counterpart as in pseudo-rigid body modeling [4]. Both approaches make it difficult to generate flexure mechanisms with a large range of motion: constraint based design assumes that the functional geometry is equal to the fabrication geometry, and pseudo-rigid body modeling simplifies the mechanics to such an extent that it is not possible to accurately control the geometry (and curvature) during motion. Although the STAGE method developed in this thesis also does not provide control over the full range of motion, it does allow to control the geometry and stresses at large displacements even if the behavior is nonlinear, without simplifying the mechanics.

The examples in this thesis show that initially curved and stressed flexures can lead to improvements regarding peak stress, actuation force and support stiffness at large displacements. The examples have been limited to single degree of freedom mechanisms with parallel flexure arrangements, but the method is not restricted to these types and can be directly applied to other types. An exception is when a mechanism does not have any closed chains and stresses are to be designed. For example, the stresses in a fully serial configuration with one attachment point and a floating end effector cannot be designed using the method, because at least two attachment points are needed to introduce stresses.

This thesis has been limited to blade flexures with curvature in the plane of motion of the mechanism. It is also possible to add other curvatures to a blade flexure, for example by twisting it around its length axis. This would allow the design of more complex stress distributions. Furthermore, any curved geometry could be investigated, instead of starting from pre-existing flexures. The STAGE method could be also be used for more complex geometries, when an inverse finite-element code based on shell or solid elements would be used instead of 2D beam elements as in this thesis. To investigate these more complex geometries, two questions have to be answered. The first is which curved geometries provide a distinct high and low instantaneous stiffness in different directions, respectively, in order to function as a kinematic element in a flexure mechanism. The second question is how these geometries can be used for large displacements. For this second question the STAGE method could be used. The efficient computation of the stress-free geometry will be even more advantageous when used in the more computationally expensive shell or solid models. A good starting point for the first question could be [5], in which the instantaneous stiffness of several curved thin-walled geometries is investigated in different directions. From this overview, the geometries with distinct high and low instantaneous stiffness can be selected.

7.2. DISCUSSION ON PART 2 (CHAPTERS 5 AND 6)

In the original work which introduces the torsion reinforcement strategy [6], the reinforcements are applied to a single straight blade flexure in order to increase its support stiffness at large displacements. In chapter 5, torsion reinforcements are applied to a folded leaf spring instead of a blade flexure, which results in the new planar flexure element shown in Fig. 5.3. The key contribution here is that two of the prism elements are connected under an angle without an intermediate body, creating a new flexure element (instead of a flexure system, which would be the case with intermediate bodies). The generalized tetrahedron element in chapter 6 allows a connection under a second angle, also without an intermediate body, as shown in the spherical joint design in Fig. 6.2. In this perspective, the contribution of chapters 5 and 6 is that they present a new spatial flexure, consisting of tetrahedron or prism elements connected under different angles. The rotation points of the elements do not necessarily have to be all at infinity or all intersect at a single point, as in the planar and spherical joints presented in this thesis. For example, a prism element could be connected to a tetrahedron element, resulting in different kinematics. Different parallel configurations of these elements might also lead to useful new designs.

REFERENCES

[1] J. B. Hopkins and M. L. Culpepper, *Synthesis of multi-degree of freedom, parallel flexure system concepts via freedom and constraint topology (fact)–part i: Principles,* Precision Engineering **34**, 259 (2010).

[2] J. B. Hopkins and M. L. Culpepper, *Synthesis of multi-degree of freedom, parallel flexure system concepts via freedom and constraint topology (fact). part ii: Practice,* Precision Engineering **34**, 271 (2010).

[3] L. C. Hale, *Principles and techniques for designing precision machines*, Tech. Rep. (Lawrence Livermore National Lab.(LLNL), Livermore, CA (United States), 1999).

[4] L. L. Howell, *Compliant mechanisms,* in *21st Century Kinematics* (Springer, 2013) pp. 189–216.

[5] J. Nijssen, G. Radaelli, C. J. Kim, and J. L. Herder, *Overview and kinetostatic characterization of compliant shell mechanism building blocks,* Journal of Mechanisms and Robotics **12** (2020).

[6] D. Wiersma, S. Boer, R. Aarts, and D. Brouwer, *Design and performance optimization of large stroke spatial flexures,* Journal of Computational and Nonlinear Dynamics **9** (2014), 10.1115/1.4025669.

8

CONCLUSION

This thesis has presented design strategies to increase the motion range of flexure mechanisms. The first part of the thesis focused on initially curved and stressed flexures, and the second part on expanding the recent 'torsion reinforcement' strategy. The original contributions are summarized in this chapter.

8.1. CONCLUSIONS OF PART 1 (CHAPTERS 2-4)

In the first part of this thesis the stress and geometry (STAGE) method was proposed, which can be used to design the stress and geometry of flexure mechanisms simultaneously for a specified state. This allows designers to control at which point in the displacement range the flexures are curved and stressed, which in turn enables the design of initially curved and stressed flexures. The main contribution of the method is that it explicitly distinguishes between the functional geometry and the fabrication geometry, which are commonly regarded as equal. The method is valid for large displacements without simplifying the mechanics, by using the relatively unknown inverse finite-element method. The STAGE method gives insight in the achievable stress fields by providing a graphical approach. It shows that the stress field of a flexure mechanism can be designed independently from its geometry and vice versa if it is statically determinate, if bending stresses dominate, and if it consists of slender flexures with constant cross sections. If this is not the case, a parameter sweep can be used as demonstrated in chapter 3.

The potential of the method was demonstrated by creating initial stress fields in commonly used flexure mechanisms with the goal of reducing peak stress or actuation force at large displacements. In the well-known crossed-flexure pivot design, a peak stress reduction of 23% was achieved. The actuation force of a folded leaf spring linear guide mechanism has been decreased by 96%, at the cost of an increase of 45% in peak stress. A different initial stress field in the latter mechanism resulted in a simultaneous reduction of actuation force (35%) and peak stress (28%), which is a surprising result because commonly a trade-off has to be made between these two properties. After assembly, the redesigns attain the functional geometry, which was originally intended by the designer. This means that existing flexure mechanisms could be replaced by their redesigned versions without changes in their geometry and without changing their attachment points in the machine.

Experiments validated the theoretically predicted peak stress and actuation force reduction. Additional experiments showed that the functional geometry was well attained after assembly, with geometric deviations in the order of half the thickness of the flexures. The flexures were fabricated using wire-electrical discharge machining, which is a proven fabrication method in industry.

Chapter 4 showed that curved flexures can be used to create a folded leaf spring with a high support stiffness at large displacements, and that, theoretically, a combination of different elements could be used to create a high support stiffness in the whole motion range. It is likely that the same approach will benefit other flexure designs.

8.2. CONCLUSIONS OF PART 2 (CHAPTERS 5 AND 6)

In the second part of this thesis, the recent 'torsion reinforcement' strategy has been further developed and generalized. This strategy aims to increase support stiffness at large displacements, by resisting torsional deformations in flexures which arise due to their curvature during motion.

In chapter 5, torsion reinforcement structures were added to a folded leaf spring, which increases its constraints from one to three. This enables the design of a linear guide with only two flexure elements instead of the five (or six) folded leaf springs as in pre-existing designs. Both the pre-existing and the new design were optimized on support stiffness and then compared. The support stiffness of the new design showed to be twice as high as the pre-existing design, while occupying a 33% smaller and less obstructive build volume. The models used to assess the support stiffness were validated by experiments.

In chapter 6, a generalization of the blade flexure with a single torsion reinforcement structure was presented in the form of a tetrahedron-shaped element. Using this element, two new spherical joint designs were conceived. These joints allow a large motion range without intermediate bodies, which is new with respect to the state of the art. Analytic equations were presented for the support stiffness of the element in its undeflected state and compared to finite-element simulations.

8.3. GENERAL CONCLUSIONS

This thesis has shown that flexure mechanisms can be improved significantly, even without changing their designed geometry. In designs with open chains, torsion reinforcements can be applied, both in planar and spatially curved mechanisms. This results in improved support stiffness at large motion ranges and adds additional constraints, which means that less flexure elements are required to suppress a set of degrees-of-freedom. In designs with closed chains, torsion reinforcements can also be applied, and additionally, an initial stress field can be introduced. A correctly designed initial stress field can decrease the stresses due to motion of the mechanism, for example in the commonly used crossed-flexure pivot design. The initial stress field is introduced without changing the geometry of the mechanism. In this respect, all existing crossed-flexure pivots can be improved. A second use of the initial stress field is the reduction of actuation forces. In the common folded leaf spring, both the actuation force and the stresses due to motion can be reduced simultaneously. By combining the techniques proposed in this thesis, an initial stress field can be used to eliminate the increase of motion stiffness and stress due to the torsion reinforcements.

ACKNOWLEDGEMENTS

Of course, this thesis was not an individual effort but rather the work of many people, before and during my PhD period. Just, I want to thank you for teaching me a way of thinking which I learned to appreciate even more now that I am working in Industry. I still clearly remember the excitement in some of our conversations when we realized that we stumbled upon a new idea, and your talent to motivate if things were not working out. Volkert, thank you for showing different perspectives on the academic world and on writing, these were very valuable. I learned a lot from my co-authors Mark Naves, Dannis Brouwer, Alden Yellowhorse, Alejandro Aragon, and the students that I mentored. I appreciated the warm and non-competitive atmosphere in the group of Just where everybody always freed up time to help each other. The companies that co-funded the project helped to keep the applications in mind, and I especially appreciated the conversations with Ard Geelkerken (Hittech), Jan Nijenhuis (TNO), Pieter Kappelhof (Hittech), Jules Oostdijk (ASML) and Stefan Vossen (Hittech). I know that the lab support at the 3ME faculty is of outstanding quality compared to the rest of the world, and would like to thank the group of Rob Luttjeboer, with in particular Patrick Holst, for supporting the experiments. I am grateful for having a group of friends which provided ample motivation, in particular the conversations with my friend Robbert on our long walks through the dunes, where we discussed the more philosophical aspects that I encountered in the research project.

A special corner is reserved for my family, with in particular my parents, for teaching me to focus on the important things in life, and for helping me to recognize what these things are. Evelien, you know that I am not exaggerating when I say that, especially given the turbulent times in the last year of the project, without you this thesis would not have been what it is now.

A

INVERSE FEM EXAMPLE

In this appendix, we provide an illustrative example to help to understand the solution method used in the inverse FEM code used in this thesis in an intuitive way. First, the example problem is solved analytically. We then use Newton-Raphson to find a solution, similar to the way in which nonlinear FEM problems are often solved. We start with the conventional (forward) case and then show the difference with the inverse case.

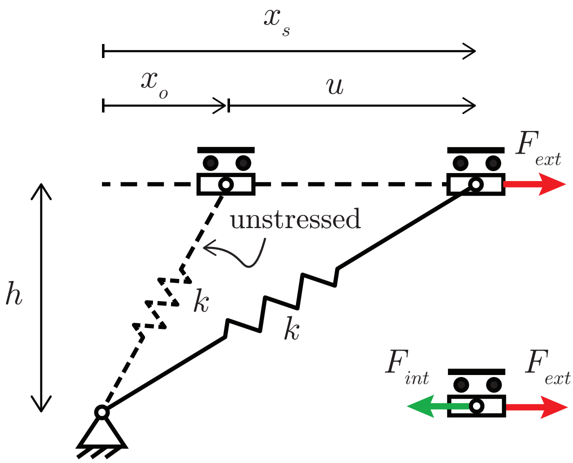

Figure A.1: Example used to explain the inverse FEM solution method.

Figure A.1 shows a spring-slider mechanism. The spring with stiffness k is drawn in its stress-free (dashed) and stressed states. We assume that the height h is fixed and the stress-free and stressed geometries of the spring are fully described by x_o and x_s, respectively. We choose $h = 50$ mm, $k = 2$ N/mm, $F_{ext} = 15$ N and $x_o = 25$ mm. The internal force F_{int} is the horizontal component of the spring force, which is equal to F_{ext} at static equilibrium. We write this equilibrium by equating the residual R (the force imbalance) to zero:

$$R(x_o, x_s) = F_{int}(x_o, x_s) - F_{ext} = 0. \tag{A.1}$$

For this example, the following equation can be derived:

$$R(x_o, x_s) = kx_s \left[1 - \sqrt{\frac{h^2 + x_o^2}{h^2 + x_s^2}}\right] - F_{ext} = 0. \tag{A.2}$$

Note that $x_s = x_o + u$, where u is the displacement from the stress-free configuration. Equation (A.2) is written in terms of x_o and x_s, while conventionally x_o and u would be used. This choice will show to be more convenient for inverse FEM. Equations (A.1) and (A.2) already give some insight into the difference between the forward and inverse problem. In the forward case, x_o is known and x_s has to be found, whereas in the inverse case, x_s is known and x_o has to be found.

We now proceed to solve the example problem using the Newton-Raphson solution method, starting with the conventional forward case. We assume that similar to a FEM problem, the analytical equation (A.2) can not be solved explicitly but its residual can be evaluated sequentially for a certain input x_s. The nonlinear problem can be solved using an iterative gradient-based approach, such as Newton-Raphson. The gradient of

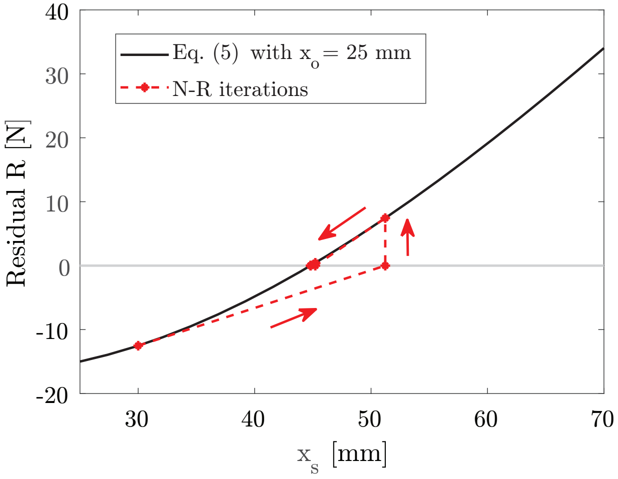

Figure A.2: Newton-Raphson iterations of the conventional (forward) analysis, in which x_o is known and x_s is to be found. Note that in this case, equation (A.2) is a function of x_s.

the residual equation is computed as:

$$K_{fwd} = \frac{\partial R(x_o, x_s)}{\partial x_s} = k\left[1 - \frac{h^2\sqrt{h^2 + x_o}}{(h^2 + x_s^2)^{3/2}}\right], \tag{A.3}$$

where K_{fwd} is the stiffness of the system. Figure A.2 shows how this gradient can be used to iteratively find the solution. We start with the (arbitrary) initial guess of $x_s = 30mm$. The residual is calculated and using K_{fwd} a new guess for x_s is computed. At the intersection of the dashed line with the horizontal axis, this updated value for x_s is obtained and the residual is re-evaluated. This process is repeated until the residual is sufficiently small to consider the problem to be solved. This results in a x_s of around 44.8 mm as the solution to the problem. If we substitute $x_o = 25$ and $x_s = 44.8$ in equation (A.2), this indeed results in a residual close to zero.

In the inverse problem, the stressed geometry x_s is known and the stress-free geometry x_o has to be found. We choose $x_s = 44.8$ mm. Using Newton-Raphson, x_o should be found to be close to 25 mm, in order to satisfy the residual equation (A.2). The residual equation is the same as in the forward case. However, the gradient used to solve the problem is different because the residual equation is now a function of x_o:

$$K_{inv} = \frac{\partial R(x_o, x_s)}{\partial x_o} = \frac{-kx_s x_o}{\sqrt{h^2 + x_s^2}\sqrt{h^2 + x_o}}. \tag{A.4}$$

Figure A.3 shows how this gradient can be used to iteratively arrive at the correct solution of x_o around 25 mm, starting from an arbitrary initial guess of $x_o = 5$ mm.

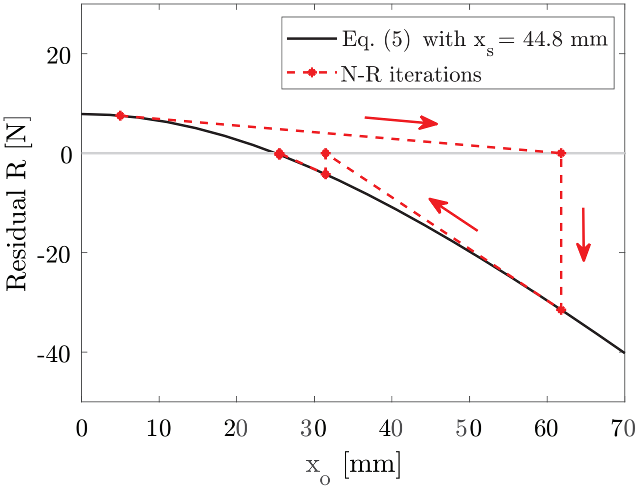

Figure A.3: Newton-Raphson iterations of the inverse analysis, in which x_s is known and x_o is to be found. Note that in this case, equation (A.2) is a function of x_o.

The example shows how Newton-Raphson can be used to solve both forward and inverse nonlinear problems. Although in FEM a multitude of degrees of freedom are present, the solution procedure is very similar to the example presented here.

CURRICULUM VITÆ

Jelle ROMMERS

25-11-1987	Born in Rijswijk, The Netherlands.

EDUCATION

2007–2008	Propaedeutic degree Industrial Design Delft University of Technology, Delft
2008–2012	Bachelor Mechanical Engineering Delft University of Technology, Delft
2012–2015	Master Mechanical Engineering Delft University of Technology, Delft *Thesis:* Modeling and design of origami mechanisms with compliant facets *Promotor:* Prof. dr. ir. Just L. Herder

PROFESSIONAL EXPERIENCE

2013–2015	Research engineer (parttime) *Exasun*
2015–2017	Mechanical engineer R&D *Exasun*

AWARDS

2016	ASME compliant mechanisms award *ASME IDETC conference in Charlotte, North Carolina*

LIST OF PUBLICATIONS

JOURNAL PUBLICATIONS

1. **J. Rommers**, V. van der Wijk, A.M. Aragón, J.L. Herder (2022, to be submitted) *The STAGE method for simultaneous design of the stress and geometry of flexure mechanisms*, Precision Engineering
2. **J. Rommers**, M. Naves, D.M. Brouwer, J.L. Herder (2021) *A flexure-based linear guide with torsion reinforcement structures*, Journal of Mechanisms and Robotics, 10.1115/1.4052971
3. **J. Rommers**, V. van der Wijk, J.L. Herder (2021) *A new type of spherical flexure joint based on tetrahedron elements*, Precision Engineering, 10.1016/j.precisioneng.2021.03.002
4. **J. Rommers**, G. Radaelli, J.L. Herder (2017) *A design tool for a single vertex compliant-facet origami mechanism including torsional hinge lines*, Journal of Mechanisms and Robotics, 10.1115/1.4038008
5. **J. Rommers**, G. Radaelli, J.L. Herder (2017) *Pseudo-rigid-body modeling of a single vertex compliant-facet origami mechanism*, Journal of Mechanisms and Robotics, 10.1115/1.4035881

PEER-REVIEWED CONFERENCE PAPERS

1. A. Yellowhorse, **J. Rommers**, A. Amoozandeh, J.L. Herder (2021) *Methods for Shape Fitting in Morphing Compliant Mechanisms*, ASME IDETC/CIE 2021, Virtual, 10.1115/DETC2021-70686
2. P. Vugts, **J. Rommers**, B.T. Sterke, J.L. Herder (2021) *Conceptual Design of a Compliant Hip Orthosis for Trendelenburg Gait*, ASME IDETC/CIE 2021, Virtual, 10.1115/DETC2021-68104
3. B. Daan, **J. Rommers**, J.L. Herder (2021) *Modelling the Axis Drift of Short Wire Flexures and Increasing Their Support Stiffness Using Polymers*, ASME IDETC/CIE 2021, Virtual, 10.1115/DETC2021-68255
4. **J. Rommers**, J.L. Herder (2019) *Design of a Folded Leaf Spring with high support stiffness at large displacements using the Inverse Finite Element Method*, IFToMM World Congress on Mechanism and Machine Science, Krakau, 10.1007/978-3-030-20131-9_209
5. **J. Rommers**, M. Naves, D.M. Brouwer, J.L. Herder (2018) *A large range spatial linear guide with torsion reinforcement structures*, ASME IDETC/CIE, Quebec City, 10.1115/DETC2018-86424
6. **J. Rommers**, G. Radaelli, J.L. Herder (2016) *A Pseudo Rigid Body Model of a Single Vertex Compliant-Facet Origami Mechanism (SV-COFOM)*, ASME IDETC/CIE, Charlotte, North Carolina, 10.1115/DETC2016-59377